Final Scientific/Technical Report

Submitted to: Department of Energy

DE-NE0000726

Structural Health Monitoring of Nuclear Spent Fuel Storage Facilities

January 13, 2014 to January 12, 2018

PI: Lingyu "Lucy" Yu, Associate Professor
Email:yu3@cec.sc.edu; Office: 803.777.0070

April 10, 2018

DUNS number: 04-138-7846
The University Of South Carolina Research Foundation
1600 Hampton Street, Suite 414, Columbia, SC 29208

Signature of submitting official

Final Report

EXECUTIVE SUMMARY

Interim storage of spent nuclear fuel from reactor sites has gained additional importance and urgency for resolving waste-management-related technical issues. To ensure that nuclear power remains clean energy, monitoring has been identified by DOE as a high priority cross-cutting need, necessary to determine and predict the degradation state of the systems, structures, and components (SSCs) important to safety (ITS). Therefore, nondestructive structural condition monitoring becomes a need to be installed on existing or to be integrated into future storage system to quantify the state of health or to guarantee the safe operation of nuclear power plants (NPPs) during their extended life span.

In this project, the lead university and the collaborating national laboratory teamed to develop a nuclear structural health monitoring (n-SHM) system based on in-situ piezoelectric sensing technologies that can monitor structural degradation and aging for nuclear spent fuel DCSS and similar structures. We also aimed to identify and quantify possible influences of nuclear spent fuel environment (temperature and radiation) to the piezoelectric sensor system and come up with adequate solutions and guidelines therefore. We have therefore developed analytical model for piezoelectric based n-SHM methods, with considerations of temperature and irradiation influence on the model of sensing and algorithms in acoustic emission (AE), guided ultrasonic waves (GUW), and electromechanical impedance spectroscopy (EMIS). On the other side, experimentally the temperature and irradiation influence on the piezoelectric sensors and sensing capabilities were investigated. Both short-term and long-term irradiation investigation with our collaborating national laboratory were performed. Moreover, we developed multi-modal sensing, validated in laboratory setup, and conducted the testing on the We performed multi-modal sensing development, verification and validation tests on very complex structures including a medium-scale vacuum drying chamber and a small-scale mockup canister available for the desired testing. Our work developed the potential candidate for long term structural health monitoring of spent fuel canister through piezoelectric wafer sensors and provided the sensing methodologies based on AE and GUW methodologies. It overall provides an innovative system and methodology for enhancing the safe operation of nuclear power plant. All major accomplishments planned in the original proposal were successfully achieved.

OVERVIEW OF THE PROJECT

OBJECTIVE

The object of the project is to develop a combined modeling and experimental methodology to assess irradiation effects on the SHM system in order to validate and verify (V&V) the proposed sensing methods. Our aim is to identify and quantify the possible influences of the nuclear environment (temperature and radiation) to the proposed sensor and sensing system, and to develop adequate solutions and guidelines accordingly.

SCOPE OF THE TASKS

Our scope here is to develop a SHM system that (1) can be integrated in cask (over pack) or dry storage systems, (2) can detect representative damage such as cracks at various stage, and (3) can withstand the temperature, radiation environment, and long term regime for the expected operational conditions and applications. To attain our goals, we have built up the theoretical foundation of the proposed methodologies, understood the nuclear environmental influences, developed a nuclear qualified sensor system for damage detection and quantification, and experimentally verified the proposed concepts at small and medium scales. All these efforts led to the design guidelines to mitigate the effects of temperature and radiation on the SHM system capability. Our research tasks consisted of four tasks over a three-year period and later extended for one more year to fulfill all tasks.

SUMMARY OF THE ACCOMPLISHED TASKS

During this project, we developed analytical model for piezoelectric based ultrasonic DCSS SHM. We considered the temperature and irradiation influence on the model of sensing and sensing algorithm considering acoustic emission (AE), guided ultrasonic waves (GUW), and electro-mechanical impedance spectrum (EMIS). We explored experimentally and numerically the temperature and irradiation influence on the PWAS sensor and sensing capabilities for steel canisters in nuclear spent fuel storage facilities. We performed multi-modal sensing development, verification and validation tests in laboratory environment. And finally, we studied scale-up issues and performed testing on a vacuum drying chamber. In addition, we have conducted both short-term and long-term irradiation investigation with our collaborating national laboratory. Also, we performed the testing on the mid-size canister mockup. We achieved all major accomplishments planned in the original proposal and are summarized as:

- PWAS sensing modeling with temperature and irradiation effects (Achievement 1)
- Short-term and long-term laboratory study of nuclear environmental influences including temperature and irradiation effects on the PWAS sensor (Achievement 2)
- High temperature piezoelectric evaluation (Achievement 2)
- PWAS sensing algorithms/methodologies (Achievement 3)
- Study of sensing in realistic complex structures with rich features and transition to National laboratory (Achievement 4)

We will summarize major achievements in this report.

1 TECHNICAL ACCOMPLISHMENT 1: DEVELOP ANALYTICAL MODELS FOR PIEZOELECTRIC BASED ULTRASONIC DCSS SHM

1.1 GOAL OF THE REPORTED WORK

The goal is to use a combined ultrasonic sensing including AE, GUW, and EMIS approaches to better understand the challenges of sensing and to ensure a successful detection on the subject DCSS thick steel canister component. In this Task, our goal is to develop the *theoretical framework* for modeling the multimode sensing and create a "virtual sensing" capability to predict the signal changes due to structural flaws/damage with close interaction with our colleagues from the SRNL.

1.2 ACCOMPLISHMENT UNDER THIS GOAL

USC developed the *theoretical framework* for modeling the multimode sensing and created a "virtual sensing" capability to predict the signal changes due to structural flaws/damage. The analytical predictive modeling for GUW interaction with damage (e.g., cracks) in thick steel plates and shells were performed. The signal prediction software was developed for the AE simulation to capture the growth of crack at early stage. For AE simulation, the AE source was simulated by a point excitation that has the same acoustic trend as of an opening crack (i.e., the pop of an opening crack). Diagnostics methodology was developed through case studies with focus on specific facets of structural sensing: (a) sensor-structure interaction and (b) multi-physics transduction modeling. The work will be done analytically, such that the relative interconnection of sensor and structure effects can be easily understood and traced. We will conclude how the presence of crack would change the sensing signal signatures and what the sensitivities are with respect to the damage size and location.

1.3 DISSEMINATION OF THE RESULTS

A wide range of sensors has been developed particularly for generating and receiving acoustic-ultrasonic waves. Piezoelectric wafer active sensors (PWAS) have emerged as one of the major SHM technologies. A variety of damage detection methods can be applied to this type of sensor [6-9]: (a) propagating ultrasonic waves, both acoustic emission (AE) and guided ultrasonic waves (GUW); and (b) standing ultrasonic waves, i.e., electromechanical impedance spectroscopy (EMIS). The proposed sensing will use a combined ultrasonic sensing including AE, GUW, and EMIS approaches. The theoretical framework for modeling the multi-mode sensing and will create a "virtual sensing" capability to predict the signal changes due to structural flaws/damage as well as the environmental conditions (temperature and radiation). In order to use AE and GUW for effective damage detection, it is necessary to study the wave propagation characteristics in the structures and its interactions with structural discontinuities such as damage. However, for the thick structural, there is a major challenge in this method since higher modes of guided wave may appear other than fundamental modes depending on the frequency and thickness of the plate. Hence, we have started developing an analytical solution to provide theoretical studies of waves in thick structures.

1.3.1 Ultrasonic wave modeling

Guided waves modeling using PWAS

The long-range inspection capability is the major attraction of guided waves for structural damage detection. The understanding of wave propagation is the major difficulty. The complexity of guided wave propagation requires some experience related to monitoring strategy and data interpretation. A piezoelectric wafer active sensors (PWAS) can generates Lamb waves into the host structure under electrical excitation. Lamb waves propagate along the structure, interact with the damage, undergo scattering and mode conversion, and are finally picked up by receiver PWAS. The received signal is also comprised of scattered waves from the damage. Thus, the damage can be modeled as a secondary wave source.

The analytical model is a general description of wave generation, propagation, damage interaction, and detection. Parameter exploration is made possible for transmitter PWAS size, structure material and thickness, sensor-damage locations, and arbitrary excitations, etc. In this analytical model, straight-crested Lamb waves propagating in a plate of thickness h=2d was considered. The assumption of straight-crested waves makes the problem z-invariant. Here P+SV waves in a plate were considered. The P waves and SV waves give rise to the Lamb waves. Lamb waves or plate guided waves, are a type of stress waves that remain confined between two parallel traction free plate surfaces. Rayleigh-Lamb equations can be written as follow

$$\frac{\tan \eta_P d}{\tan \eta_S d} = \left[-\frac{(\xi^2 - \eta_S^2)^2}{4\xi^2 \eta_P \eta_S} \right]^{\pm 1} \tag{1}$$

Lamb waves exist in plate structures in two basic types of modes, symmetric and antisymmetric modes. The power of the right hand side of equation (1) changes sign for symmetric and antisymmetric modes; +1 is for symmetric modes and −1 is for antisymmetric modes. Equation (1) can be written as

$$\begin{aligned} &\left(\xi^2 - \eta_S^2\right)^2 \cos \eta_P d \sin \eta_S d + 4\xi^2 \eta_P \eta_S \sin \eta_P d \cos \eta_S d = 0 \qquad \text{(Symmetric)} \\ &\left(\xi^2 - \eta_S^2\right)^2 \sin \eta_P d \cos \eta_S d + 4\xi^2 \eta_P \eta_S \cos \eta_P d \sin \eta_S d = 0 \qquad \text{(AntiSymmetric)} \end{aligned} \tag{2}$$

In order to find the roots of equation (2), the following substitution is made.

$$\overline{\xi} = \xi d \text{ and } \Omega = \frac{\omega d}{c_s} \tag{3}$$

The corresponding roots are shown in Figure 1.

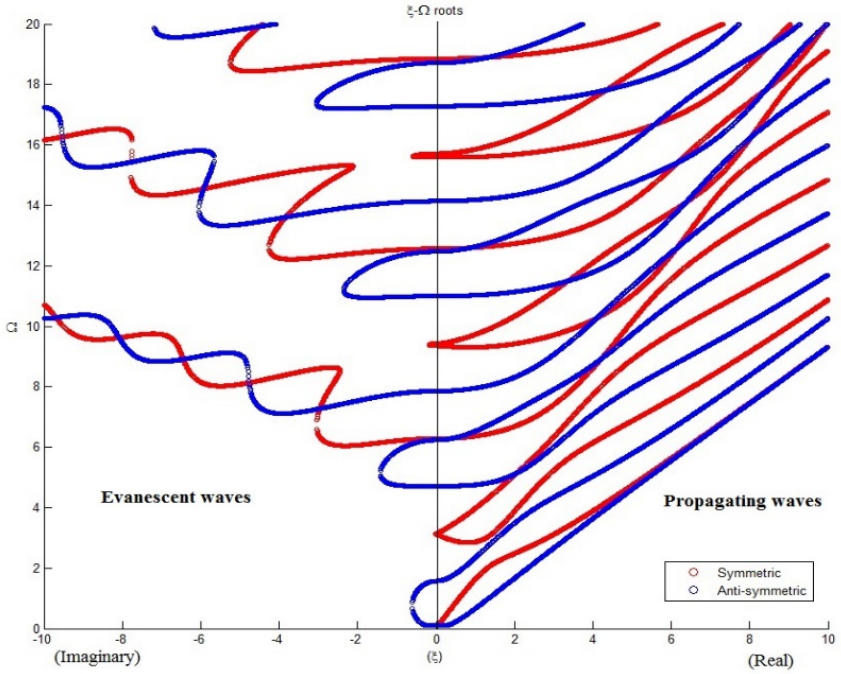

Figure 1 Trajectories of $\overline{\xi} - \Omega$ roots for Poisson ratio 0.33.

Figure 2 shows the phase velocity dispersion curve, group velocity dispersion curve and tuning curve for different thick plate. It can be seen from this figure that for 12.7 mm thick plate at 150 kHz A1 will appear other than A0 and S0, where at 200 kHz both A1 and S1 will appear. So it is important to isolate the wave packets from each other. PWAS tuning is very important in this view. Figure 2 (c, f) show the PWAS tuning curve for different thick plate. It can be seen that at some frequency some mode is dominant than other. For 12.7 mm thick plate at 180 kHz A1 and A0 amplitude is higher than S0. So, it may be useful to focus on particular mode to detect damage for thick plate.

1mm steel plate

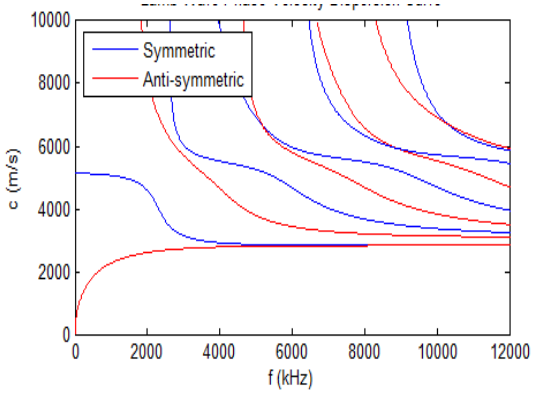

(a)

12.7 mm steel plate

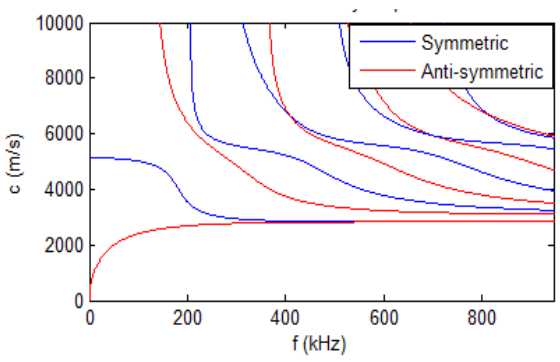

(d)

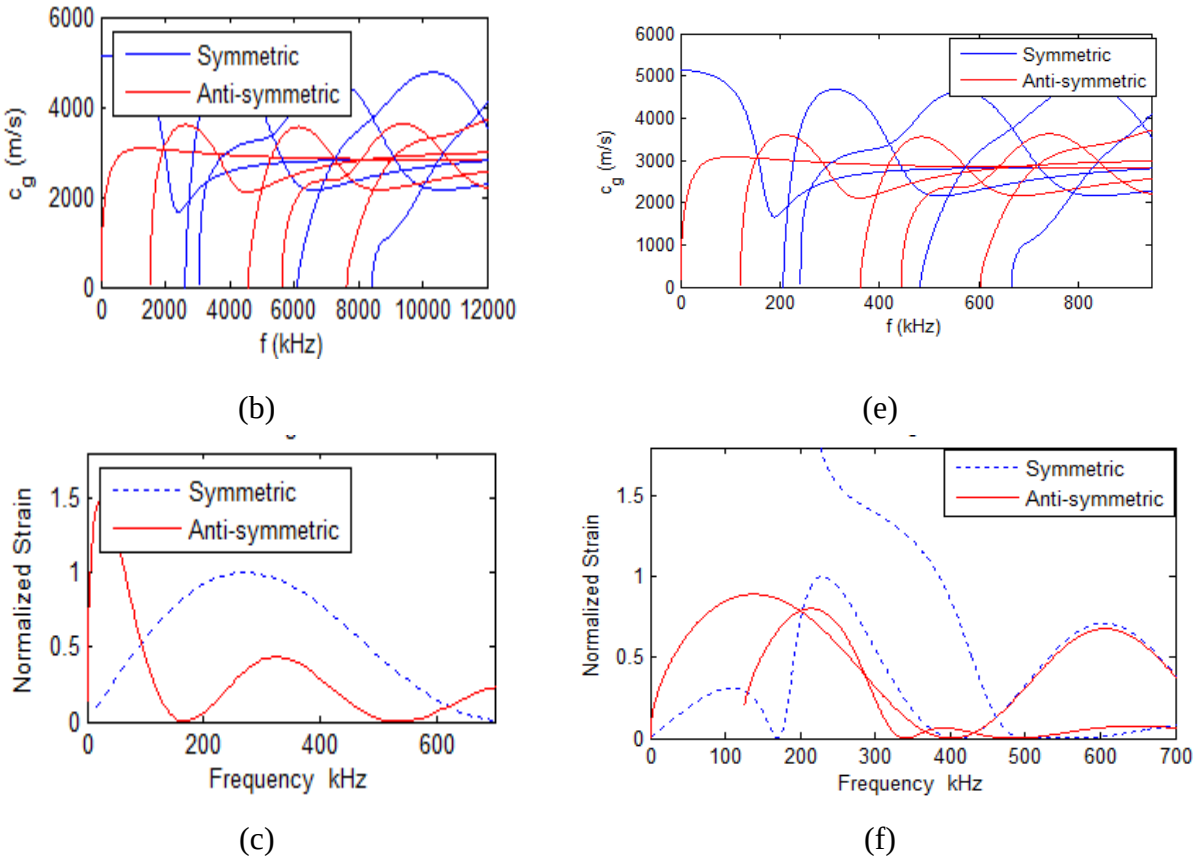

Figure 2 (a, d) Phase velocity, (b, e) group velocity and (c, f) tuning curve of 1 mm and 12.7 mm steel plate.

Experimental validation

For experimental validation 1mm and 12.7 mm thick plates were chosen. In experiment, the major challenge is to analyze signals containing multiple propagation modes. In order to resolve the problem time-frequency analysis was done. A major advantage of time-frequency methods is the ability to analyze signals containing multiple propagation modes of guided waves, which overlap and superimpose in the time domain signal. By combining time-frequency analysis, the dispersion of multiple Lamb modes over a wide frequency range can be determined. PWAS were used to generate and detect guided wave in steel plate. To observe the wave packets, 3 count tone burst signal at different frequency was generated as shown in Figure 3.

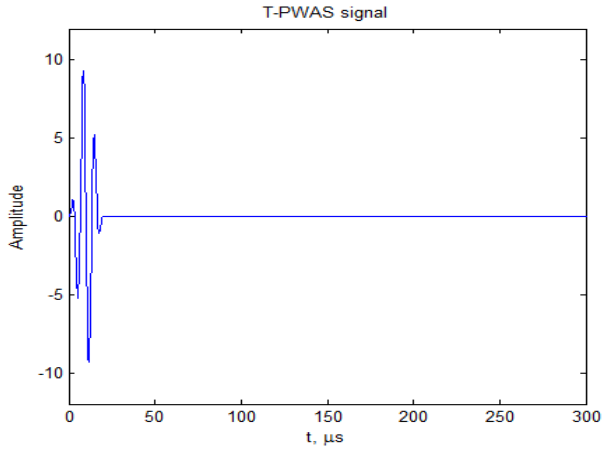

Figure 3 Excitation signal of 4.5 count tone burst

Receiver PWAS was at 100 mm distance for 1mm thick plate and 150 mm for 12.7 mm thick plate (Figure 4). A signal generator was used to generate the signal and a oscilloscope was used to collect and visualize the data (Figure 5).

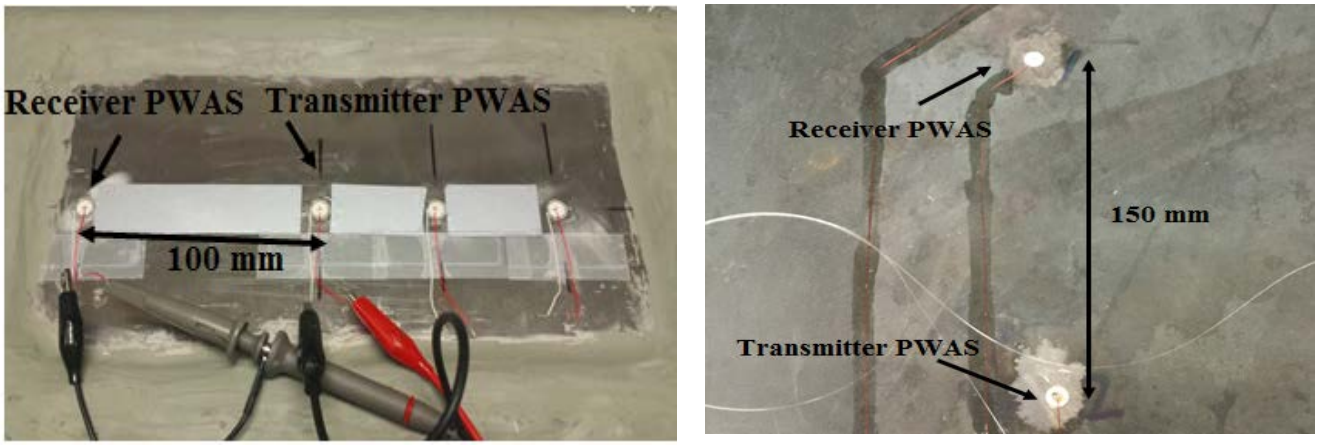

(a) (b)

Figure 4 PWAS location of (a) 1 mm plate and (b) 12.7 mm plate

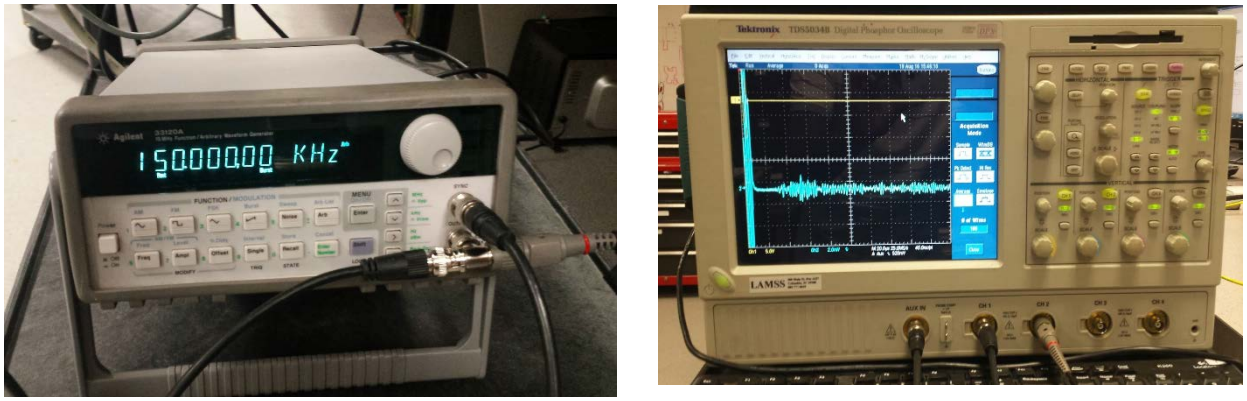

(a) (b)

Figure 5 (a) signal generator and (b) oscilloscope

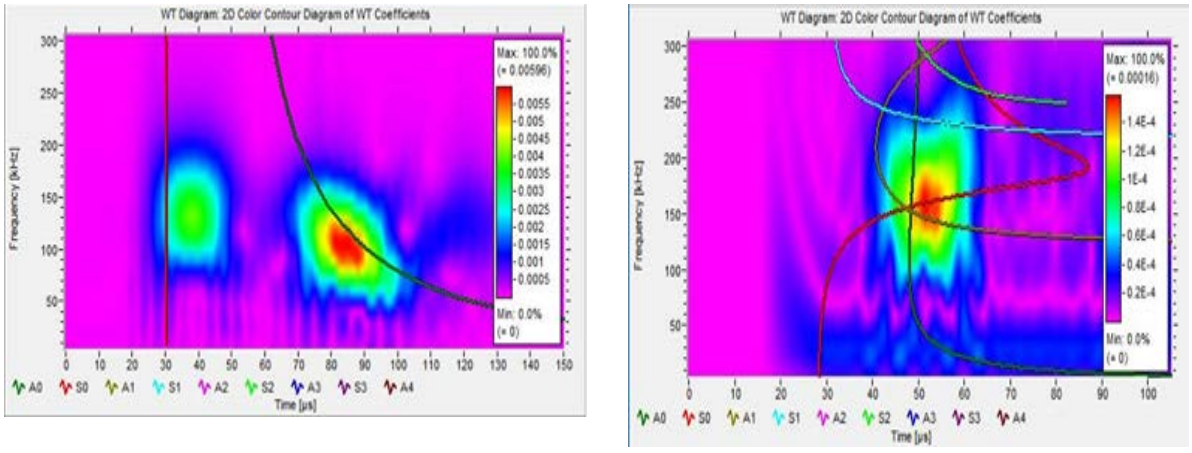

(a) (b)

Figure 6 Time-frequency analysis of (a) 1 mm and (b) 12.7 mm steel plate

In experiment, the major challenge is to analyze signals containing multiple propagation modes. In order to resolve the problem time-frequency analysis was done. For this purpose, AGU-Vallen Wavelet was used. AGU-Vallen Wavelet is a tool which allows you to calculate and display the wavelet and distribution of individual waveforms. A time-frequency transform distributes the energy of a wave in time and frequency. Hence it is possible to identify at what time which frequency content occurs. This kind of analysis is not possible by use of standard Fourier transform. The great advantage of this tool is that time-frequency transform can be superimposed with the inverse of dispersion curve (slowness curve) and distribution of individual wave forms can be obtained. Figure 6 shows the time frequency analysis of a 1mm and 12.7 mm thick plate at 150 kHz. After distinguishing different modes, the PWAS tuning curve were generated (Figure 7 and Figure 8). Experimental results validate the simulation results.

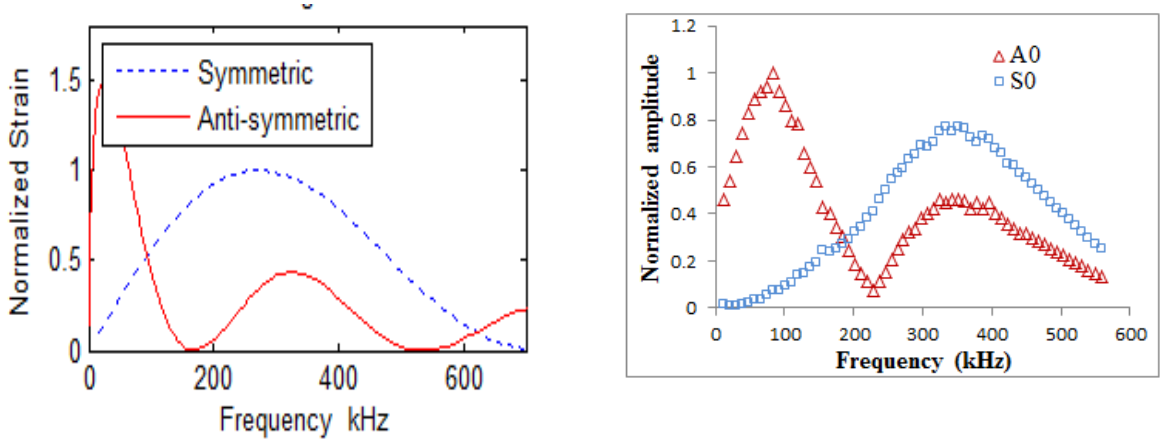

(a) (b)

Figure 7 (a) Numerical and (b) experimental tuning curve of PWAS for 1mm steel plate

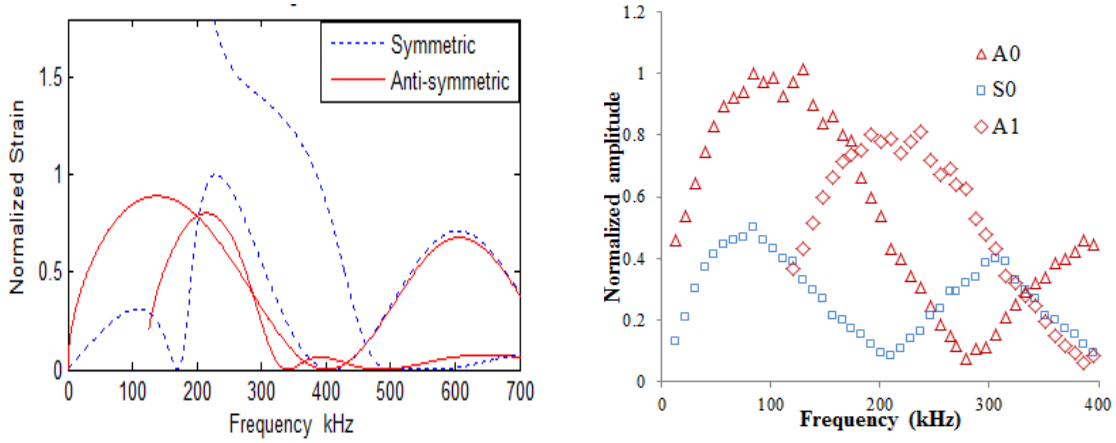

(a) (b)

Figure 8 (a) Numerical and (b) experimental tuning curve of PWAS for 12.7 mm steel plate

1.3.2 Acoustic emission modeling

Acoustic emission (AE) has been used widely in structural health monitoring (SHM) and nondestructive testing (NDT) for the detection of crack propagation and to prevent ultimate failure. Acoustic emission (AE) signals are therefore needed to study extensively in order to characterize the crack in an aging structure. This paper presents a theoretical formulation of AE guided wave due to AE events such as crack extension in a structure. The presence of body force makes the homogeneous Navier-Lame elastodynamic equations into inhomogeneous equations. Helmholtz decomposition principle was used to decompose displacement to unknown scalar and vector potentials, and force vectors to known excitation scalar and vector potentials. There are

two types of potentials acting in a plate for straight crested Lamb waves: pressure potential and shear potential. The assumption of the straight-crested guided wave makes the problem z-invariant (plane strain assumption). Excitation potentials for body forces can be generalized as localized AE event. Excitation potentials can be traced to energy released from the tip of the crack during crack propagation. These potentials satisfy the inhomogeneous wave equations. In this research, inhomogeneous wave equations for unknown potentials were solved due to known generalized excitation potentials in a form, suitable for numerical calculation. The theoretical formulation shows that elastic waves generated in a plate using excitation potentials followed the Rayleigh-Lamb equations. The displacement solution is obtained by following the methodology as shown in Figure 9. The displacement solution is shown in eq. (4).

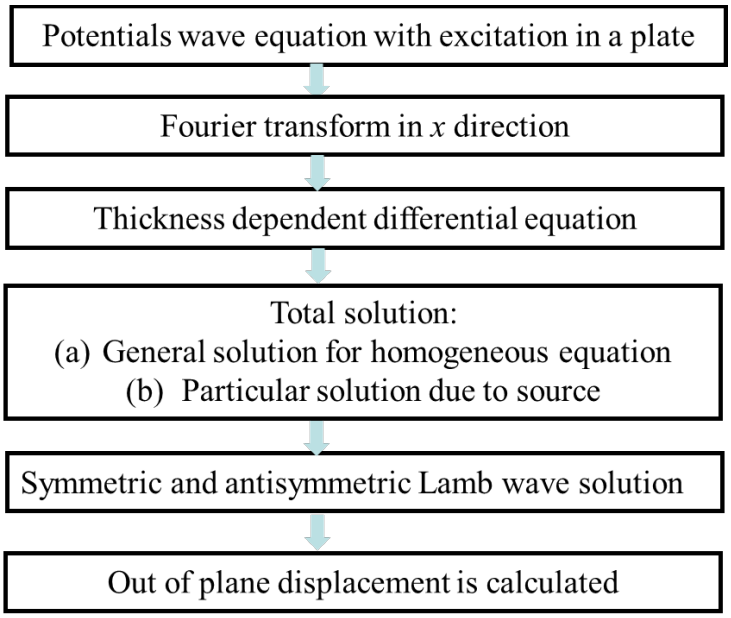

Figure 9 Displacement solution of Lamb wave methodology using excitation potential

$$u_{yL} = i\left(\sum_{j=0}^{j_s} \left[P_S(\xi_j^S) \frac{N_S(\xi_j^S)}{D_s'(\xi_j^S)} \right] e^{i(\xi_j^S x - \omega t)} + \sum_{j=0}^{j_A} \left[P_A(\xi_j^A) \frac{N_A(\xi_j^A)}{D_A'(\xi_j^A)} \right] e^{i(\xi_j^A x - \omega t)} \right) \tag{4}$$

The corresponding source terms, for symmetric and antisymmetric solutions are

$$P_S = (\xi^2 - \eta_s^2) \frac{A}{2\eta_p} \sin \eta_p d_1 + \xi B_z \cos \eta_s d_1 \tag{5}$$

$$P_A = \xi A \cos \eta_p d_1 + (\xi^2 - \eta_s^2) \frac{B_z}{2\eta_s} \sin \eta_s d_1 \tag{6}$$

Results and discussion

AE guided waves will be generated by the AE event. AE guided waves will propagate through the structure according to the structural transfer function. The out-of-plane displacement of the guided waves can be captured by conventional AE transducer installed on the surface of the structure as shown in Figure 10.

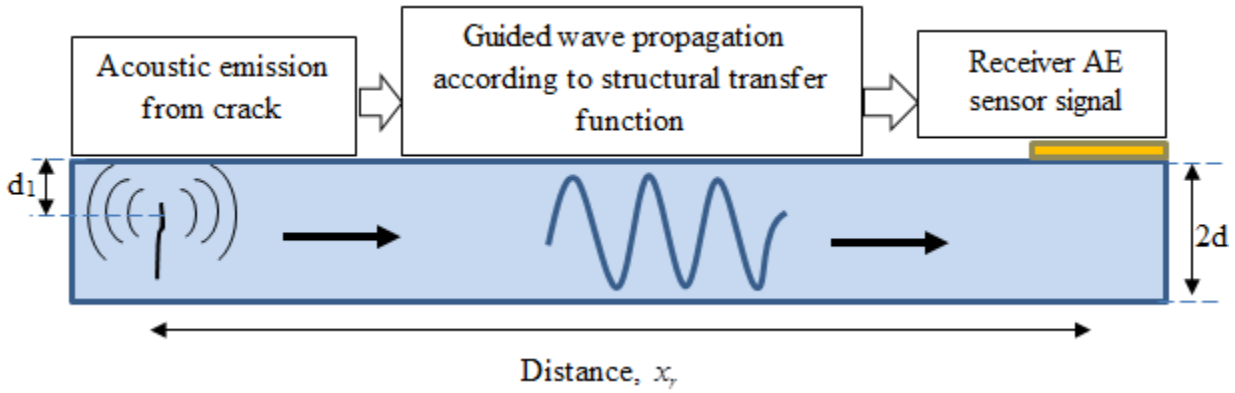

Figure 10 Acoustic emission propagation and detection by a sensor installed on a structure

Figure 11a shows the time rate of excitation (pressure and shear potentials). The corresponding equations are,

$$\frac{\partial A^*}{\partial t} = A_0 t^2 e^{-\frac{t^2}{\tau^2}} \quad ; \quad \frac{\partial B_z^*}{\partial t} = B_{Z0} t^2 e^{-\frac{t^2}{\tau^2}} \tag{7}$$

Here A_0 and B_{z0} are the scaling factors. Time profile of the potentials are to be evaluated by integrating Equation (7), i.e.,

$$A^* = A_0 \left(\sqrt{\pi}\tau erf\left(t/\tau\right) - 2te^{-\frac{t^2}{\tau^2}} \right) \quad ; \quad B_z^* = B_{z0} \left(\sqrt{\pi}\tau erf\left(t/\tau\right) - 2te^{-\frac{t^2}{\tau^2}} \right) \tag{8}$$

Figure 12 shows the out-of-plane displacement (S0 and A0 mode, bulk wave) vs time at 500 mm propagation distance for mid-plane source location. Time profile excitation potentials (Figure 11b) were used to simulate AE waves in the plate. Excitation potential can be calculated from the time rate of potential released during crack propagation. Signals are normalized by their individual peak amplitudes, i.e., amplitude/ peak amplitude.

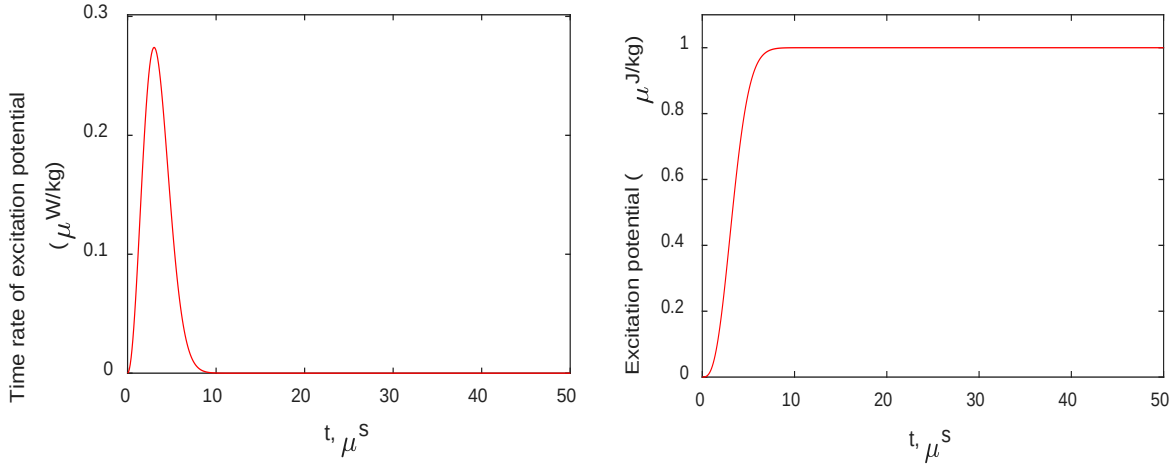

(a) (b)

Figure 11 Excitation profile: (a) Time rate plot and (b) cumulative plot

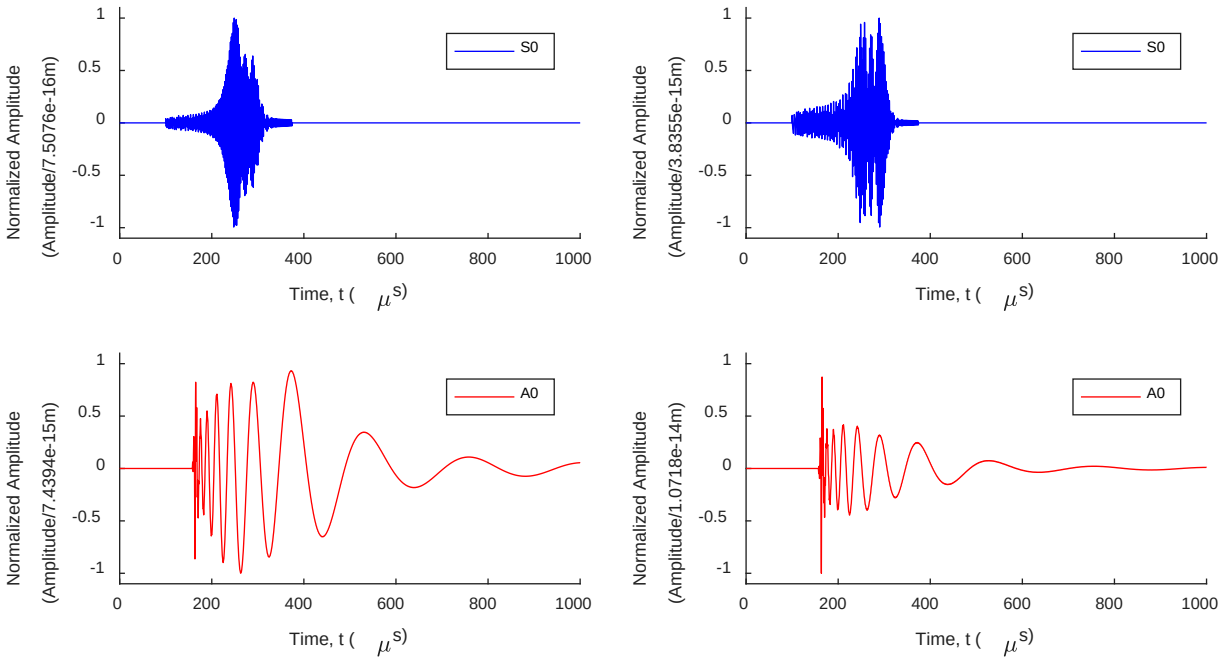

(a) (b)

Figure 12 Lamb waves (S0 and A0 mode) and bulk waves propagation at 500 mm distance in 6 mm 304-steel plate for (a) pressure potential excitation (b) shear potential excitation (peak time = 3 μs) located at 1.5 mm depth from top surface.

It can be inferred from the figures that both A0 and S0 are dispersive. Figure 12b shows the Lamb wave (S0 and A0 mode) and bulk wave propagation using shear potential only. Peak amplitude of A0 is higher than peak S0 amplitude while using shear potential only (Figure 12b). By comparing Figure 12a and Figure 12b the important observation can be made as, pressure excitation potential has more contribution to the peak S0 amplitude over shear excitation potentials whereas, shear excitation potential has more contribution to the peak A0 amplitude. However, their contribution to the S0 and A0 peak amplitude might change due to change in source depth and propagating distance. The notable characteristic is that, peak amplitude of A0 is higher than the peak S0 amplitude for both excitation potentials.

1.3.3 Electromechanical impedance spectroscopy (EMIS)

This section presents numerical results of E/M impedance /admittance of circular PWAS transducer influenced by increasing temperature. Driving parameters for E/M impedance and admittance are density, Poisson's ratio, elastic compliance, mechanical loss factor, dielectric constant, dielectric loss and in plane piezoelectric constant. It is very difficult to measure all the PWAS transducer material properties (e.g. elastic coefficient) experimentally. A proper numerical model is essential to understand effect of PWAS transducer material properties on E/M impedance/admittance with temperature. For E/M impedance/admittance modeling based on Eqs. (9) and (10), the material properties were taken Table 1and Table 2.

$$\text{Admittance}: \quad \overline{Y}(\omega) = i\omega\overline{C}\left[1-\overline{k}_p^2\left(1-\frac{(1+\upsilon)J_1(\overline{z})}{\overline{z}J_0(\overline{z})-(1-\upsilon)J_1(\overline{z})}\right)\right] \tag{9}$$

$$\text{Impedance}: \quad \overline{Z}(\omega) = \frac{1}{i\omega\overline{C}}\left[1-\overline{k}_p^2\left(1-\frac{(1+\upsilon)J_1(\overline{z})}{\overline{z}J_0(\overline{z})-(1-\upsilon)J_1(\overline{z})}\right)\right]^{-1} \tag{10}$$

where, $\overline{k}_p^2 = \frac{2}{(1-\upsilon)}\frac{d^2{}_{31}}{\overline{s}_{11}^E\overline{\varepsilon}_{33}^T}$; $\overline{C} = \overline{\varepsilon}_{33}^T\frac{\pi a^2}{t_a}$; $\overline{c}_p = \sqrt{\frac{1}{\rho\overline{s}_{11}^E(1-\upsilon^2)}}$; $\overline{z} = \frac{\omega a}{\overline{c}_p}$

a = radius of the PWAS transducer, t_a =thickness of the PWAS transducer and ρ =density of the PWAS transducer, d_{31} =in-plane piezoelectric coefficient, $\overline{s}_{11}$ = complex compliance coefficient, υ = Poisson ratio, $J_0(\overline{z})$ and $J_1(\overline{z})$ are the Bessel functions of order 0 and 1, ω is the angular frequency. Complex compliance and dielectric constant can be expressed as

$$\overline{s}_{11}^E = s^E{}_{11}(1-i\eta) \tag{11}$$

$$\overline{\varepsilon}_{11}^E = \varepsilon^E{}_{11}(1-i\delta) \tag{12}$$

where η & δ are dielectric and mechanical loss factor respectively.

Figure 13 (a) and (b) show the numerical results for E/M impedance and admittance. For numerical model density, Poisson's ratio, dielectric constant, dielectric loss, in plane

piezoelectric constant and elastic compliance were initially taken from manufacturer data sheet and experimental results. One important observation is that during numerical model the mechanical loss factor for admittance model is higher than for the impedance model. During the resonance the transducer goes through mechanical friction and contributed to more dissipation loss. During anti-resonance the transducer moves hardly resulting in very little mechanical friction and thus it showed very low mechanical loss. Mechanical loss factors are related with the quality factor.

In a nutshell, the major observations from numerical results are:

1. The degraded mechanical, electrical, and piezoelectric properties of PWAS transducer were used to simulate the temperature effects on E/M admittance and impedance peaks.
2. Density, Poisson's ratio and compliance coefficient is similar for both impedance and admittance model. Density, Poisson's ratio decreases with increasing temperature and compliance coefficient increases with temperature.
3. Mechanical loss factor for admittance model is higher than for the impedance model. Mechanical loss factor is directly proportional to the inverse of quality factor during resonance. However, mechanical loss factor is not directly proportional to the inverse of quality factor rather, it depends on other losses.

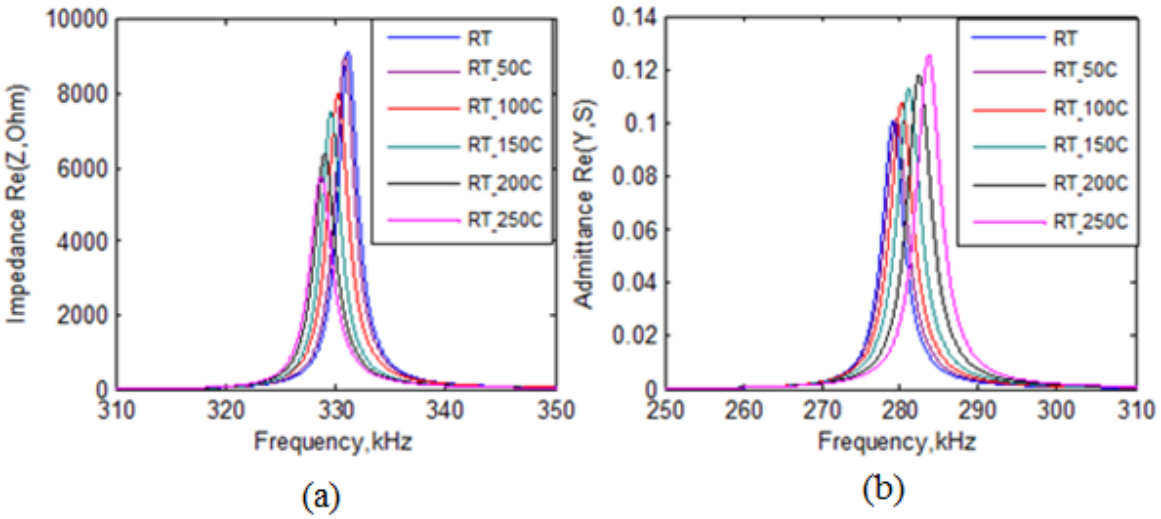

Figure 13 Impedance and admittance: (a) experimental E/M impedance (b) experimental E/M admittance (c) analytical E/M impedance (d) analytical E/M admittance of PWAS transducer after exposure to different temperature.

Table 1 Modified material properties for E/M impedance modeling to match experimental results.

Temperature (^oC)	Density (kg/m^3)	Poisson's ratio ν	s_{11} ($x10^{-12}$ m^2/N)	Mechanical loss factor (η^{AR}) %	Dielectric constant	Dielectric loss (δ^{AR}) %	Piezoelectric coefficient (d_{31}) ($x10^{-12}$)
RT	7600	0.350	17.2	0.01	1900	1.6	-185
50	7580	0.351	17.22	0.01	1920	1.62	-186
100	7550	0.352	17.25	0.015	1950	1.75	-188
150	7520	0.354	17.28	0.015	2050	1.78	-189
200	7500	0.356	17.30	0.03	2200	1.85	-190
250	7450	0.358	17.35	0.05	2300	1.89	-192

Table 2 Modified material properties for E/M admittance modeling to match experimental results.

Temperature (^oC)	Density (kg/m^3)	Poisson's ratio ν	s_{11} ($x10^{-12}$ m^2/N)	Mechanical loss factor (η^{R}) %	Dielectric constant	Dielectric loss (δ^{R}) %	Piezoelectric coefficient (d_{31}) ($x10^{-12}$) m/V
RT	7600	0.350	17.2	1.2	1950	1.7	-160
50	7580	0.351	17.22	1.25	2000	1.8	-165
100	7550	0.352	17.25	1.28	2200	1.82	-170
150	7520	0.354	17.28	1.30	2300	1.84	-175
200	7500	0.356	17.30	1.32	2400	1.86	-180
250	7450	0.358	17.35	1.33	2500	1.88	-185

In summary, the analytical wave propagation model was considered on thick steel plates. The phase velocity dispersion curve and tuning curves using piezoelectric wafer active sensors (PWAS) were generated by considering higher propagating modes in the thick structure. The objective is to demonstrate that wave propagation modelling can improve the physical understanding of guided wave can provide a monitoring strategy for damage detection. The simulation results are validated experimentally.

The guided waves generated by an acoustic emission (AE) event were analyzed through a Helmholtz potential approach. The inhomogeneous elastodynamic Navier-Lame equation was expressed as a system of wave equations in terms of unknown scalar and vector solution potentials, and known scalar and vector excitation potentials. The solution was readily obtained through direct and inverse Fourier transforms and application of the residue theorem. The resulting solution took the form of a series expansion containing the superposition of all the

Lamb waves modes and bulk waves existing for the particular frequency-thickness combination under consideration. A numerical study of the AE guided wave propagation in a 6 mm thick 304-steel plate was conducted in order to predict the out-of-plane displacement that would be recorded by an AE sensor placed on the plate surface at some distance away from the source.

A numerical model was developed for EMI based SHM technique for high temperature applications. Numerical results show that the impedance and admittance strongly depends on elastic coefficient, dielectric constant, dielectric loss tangent, mechanical loss and in-plane piezoelectric constant that can change significantly after high temperature exposure. The change in material properties of PWAS transducer are responsible for changing in amplitude and frequency of the peak amplitude of impedance or admittance. A tentative statistical analysis was conducted to find sensitivity of resonance and anti-resonance frequencies and amplitudes with temperature. Resonance frequency and anti-resonance frequency shows less sensitive to temperature than the corresponding amplitudes.

2 TECHNICAL ACCOMPLISHMENT 2: ASSESS NUCLEAR DCSS ENVIRONMENTAL EFFECTS ON THE PROPOSED SENSORS AND SENSING SYSTEM

2.1 GOAL OF THE REPORTED WORK

The goal is to evaluate the sensors and sensing system under harsh nuclear environments to determine the effects of DCSS environments including high temperature (up to 400 $^{\circ}$C) and radiation. This purpose is to provide the guidance for applying the designed SHM system on the target DCSS.

2.2 ACCOMPLISHMENT UNDER THIS GOAL

E/M impedance/admittance response of free PWAS transducer after exposure to various high temperature environments (50ºC to 250ºC) was investigated. Both frequency shift and amplitude change in E/M impedance/admittance were observed due to change in PWAS transducer material state. Peaks in the impedance/admittance signature depend on material properties such as stiffness coefficient, piezoelectric constant, dielectric constant and density. The change in dielectric properties, piezoelectric constant and elastic coefficients may be due to extrinsic response originating from domain wall motion without changes in microstructure or crystal structure.

To develop proper SHM techniques for dry cask storage canister (DCSC), electro-mechanical impedance and admittance (EMIA) response of free PWAS transducers were evaluated after gamma radiation exposure. Piezoelectric material degradation of PWAS transducers were observed due to gamma radiation exposure. Values of anti-resonance and resonance frequencies decrease logarithmically as radiation dose increases.

Scanning Electron Microscopy (SEM) was used to examine the microstructure of the PWAS transducer material and no change in microstructure was observed. X-ray powder diffraction (XRD) spectrum was examined to see the change in crystal structure, unit cell dimension, and

symmetry. No significant change in crystal structure, unit cell dimension, and symmetry was observed after exposure to high temperature and radiation.

2.3 DISSEMINATION OF THE RESULTS

For SHM applications it is important to evaluate the sensors and sensing system under harsh nuclear environments to determine the effects of DCSS environments including high temperature (up to 250 ^{o}C) and radiation. PWAS transducers are very small, lightweight and inexpensive transducers. PWAS transducers can be bonded on a host structure or between layers of a structure easily. PWAS transducers require low power, which enables it to be feasible for onsite inspection in SHM and NDE applications.

The aim of this task is to measure irreversible response and to examine the PWAS transducer microstructure, crystal structure after exposure to elevated temperature and radiation. For temperature dependent study, circular PWAS transducers were exposed to temperatures between 50^{o}C and 250^{o}C at 50^{o}C intervals. The material properties of PWAS transducer were measured from experimental data taken at room temperature before and after high temperature exposure. Change in material properties of PWAS transducers may be explained by depinning of domains or by domain wall motion without affecting microstructure of PWAS transducer material. The degraded PWAS material properties were also determined by matching impedance and admittance spectrums from experimental results with a closed form circular PWAS transducer analytical model. For irradiation test, PWAS were exposed to gamma radiation (a) slow radiation test: 0.1 kGy/hr rate for 20 hours and (b) accelerated irradiation test: 1.2 kGy/hr for 192 hours. Electro-mechanical (E/M) impedance-admittance signatures and electrical capacitance were measured to evaluate the PWAS performance before and after gamma radiation exposure. The piezoelectric material was investigated microstructurally and crystallographically by using scanning electron microscope, energy-dispersive X-ray spectroscopy, and X-ray diffraction methods.

2.3.1 High temperature effect

E/M impedance/admittance and different material properties of a set of six nominally identical free PWAS transducers were measured at room temperature after exposure to various high temperature values. The following experimental procedure was followed.

1. E/M impedance/admittance and different material properties of free PWAS transducers were measured at baseline room temperature.
2. PWAS transducers were heated to various temperature levels (50oC to 250oC with 50oC steps) at 1-2oC/min heating rate in an oven; then PWAS transducers were kept at that temperature for couple of hours. After exposure to that temperature, PWAS transducers were extracted from the oven and allowed to cool in air at room temperature.
3. E/M impedance/admittance and other material properties of PWAS transducers were measured again at room temperature to investigate material response of PWAS transducers.
4. Microstructural and crystallographic investigation of PWAS transducer was performed after exposure to 250oC temperature.

Experimental set up for E/M impedance/admittance measurement is shown in Figure 14. A commercial HP 4194A impedance analyzer was used for E/M impedance/admittance measurement. PWAS transducers were loaded in a test stand and connected to impedance analyzer by wires. PWAS transducers were measured in a stress-free state by using pogo pins that only apply small spring forces to the PWAS surface (Figure 14). An oven with PID temperature controller was used to elevate the PWAS to high temperature. A data acquisition system was used to collect the E/M impedance/admittance. The E/M impedance/admittance values were collected from 250 kHz to 350 kHz with a step size of 50 Hz. The real part of the impedance/admittance is used for E/M impedance/admittance method as it has been used for damage detection in SHM applications. The frequency range is determined by trial and error method and only first PWAS anti-resonance (≈ 330 kHz) and resonance (≈ 290 kHz) was considered in this article. In earlier publication by Lin et al. showed that, 1st resonance and anti-resonance spectrum shows more stable response than higher resonance or anti-resonance spectrum. In order to detect damage properly it would be recommended to follow change in frequencies of 1st resonance and anti-resonance.

Results and discussion

Peaks in the PWAS transducer E/M impedance/admittance were seen based on electromechanical coupling with mechanical impedance/admittance of the PWAS transducer. Eqs. (9) & (10) show the coupled relation between the PWAS transducer mechanical impedance and complex electrical impedance/admittance. E/M impedance/admittance spectra depend on PWAS transducer material properties such as stiffness coefficient, piezoelectric constant, dielectric constant, density and different losses in PWAS transducer material. Any kind of change in PWAS transducer material state can be noticed as peak shifts in E/M impedance/admittance. The spectral peaks observed in the real part of the E/M impedance spectrum follows the PWAS transducer anti-resonances and E/M admittance spectrum follows the resonance. Figure 15 (a) shows the E/M impedance spectra of a free PWAS transducer after exposure to different temperature and Figure 15 (b) shows the admittance spectra. In these figures, RT denotes room temperature data, RT_50 denotes as data was taken at room temperature after exposure to 50^0C, and so on. It can be seen that, for impedance spectra, both the impedance amplitude and the frequency of the peak impedance decreases with increasing temperature. In case of admittance spectra, admittance amplitude and the frequency of the peak increase with increasing temperature. So, frequency and amplitude of the spectral peaks vary with temperature, which may indicate a change in the PWAS transducer material properties.

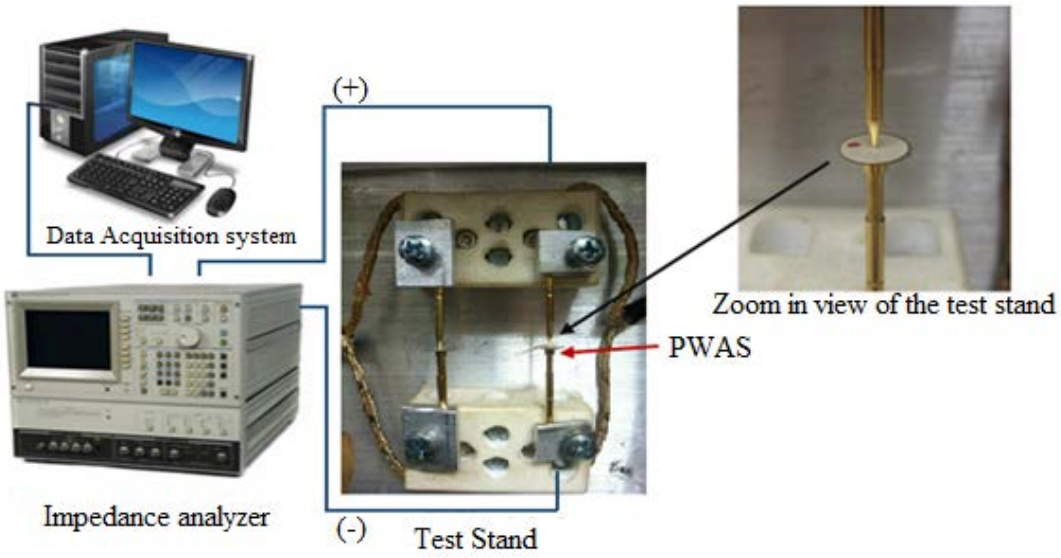

Figure 14 Experimental setup for E/M impedance/admittance measurement

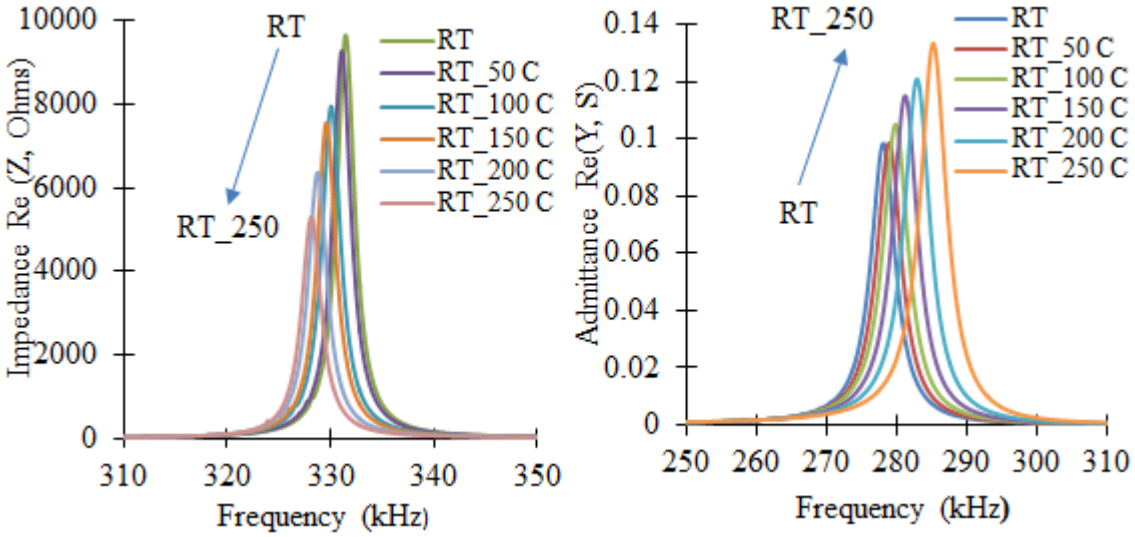

Figure 15 (a) E/M impedance and (b) E/M admittance of a PWAS transducer after exposure to different temperature.

Microstructural and crystallographic investigation

To further facilitate understanding of PWAS transducer material state, microstructural and crystallographic investigation were done. A scanning Electron Microscopy (SEM) system was used to visualize the PWAS transducer (Ag/PZT/Ag) cross section (Figure 16). PWAS transducers have a dense structure with PZT grains composed of 2-3 μm. No variation was found

in the microstructure or PZT grains in the PWAS transducer due to elevated temperature exposure (Figure 16 a and b).

Figure 17 shows the X-ray powder diffraction (XRD) spectrum for PWAS transducer material at room temperature (Figure 17a) and at room temperature after exposure to 250^{o} C (Figure 17b). XRD is a rapid analytical technique primarily used for phase identification of a crystalline material and can provide information on unit cell dimensions. XRD measures the X-ray diffraction peak with diffraction angle (2θ). Position of the peaks with diffraction angle (2θ) is the important characteristic of the XRD pattern, which act as a unique characteristic of the crystallographic unit cell. By comparing measured peak positions, change in unit cell dimension and symmetry can be obtained. Figure 17 shows no noticeable change in X-ray diffraction peak position. That means, there is no significant change in crystal structure, unit cell dimension, and symmetry after exposure to elevated temperature. Microstructural and crystallographic studies confirm that PWAS transducer can be used as a SHM transducer without any damage after heating to high temperature.

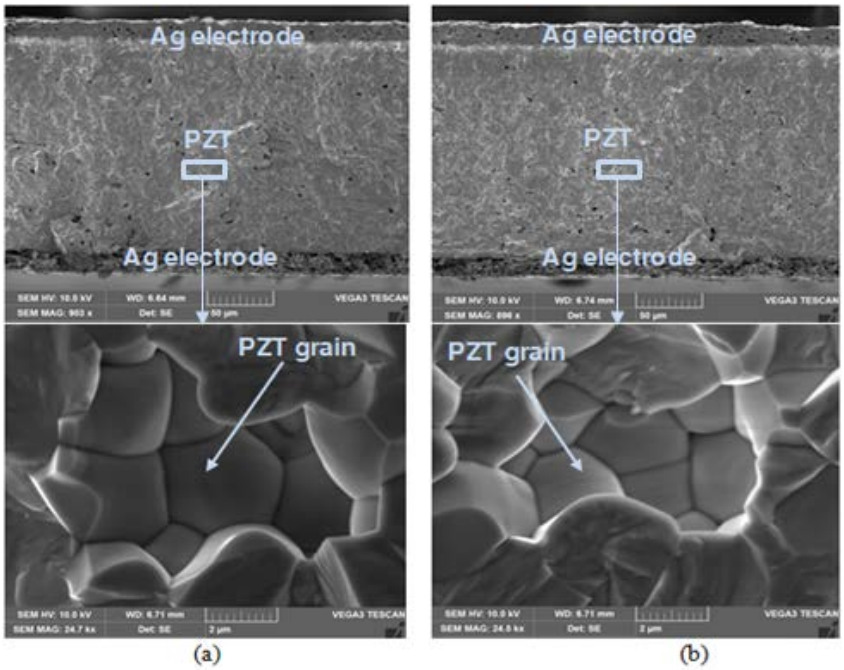

Figure 16 SEM micrograph of cross section of Ag/PZT/Ag PWAS transducer (a) at room temperature (b) at room temperature after exposure to 250^{o}C for 2 hours.

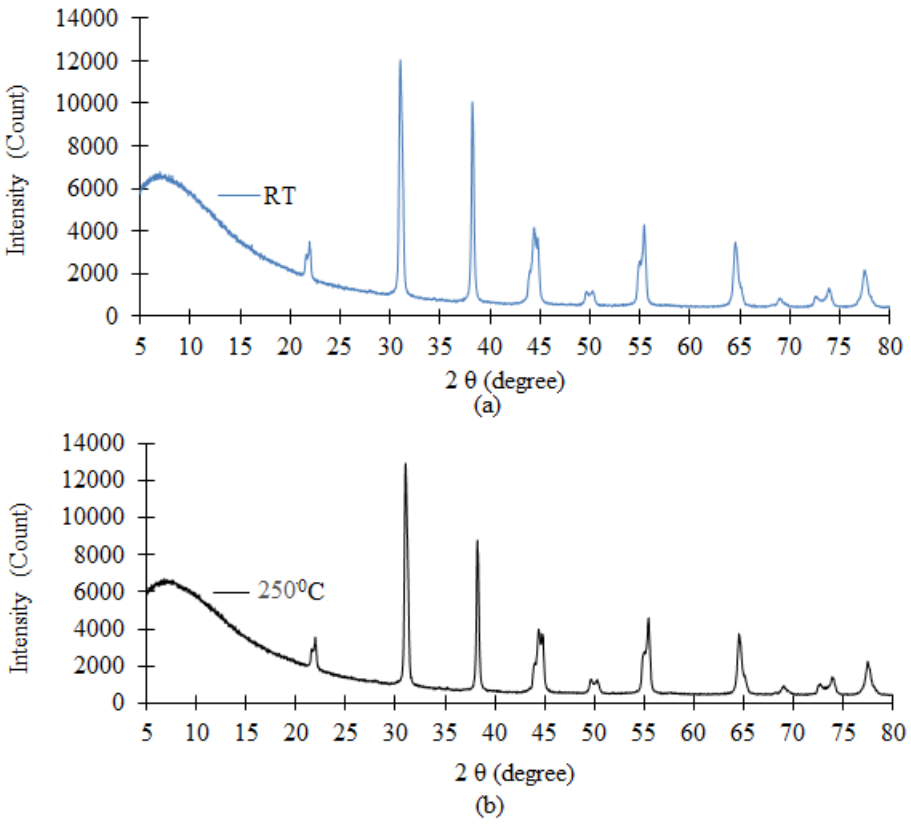

Figure 17 XRD of PWAS transducer (a) at room temperature (b) at room temperature after exposing to 250°C for 2 hours.

2.3.2 Radiation effect

For slow radiation experimental study, radiation dose was set to 0.1 kGy/hr for 20 hours (Cumulative dose: 2 kGy). PWAS were exposed to the radiation for 5 times with 4 hours for each time. A set of ten (numbered from 1 to 10) nominally identical free PWAS (PZT and GaPO4) were tested (Figure 18(a)). The irradiation test was done in a Co-60 gamma irradiator facility (by JL Shepherd and Associate) as shown in Figure 18 (b). The experimental procedure is shown in Figure 19.

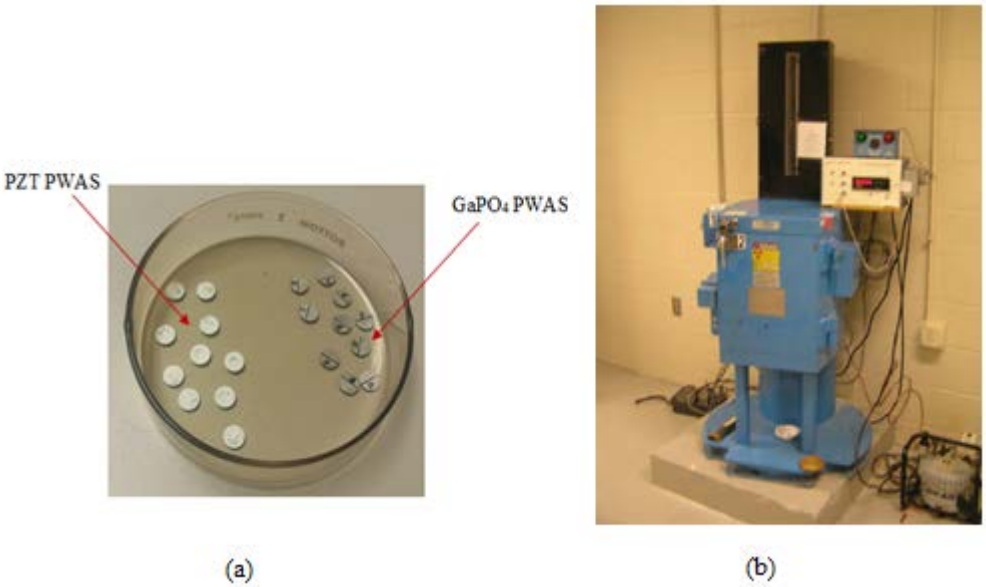

Figure 18 (a) PWAS for radiation exposure (b) JL Shepherd and associate irradiator facility

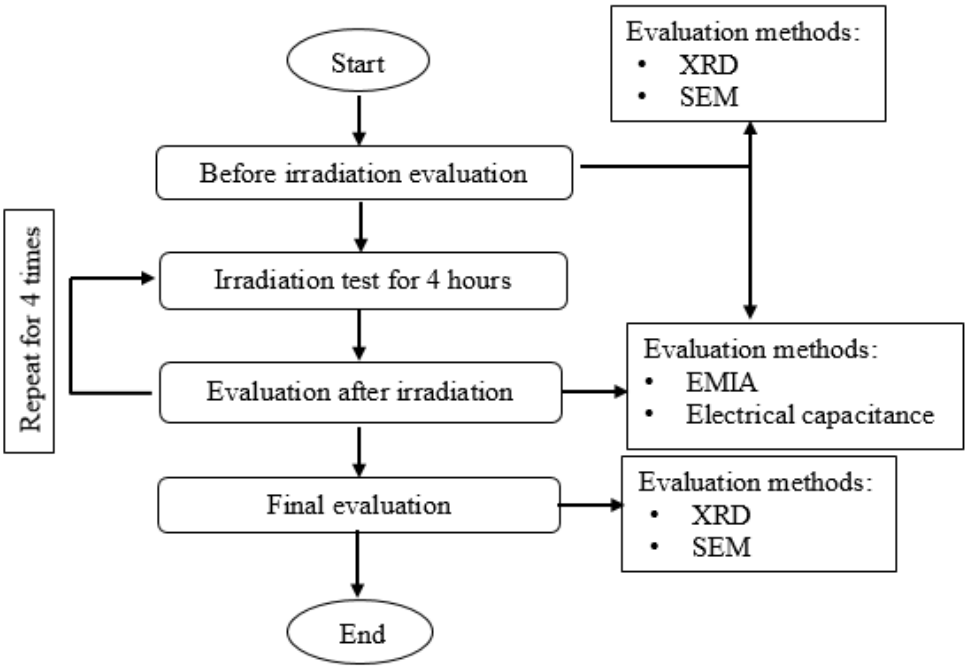

Figure 19 Experimental procedure flow chart for slow radiation test

Figure 20 Irradiator facility

For accelerated radiation experiment study, radiation dose was set to 1.233 kGy/hr for 192 hours (Cumulative dose: ~ 223 kGy). The irradiation test was done in a Co-60 Gamma Irradiator facility as shown in Figure 20. Radiation dose analysis is shown in Table 3. Last 80 hours radiation test was done only to a subset (4 samples from each group). In order to determine the stability of PWAS transducers under gamma radiation, the following experimental procedure was followed.

Step 1: Transducers were delivered to the testing laboratory for first run with the following steps

- Transducers were placed in petri dish
- Transducers were spread out well in order to be contact free from each other
- Transducers were placed at the center of the irradiator facility (dose rate: 1.233 kGy/hour)
- Transducers were exposed for 16 hours continuously
- Temperature of the sample/chamber was recorded periodically
- Transducers were extracted after the irradiation test and were kept at room temperature

Step 2: Transducers were returned back to USC-LAMSS for evaluation

- EMIA was evaluated
- Electrical capacitance was measured

Step 3: Repeat Step 1 and Step 2 for additional 16 hours.

Step 4: Intermediate evaluation

- SEM system was used to visualize the cross section of PWAS Transducer
- XRD spectrum was used to identify change in crystal structure, unit cell dimension and symmetry.

Step 5: Repeat Step 1 and Step 2 for additional 160 hours with 80 hours interval.

Step 6: Final evaluation

- SEM system was used to visualize the cross section of PWAS Transducer
- XRD spectrum was used to identify change in crystal structure, unit cell dimension and symmetry

Table 3 Radiation dose analysis for DCSC applications

Radiation rate (kGy/hr)	Radiation exposure time (hours)	Radiation exposure (kGy)	Accumulated exposure time (hours)	Accumulated radiation (kGy)	Equivalent to application dose (years)
Slow radiation test					
0.1	4	0.4	4	0.4	0.45
	4	0.4	8	0.8	0.9
	4	0.4	12	1.2	1.4
	4	0.4	16	1.6	1.82
	4	0.4	20	2.0	2.28
Accelerated radiation test					
1.23	16	19.7	36	21.7	24.7
	16	19.1	52	40.8	46.6
	80	92.7	132	133.5	152.4
	80	92.0	212	225	256

Results and discussion

Figure 21 (a)-(d) show the change of resonance frequency and amplitude for both radially and thickness vibrating PZT-PWAS transducers with accumulated gamma radiation. To facilitate the understanding the plot of PWAS EMIA with exposed radiation, slow radiation part and accelerated radiation part of the total dose is shown in Figure 21(a). In order to respond to skewness towards large radiation dose, the cumulative radiation dose values are plotted in log scale (x-axis). A small radiation exposure (~ 30 Gy) was assigned to the before radiation test data in order to plot in the log scale.

Figure 21 (a) and (c) shows the change in resonance frequency with accumulated radiation dose for in-place and thickness vibrating PZT-PWAS respectively. Whereas Figure 21 (b) and (d) shows the change in resonance amplitude with accumulated radiation dose for in-place and thickness vibrating PZT-PWAS respectively. The mean resonance frequency before radiation of radially and thickness vibrating PWAS are 287 kHz and 1134 kHz respectively. The resonance frequency (Figure 21 (a) and (c)) increases at higher rate initially but at higher cumulative radiation dose the frequency increases at slower rate. Therefore, the resonance frequency follows a logarithmic increment with radiation dose. The resonance amplitude shows the opposite phenomenon i.e., resonance amplitude decreases logarithmically with radiation dose.

However, the change in resonance frequency for thickness vibrating PZT-PWAS is significant compared to radially vibrating PZT-PWAS. Admittance of a piezoelectric sensor is proportional to capacitance, concluding that capacitance of the piezoelectric sensor decreases with increasing radiation dose.

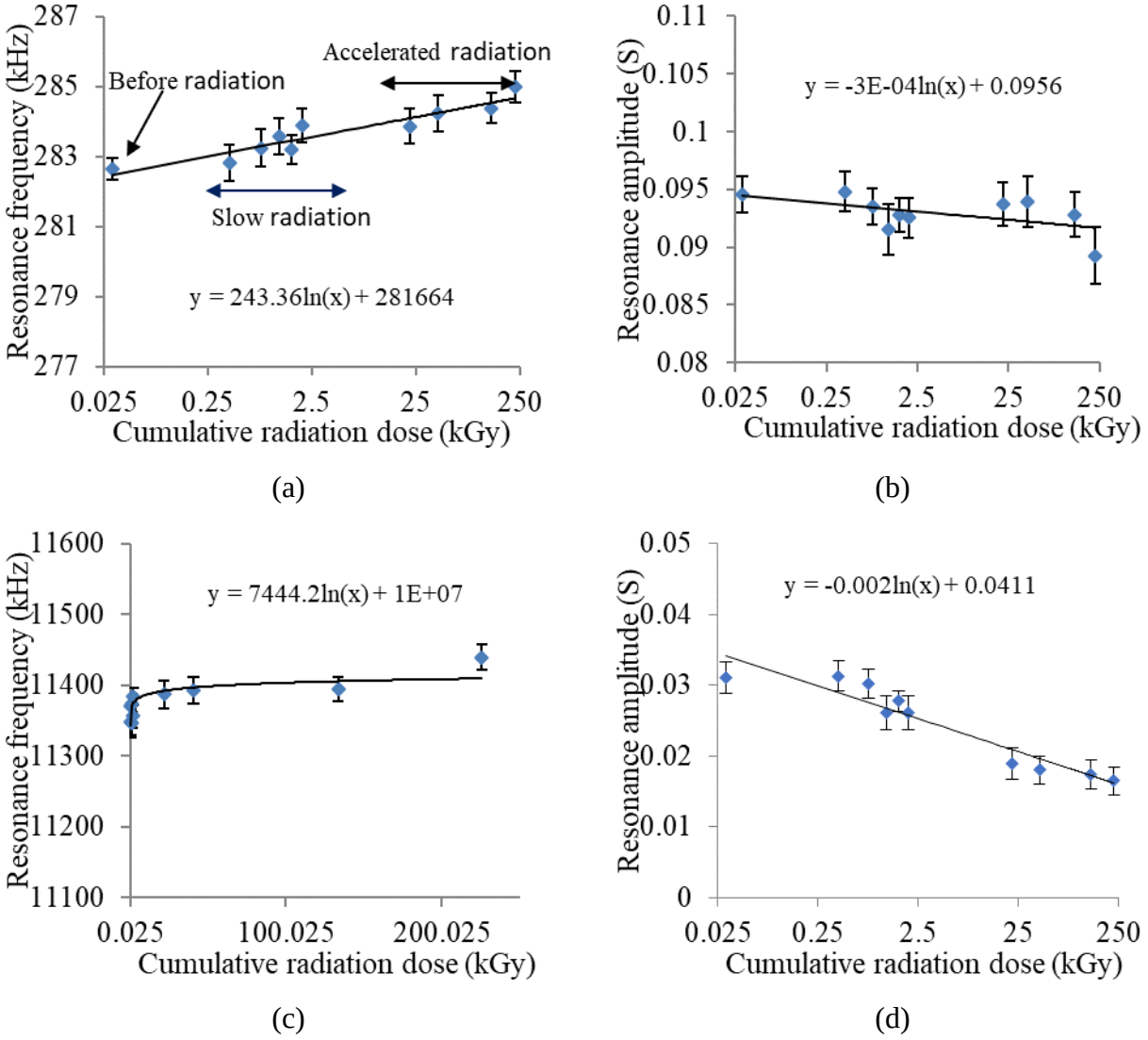

Figure 21 Change in (a) –(b) Resonance frequency and amplitude for radially vibrating PZT-PWAS; (c)-(d) Resonance frequency and amplitude for thickness vibrating PZT-PWAS; with cumulative gamma radiation dose.

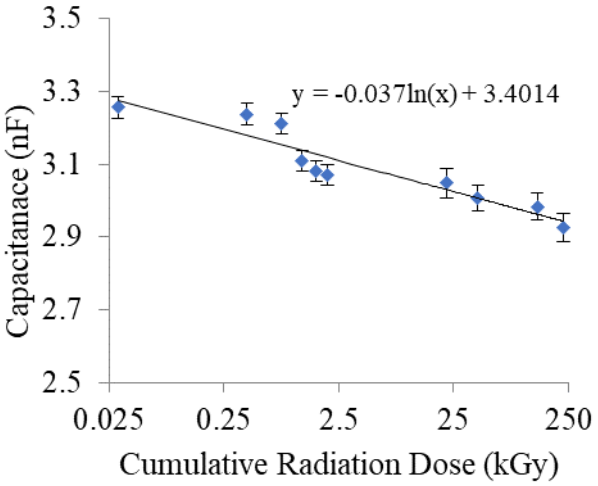

Figure 22 Electrical capacitance of PZT-PWAS with cumulative radiation.

Figure 22 shows the change in electrical capacitance after exposure to different radiation dose. Electrical capacitance decreases logarithmically as radiation absorbed dose increases. Many researchers have reported decreasing capacitance value with increasing radiation dose. Several polarization mechanisms are responsible for changing the dielectric response. Among them, pinning of domain is the key factor to the change the dielectric response of PZT-PWAS transducer.

Figure 23 (a) and (c) show the change of resonance frequency with radiation for in-plane and thickness modes respectively. The resonance frequency increases slightly with increasing exposed radiation dose whereas, the resonance amplitude decreases with increasing exposed radiation dose. However due to large scatter of resonance amplitude between the samples resulting a large standard error (error bar). Due to high electrical resistivity of $GaPO_4$-PWAS, it shows very low resonance amplitude (Figure 23 (b)). The change in resonance frequency and amplitude can be explained by the role of Ga–O-P interactions. The Ga–O and P–O distances may contract due to radiation exposure, based on the ionic radii it may change Ga–O–P angle. The change in Ga-O-P angle may contribute to change in capacitance and piezoelectric performance as well as mechanical and electrical loss. Figure 24 shows the change in electrical capacitance of $GaPO_4$-PWAS with cumulative radiation dose. The capacitance value decreases with increasing radiation dose. The resonance amplitude is proportional to capacitance therefore; decreasing resonance amplitude with increasing radiation dose is expected.

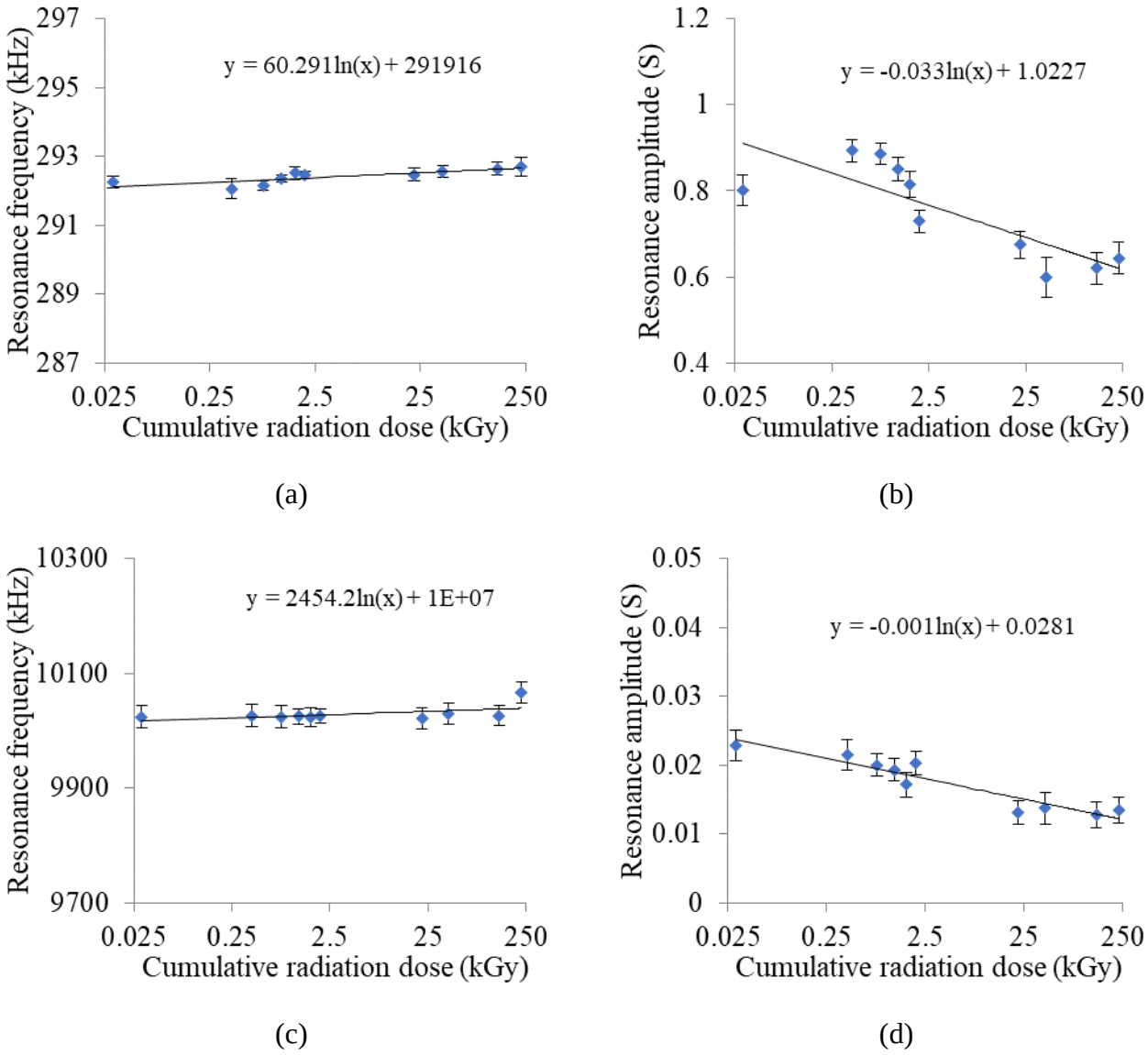

Figure 23 Change in (a) –(b) Resonance frequency and amplitude for radially vibrating $GaPO_4$ PWAS; (c)-(d) Resonance frequency and amplitude for thickness vibrating $GaPO_4$ PWAS; with cumulative gamma radiation dose.

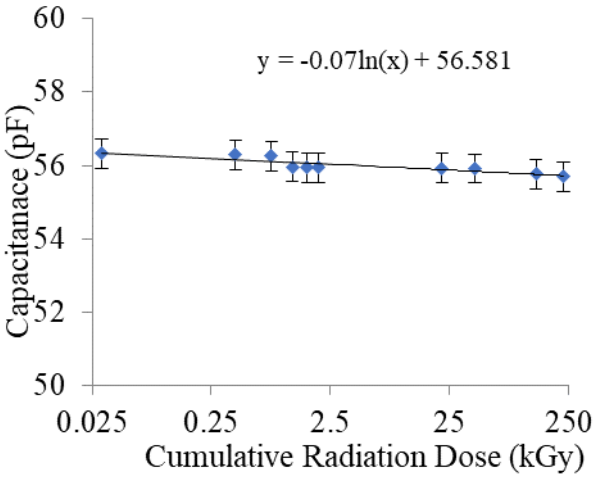

Figure 24 Electrical capacitance of $GaPO_4$-PWAS with cumulative radiation.

Microstructural and crystallographic investigation

This section investigates the microstructure and crystal structure of the PWAS transducers. The microstructure of the PWAS was examined using scanning electron microscopy (SEM) where, crystal structure was investigated by X-ray diffraction (XRD) method. SEM and XRD examinations were performed on four cases (a) before exposure to radiation (b) after 225 kGy radiation exposure.

SEM images of PWAS transducers (Ag/PZT/Ag and Pt/$GaPO_4$/Pt) cross section are shown in Figure 25 and Figure 26. PZT-PWAS transducer has two Ag electrodes on top and bottom with multi domain PZT in between them (Figure 25). $GaPO_4$ has also two Pt electrodes on top and bottom with single crystal $GaPO_4$ in between them (Figure 26). No significant variation was found in the microstructure (PZT grains and $GaPO_4$ single crystal) PWAS transducers due to radiation exposure. Figure 27 and Figure 28 show the X-ray powder diffraction (XRD) spectrum for PWAS transducers material. The important feature of the XRD measurement is X-ray diffraction peak with diffraction angle (2θ). Any change in the crystal structure shifts the peak with diffraction angle (2θ). Figure 27 show no significant change in X-ray diffraction peak position of PZT-PWAS transducer material. Figure 28 shows that the overall XRD patterns of $GaPO_4$-PWAS transducer material remain the same before and after radiation exposure. SEM and XRD studies confirm that, there was no significant variation in PWAS transducer microstructure and crystal structure.

(a) Before irradiation

(b) After 225 kGy

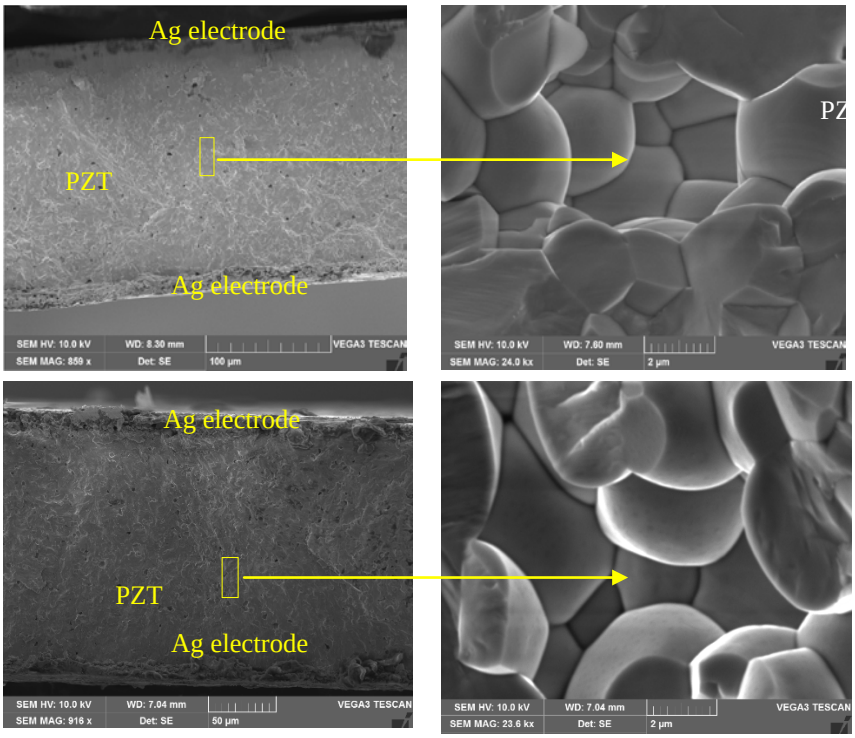

Figure 25 SEM micrograph of cross section of Ag/PZT/Ag PWAS transducer (a) before irradiation (b) after slow irradiation (2 kGy) (c) after accelerated irradiation of 40.7 kGy (d) after accelerated radiation of 225 kGy.

(a) Before irradiation

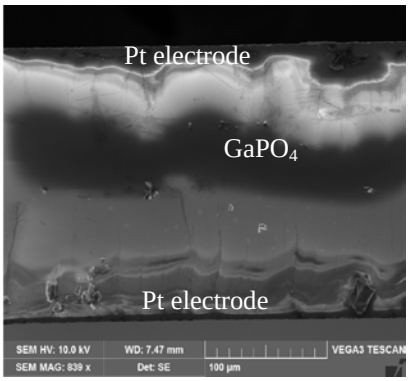

(b) After 225 kGy

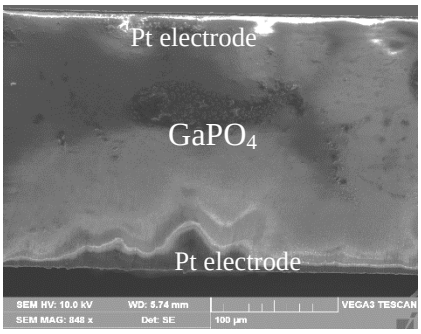

Figure 26 SEM micrograph of cross section of Pt/$GaPO_4$ /Pt PWAS transducer (a) before irradiation (b) after slow irradiation (2 kGy) (c) after accelerated irradiation of 40.7 kGy (d) after accelerated radiation of 225 kGy.

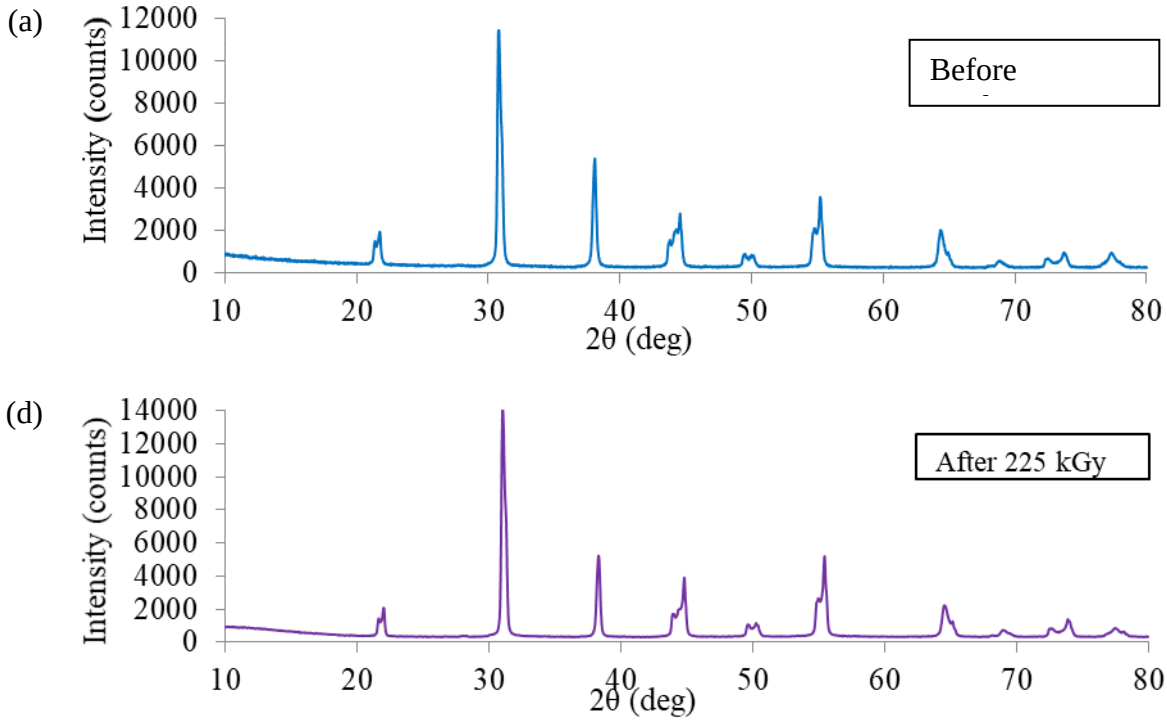

Figure 27 XRD of PZT-PWAS transducer (a) before irradiation (b) after 2 kGy radiation (c) after 40.7 kGy radiation (d) after 225 kGy radiation

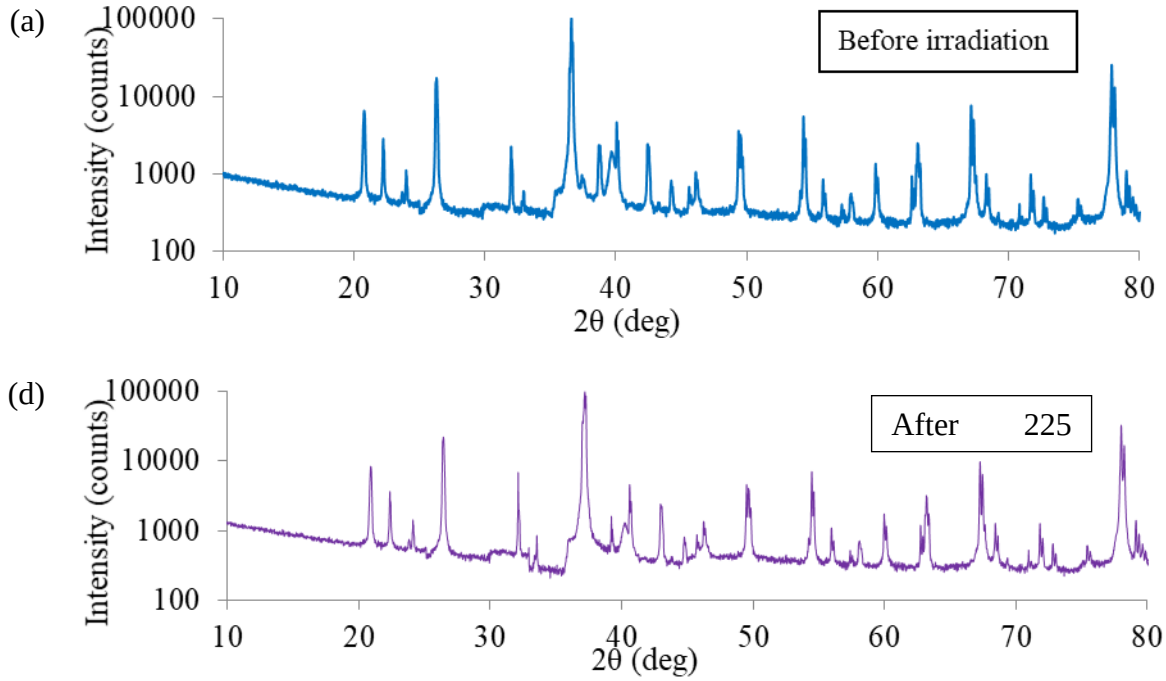

Figure 28 XRD of $GaPO_4$-PWAS transducer (a) before irradiation (b) after 2 kGy radiation (c) after 40.7 kGy radiation (d) after 225 kGy radiation

2.3.3 High Temperature piezoelectric sensors

Literature review of several high temperature materials has been conducted and reported here.

High temperature piezoelectric materials: yttrium calcium oxyborate (YCOB)

Recently discovered piezoelectric single crystal yttrium calcium oxyborate YCa4O(BO3)3 (YCOB) is known for its stable electromechanical and piezoelectric properties across a broad temperature range, and the absence of phase transitions up to its melting point (1500 °C) [33]-[35]. Together with its high resistivity at elevated temperatures, YCOB has been reported as a promising high temperature sensing crystal [35]. But YCOB sensor has a limitation of degradation of platinum thin film electrodes [34].

Johnson et al. introduced YCOB sensor for high-temperature acoustic emission (AE) sensing [37]. The YCOB AE sensor was constructed using materials that could withstand the maximum temperature of 1000 °C. Based on material properties and the design of YCOB accelerometer presented by Kim et al. [38]. Inconel was chosen as the electrode and wire material. The sensor consisted of a top electrode, an aluminum insulator pad, and the piezoelectric crystal. The sensor can also be placed on a structure with a clamp, as shown in Figure 29. In this configuration, a 316 stainless steel clamp was used, which has a critical operating temperature at around 1000°C.

And also the clamp can be used for intermittent time intervals due to its destructive scaling temperature of about 1100 °C. In this study, YCOB sensor of dimension of 8×6×2 (unit: mm) was placed on a 309 stainless steel bar. The bar structure acts as the bottom electrode for the sensor. The specimen with the YCOB sensor was tested inside of a furnace (GSL1100X, MTI Corp). An alumina insulator pad of dimensions of 10×8×1 (unit: mm) was used to isolate the top electrode from the clamp. This sensor was also used for the room-temperature testing so that frequency and amplitude wave characteristics of the sensor at room temperature and elevated temperatures can be evaluated.

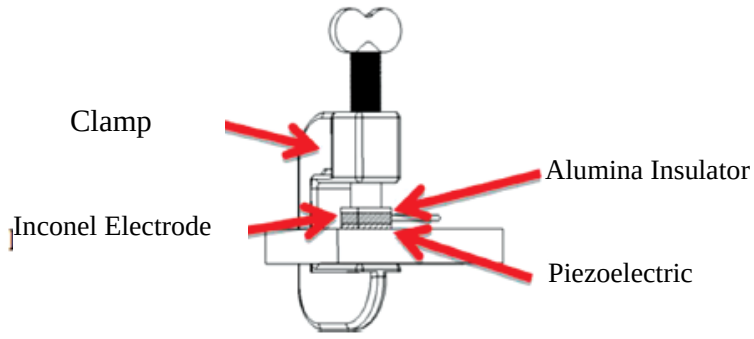

Figure 29: Illustration of high-temperature sensor design used in the experiments

The Hsu-Nielsen test was conducted at both room and high temperature at 1000 °C to evaluate the YCOB sensors for AE sensing. At room temperature, two types of AE sensors were used, one made of YCOB crystal, and another of PMN-PT crystal which has a much higher sensitivity at room temperature [39],[40]. The distance of sensors and the AE signal source was 20 cm. Because of the differences in the magnitude of the piezoelectric constants of the two crystals, the YCOB AE sensor signal was amplified by 100 times with the charge amplifier, and the PMN-PT AE sensor signal was not amplified. Waveforms and their corresponding frequency spectra were given in Figure 30. Symmetric and antisymmetric wave modes can be easily recognized in the waveforms in time domain. The time domain signal was also analyzed in the frequency domain by performing a fast Fourier transform, and finding the PSD. The earlier time of arrival of a higher frequency signal, preceding a lower frequency signal is in agreement with the dispersion curves. The frequency signal and time of arrived of zero-order mode from YCOB AE sensor were almost consistent with those from PMN-PT sensor. The ability to detect the Lamb wave modes displayed by the YCOB AE sensor is very promising for AE sensor applications.

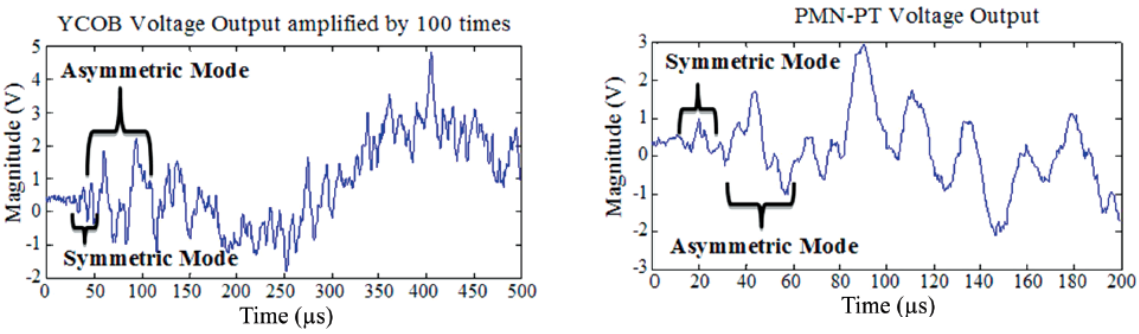

Figure 30: Response of YCOB and PMN-PT sensors to Hsu−Nielsen test at room temperature (time domain)

High temperature piezoelectric materials: Lithium Niobate (LiNbO3)

For Lithium Niobate (LiNbO3), the Curie temperature of it has been reported to be about 1,150 °C with high electromechanical coefficients [42]. The pyroelectric effect and the propagation of LiNbO3 losses are lower at elevated temperature and it has no phase transition up to about 1100 °C [43],[44]. However, practically, this material is limited to 600 °C due to chemical decomposition (starting at 300 °C), increased attenuation and intergrowth transition, loss of oxygen to the environment, and limited resistivity. LiNbO3 also suffers from a short lifetime at elevated temperatures [42]-[44].

Kirk *et al*. presented high-temperature-resistant piezoelectric sensors which had been tested as acoustic emission sensors over a temperature range from room temperature up to 400 ° . The sensors were made from lithium niobate 1-3 piezocomposites using the dice and fill method, with high-temperature-resistant cement. The sensors were tested for AE sensing on a steel block of dimensions 130.0 × 9.2 × 48.5 (unit: mm). Figure 31 showed the mounting and connection of the piezocomposite on the test sample. The steel test block itself served as the ground connection to the device. The positive electrical connection was provided by a screen-printed conductive electrode on a high temperature-resistant alumina substrate. High-temperature couplant UCA-HT (200-600°C, by Ely Chemical) was used for avoiding the air. Three types of piezocomposite sensors which were made from 4 mm and 2 mm-thick y/36°-cut and 4 mm z-cut lithium niobate piezocomposites were used to record the signal for comparison. Three sensors were the same distance from the AE signal source. The AE signal was simulated using a Hsu-Nielsen source (PLB). The data are acquired by a digital oscilloscope (Agilent 54641A). All three transducers show a broadly similar response to the simulated AE signal in both the time and frequency domains. Sensor made of 4 mm y/36°-cut piezocomposite shows better sensitivity in the frequency range of the simulated AE signal and the better signal to-noise ratio than other two sensor.

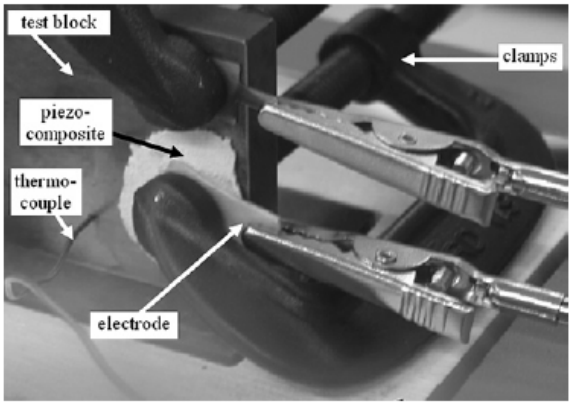

Figure 31: Lithium niobate piezocomposite mounted onto the test object (metal block standing vertically on hotplate)

For AE sensing at high temperatures, the test block was heated on a hot plate, reaching a maximum temperature of 400°C. The tests were repeated as the room temperature. PLB-AE signals were successfully detected with acceptable signal-to-noise ratio for the three different piezocomposites starting at room temperature and increasing to 400 °C, at 3 cm and 10 cm distance from the source. Results are shown for a the 4 mm-thick y/36°-cut composite, 3 cm from the source. The detected signal has a broad bandwidth and a good signal-to-noise ratio. Allowing for some variation in the signal from the AE signal source on each occasion, the signal amplitude remained approximately constant over the temperature range 25-400 °C.

Gallium orthophosphate (GaPO4) high temperature piezoelectric materials

Simple structure, fast response time, and ease of integration, all give high-temperature piezoelectric sensors (HTPES) an advantage and make them of particular interest. There are many ferroelectric/piezoelectric materials that possess high Curie temperatures that may qualify for high temperature applications. Various piezoelectric materials have been extensively researched for high-temperature applications, including gallium orthophosphate (GaPO4), Yttrium Calcium Oxyborate (YCOB) and Lithium Niobate (LiNbO3) [8]-[17]. Each of these materials has its own unique advantages and drawbacks for use as HT sensors. Among them, GaPO4 offers good temperature compensation for a new generation of crystal microbalances operating at temperatures up to at least 700 °C as shown in thermogravimetric and film thickness measurements [10],[12]. It also shows remarkable features including: higher piezoelectric effect, high electromechanical coupling constants and Q-values (ratio of reactance to resistance), existence of temperature-compensated orientations for bulk acoustic waves (BAWs) and SAWs, absence of primary pyroelectric effect, stress-induced twinning not observed, and high electric resistivity up to high temperatures [8], [9], [12]-[15]. In particular, GaPO4 shows no pyroelectricity, a high electric resistivity to guarantee high precision piezoelectric measurements. Hence, its high thermal stability and good sensitivity make it a very attractive choice for a wide range of high temperature applications [8].

GaPO4 belongs to the same point group as quartz. Compared to quartz, the piezoelectric constant d11 of GaPO4 shows no measurable deviation up to 700 °C from its room temperature value which is about twice that of quartz [9],[15]. Krempl et al. studied GaPO4 and compared the temperature dependence of the most important piezoelectric constant d11 with that of quartz in Figure 32 and found GaPO4 can survived up to 930. GaPO4 sensors have been manufactured since 1994 and are now well established in the market [28]. They have shown to be a promising candidate for HT sensors [8],[13],[28]. However, there are some disadvantages with GaPO4. As compared with bismuth titanate its sensitivity is significantly lower [9]. And also GaPO4 fairly sharp resonances and significantly lower viscosities compared to other high-temperature piezoelectric materials [22]. It is limited to operation temperatures below 700 °C because of decreased mechanical quality factor due to increased structural disorder, limiting its usage at extreme high-temperatures [16, 18].

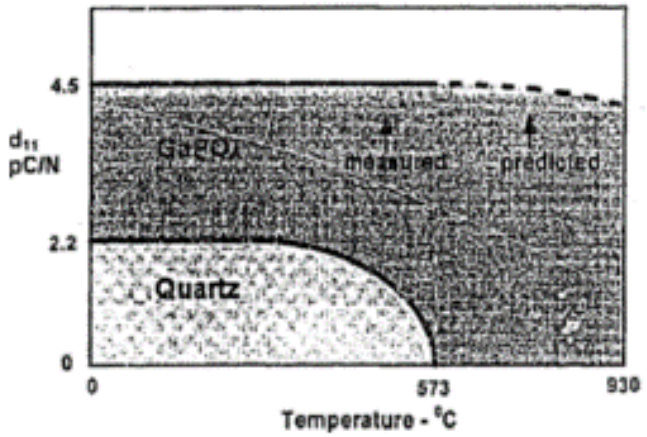

Figure 32: Temperature dependence of the piezoelectric effect d_{11} of quartz and gallium orthophosphate [1]

High temperature sensor development

Sensors consist of the piezoelectric material as well as the electrodes, adhesive, wire, and connections. Therefore in order to achieve successful high-temperature performance, all these components besides the sensing materials must be able to work in the high-temperature environment.

Thin film electrodes (~100 nm thickness) are commonly used for piezoelectric devices to apply an electric field or to obtain a generated charge signal [11]. In order to be effectively used in high-temperature sensors, these thin film electrodes should be capable of long term high-temperature operation [21],[22]. Various thin film electrodes, including platinum (Pt), Pt-based alloys, and other metallic alloys or conductive ceramic electrodes have been researched for high-temperature sensing applications [4]. Platinum thin film electrodes are popular for both low and high-temperature sensors due to their excellent electrical properties, high melting point and outstanding oxidation resistance [26],[30]. Nevertheless, there are some limitations to its application at temperatures higher than 650 °C because of platinum thin films' degradation

phenomena as a result of agglomeration, recrystallization, and dewetting effects [31]. Xu et al. introduce a Pt electrode using in the high temperature test. In his experiment, Pt and Nickel (Ni) wires of 0.01in. (25mm) and 0.02in. (50mm) diameter were selected for wiring. This work showed that Pt electrode can survive up to 1300 °F [13].

Hamidon et al. have developed a high-temperature surface acoustic wave device using gallium orthophosphate (GaPO4) with operating frequency of 434 MHz and temperatures up to 600 °C [32]. Interdigital transducers (IDTs) were fabricated using an e-beam lithography coupled with a lift-off technique on the GaPO4 crystal plate. Pt was used for the electrode due to its high melting temperature (1,768.3 °C), high resistance to oxidation and almost constant bulk resistance temperature coefficient. Titanium (Ti) or zirconium (Zr) was chosen as an adhesion layer. The sensor was bonded using Pt wire and attached to a stainless steel substrate for high-temperature tests. The long-term stability was investigated. The S11 parameters which indicates the sensor performance was measured as a function of frequency at 600 °C for 301 h. The stable S_{11} curves (Figure 33) showed the Pt electrode, Ti, Zr adhesive layer can survive up to 600 °C.

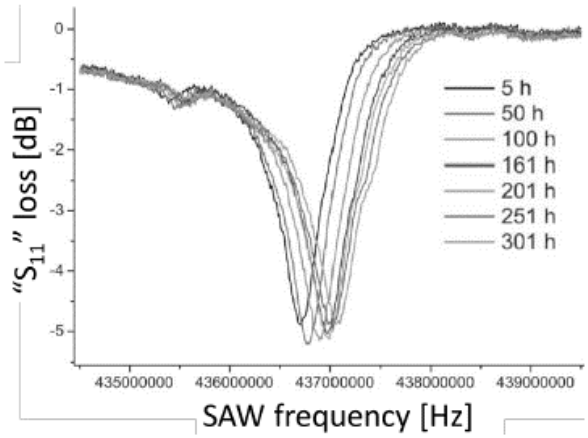

Figure 33: The S11 parameters measurement results as a function of frequency at 600 °C for 301 h [32]

Xu et al. selected the high temperature wiring, adhesive and connection for their experiment. The GaPO4 sensor was bonded to the disk with Cotronics 989 high-temperature adhesive. A nickel (Ni) wire was bonded with PryoDuct597A to the center of Pt electrode on the GaPO4. Another Ni wire was welded with a Unitek Equipment 60W.s spot welder to the edge of the Titium disk acting as electrical ground. The Ni wire was also affixed to the Ti disk with Cotronics 989 to ensure mechanical reliability. All of this were put in the oven, and the oven temperature was gradually increased from room temperature to 1300 °F (705 °C). The GaPO4 sensor, PryoDuct 597, Cotronics 989 adhesive and wiring can survive oven high temperature.

GaPO4 as HT-PWAS

Giurgiutiu et al. presented a preliminary study of GaPO4 evaluation as high temperature piezoelectric active sensor (PWAS) and found the sensor can survive high temperature up to

1300 °F [13]. The GaPO4 sensors were x-cut single crystals and made in wafer form of 7 mm diameter and 0.2 mm thickness (Figure 34). Platinum layers of 100 nm thickness were sputtered on as the electrodes. Cotronics 989 high-temperature adhesive is used to bond the GaPO4 sensors on host structure for sensing. Electromechanical impedance (EMI) of free and bonded GaPO4 were tested at different temperature to evaluate the GaPO4 HT-PES performance and survivability at high temperatures. In this study, free sensors were evaluated after exposure to high temperature while the bonded ones were tested in-situ when they were in the oven.

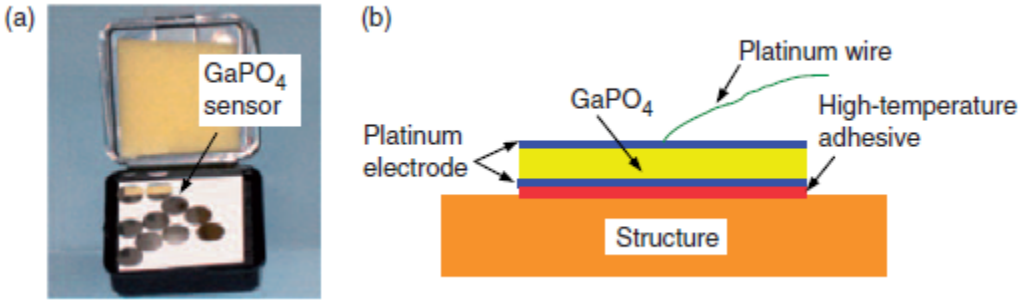

Figure 34: GaPO4 sensors: (a) photo of sensor and (b) schematic of sensor bonded on structure

For free GaPO4, EMI after exposing to increasing temperatures (RT, 200 °F, 400 °F, 600 °F, 800 °F, 1000 °F, 1200 °F, and 1300 °F) were measured and evaluated. Each oven exposure lasted 30 min, after which the sensors were taken out from the oven cooling down to RT in air, and then EMI was taken. Figure 35 showed impedance spectra of free GaPO4 HT-PES at various temperatures. It can be seen that the free GaPO4 HT-PES showed strong spectral peaks after oven exposure to 1300 °F (705 °C). The spectra also showed little change of the frequency locations of the strong spectral peaks, which indicates the GaPO4 HT-PES maintained the piezoelectric properties after the high temperature exposure.

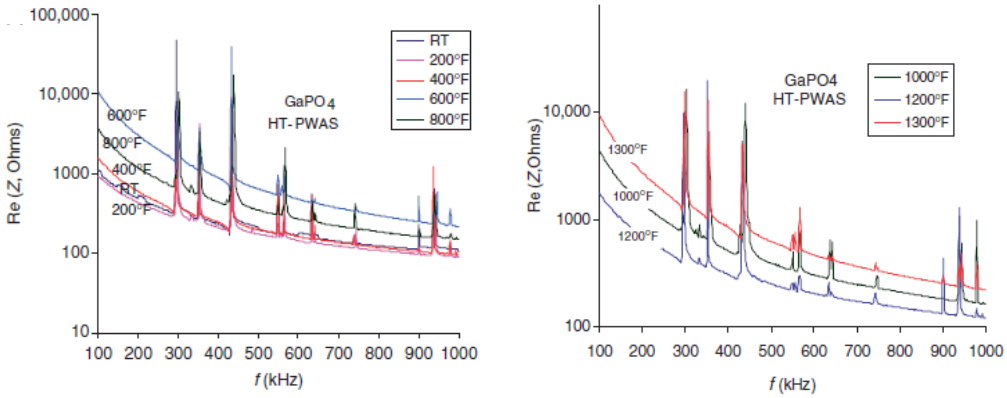

Figure 35: GaPO4 PWAS maintains its activity during high-temperature tests (measured at RT after exposure to the elevated temperatures, 1300 °F was the oven limit; the GaPO4 PWAS may remain active even above 1300 °F).

To evaluate the sensing capability at high temperature, bonded GaPO4 HT-PES was studied. The sensor was installed on a Ti disk. A nickel (Ni) wire was bonded with adhesive PryoDuct597A to the center of platinum (Pt) electrode on the top of GaPO4 HT-PES. The Ni wire was then affixed to the disk with Cotronics adhesive to ensure mechanical reliability. These tests were in-situ measurements. Temperatures were set from room temperature to the oven maximum temperature of 1300 °F with 200 °F increment. The real part of the E/M impedance spectra of the specimen instrumented with GaPO4 HT-PES were measured before and after high-temperature exposure in situ. Selected EMI results are shown in Figure 36. It can be seen that, after exposure to 1300 °F (705 °C) oven temperature, the HT-PES is still alive as indicated by the big peak in the impedance spectrum. However, the results are not as crisp as in the tests of free $GaPO_4$ HT-PES. The reason for this behavior may be due to the fact that instrumented specimen involving bonding adhesive and wiring is more complex than a free $GaPO_4$ HT-PES. The bonding between the $GaPO_4$ HT-PES and the structure and the electrically conductive bonding of the wires to the $GaPO_4$ HT-PES electrodes might have been affected by the high temperature exposure.

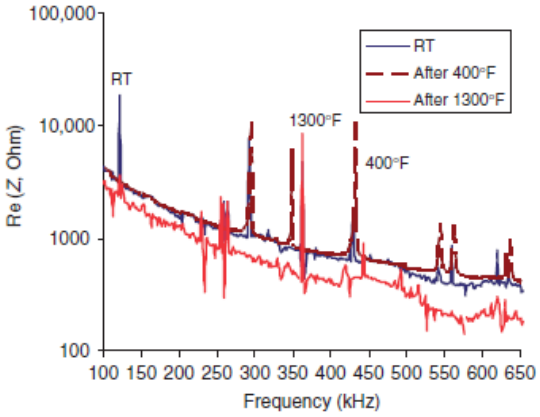

Figure 36: Real part E/M impedance spectra of HT-PWAS on Ti disk measured at RT, 400 °F, and 1300 °F.

The test procedure is similar to general PWAS temperature test. The test starts at room temperature, and ends with 225 °C. There are 40, 50, 75, 100, 110, 125, 135, 150, 175, 190, 200 °C, and total of 13 temperature points.

The real part of the admittance is shown in Figure 37a. To get close observation, zoom-in of first resonances is provided in Figure 37b with frequency range from 289 kHz to 294 kHz.

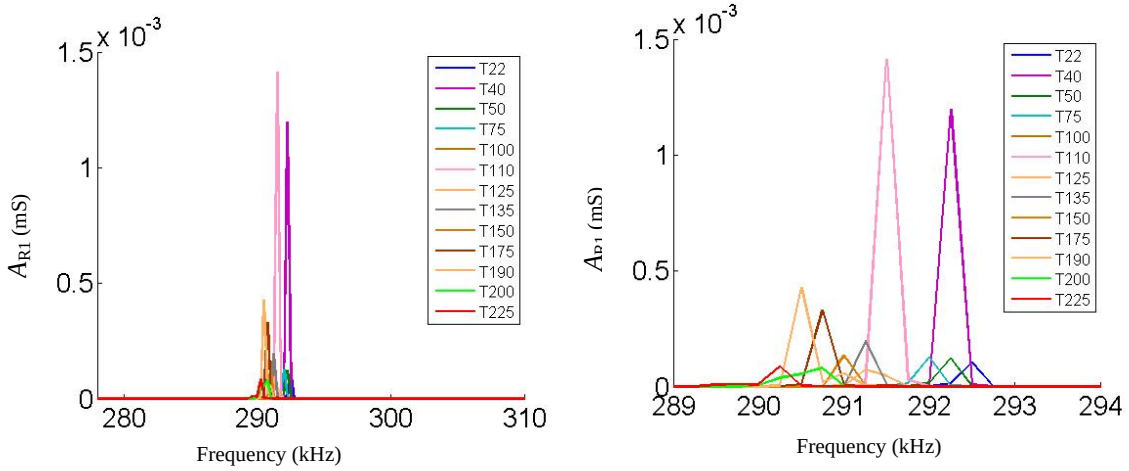

Figure 37 The admittance of the free GaPO4 sensor at different temperatures (a) from 270 kHz to 320 kHz; (b)Zoom-in of the admittance from 289 kHz to 294 kHz

The capacitance of GaPO4 PWAS was measured at each selected temperature point. The capacitances of $GaPO_4$ against temperature were plotted and presented in Figure 38.

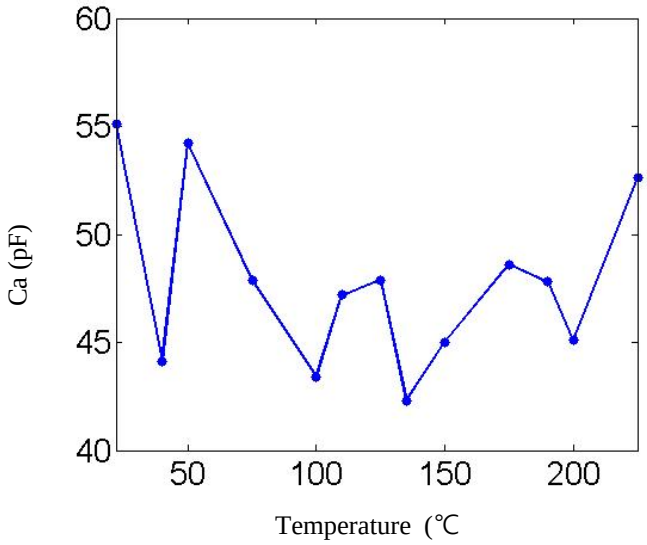

Figure 38 Capacitances at different temperatures

3 TECHNICAL ACCOMPLISHMENT 3: MULTI-MODAL SENSING DEVELOPMENT; VERIFICATION & VALIDATION TESTS

3.1 GOAL OF THE REPORTED WORK

The goal is to utilize the Micro II AE system to record AE signals and to locate the AE source based on the wave scattering theory at structural discontinuity and triangulation principles [45], [47]. The data acquisition and analysis functionality and algorithm are integrated in the AEwin software. The key components of AE source localization are sensor locations, AE wave velocity, and time of flight of the signals. At this stage, AE source is focused on the 2D planar plate.

The goal is to perform experimentally and numerically the temperature influence on the PWAS sensor and sensing capabilities and develop the damage detection algorithms with wave propagation approaches.

3.2 ACCOMPLISHMENT UNDER THIS GOAL

In this project, we investigated the AE source localization on a stainless steel plate using the commercial AE acquisition and analysis tools. We have successfully located the AE source simulated by pencil lead break (PLB) using 2D planar setup and estimated the source location errors. The detection results showed the pencil lead break can be detected within 10% error.

Software for simulating Lamb waves in thick structures was developed and validated. Temperature effects and compensation in software were simulated. Controlled temperature testing, material level investigation and modeling at material level were conducted to study the free PWAS responses to the temperature change. The bonded piezoelectric sensors with the purpose of damage detection have also been studied. Software tool for wave propagation study has been developed. We found temperature affects the guided waves excited in the structures and the damage detection as well. A temperature compensation algorithm has been therefore developed and validated to show that our array imaging method is able to address damage detection with environmental influence.

3.3 DISSEMINATION OF THE TASK

3.3.1 AE source localization

The AE source localization tests were conducted on a T304 stainless steel plate with dimension 420×330×1 (unit: mm). Four identical circular PWAS sensors (7 mm radius and 0.2 mm thickness) made of APC 850 material were bonded onto the plate using M-bond 200 for the AE tests. All the connections were the coaxial cables. The positions of the PWAS were at (105, 82.5), (105, 247.5), (315, 247.5) and (315, 82.5) which were labeled as P1, P2, P3, and P4, and the layout of the specimen is shown in Figure 39. The sensors are wired to 40dB preamp and then to the Micro II system to acquire the data, and AEwin software was used to analyze the acquired data for localization. Then the AEwin software analyzed the input data. In this test, Pencil lead break was conducted as AE source. The pencil lead was 0.5mm 2B. The setup is shown in Figure 40.

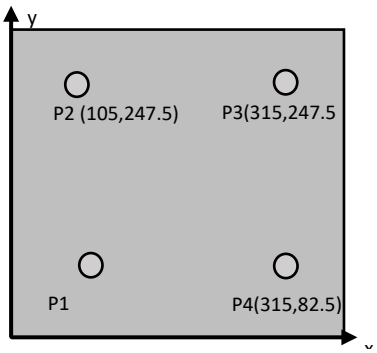

Figure 39: The layout of specimen

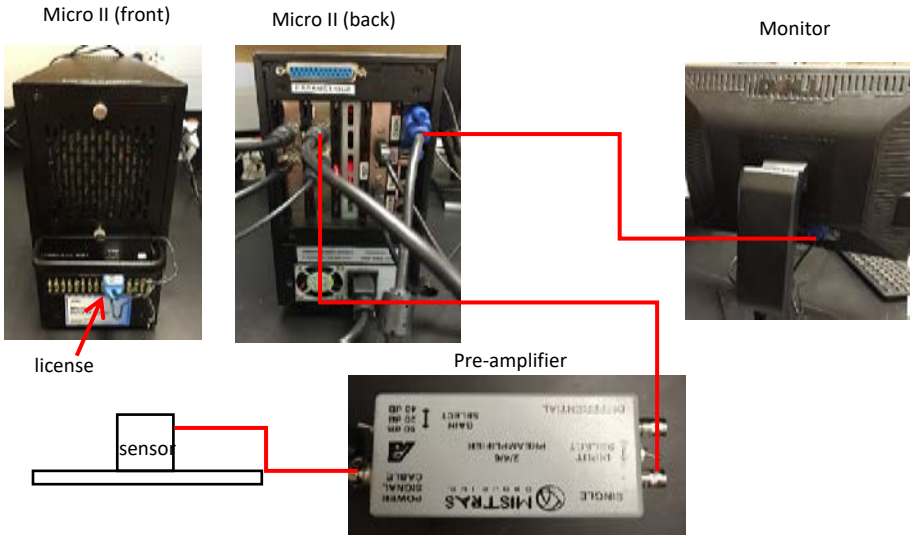

Figure 40: Experiment setup

Imaging of the AE source localization

For AE test setup, the key points are to choose the layout and the threshold level of the AE signal. In this test, because the specimen is a steel plate, the 2D Planar layout was chosen to be used. The thresh hold levels were decided as 55 dB for all four channels. The unit of the distance in this setup is millimeter. The estimated wave velocity was set as 5100 mm/μs in the 1 mm thickness steel plate. The pencil lead break test was conducted on the plate coordinate (300 mm, 150 mm). The experimental result is shown in Figure 41. The AEwin software estimated the source location is at the plate coordinate (290 mm, 141 mm). This is within 10% error comparing with the actual location (300 mm, 150 mm).

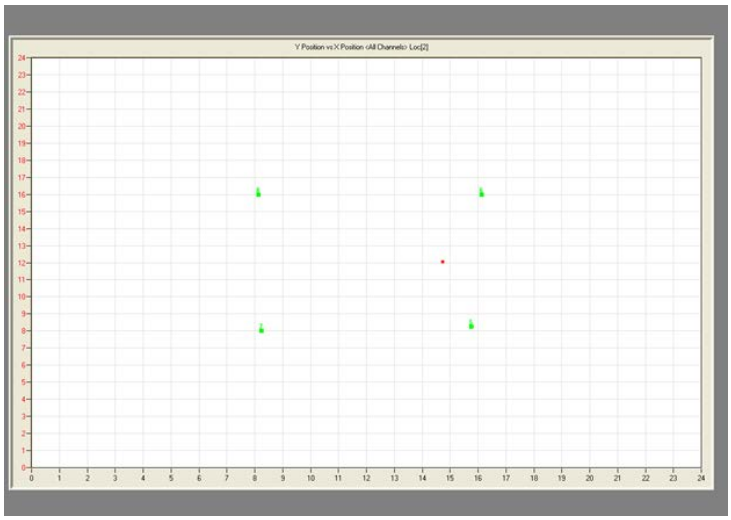

Figure 41: Imaging of AE source localization

3.3.2 Lamb waves simulation with temperature effects.

3.3.2.1 Software for simulating Lamb waves in thick plates

To simulate guided wave propagation and interaction, the elastodynamic finite integration technique (EFIT) is used. The EFIT is based on the finite integration technique (FIT) which integrates PDEs over a control volume and then approximates the integrals [52]. For guided wave simulations, the EFIT have following advantages: (1) the EFIT naturally requires staggered spatial and temporal grids which lead to stability, (2) the boundary conditions are easily incorporated in the EFIT model, and (3) the mathematical analysis is straight-forward and leads to equations that can be easily implemented in any programming language [53]. With these advantages, the EFIT method is used to simulate Lamb waves in thick plates.

In this subtask, 2D EFIT software is developed using Matlab programming language for simulating Lamb waves in the cross section of the isotropic plate. Figure 42 plots the front panel of the 2D EFIT software. This software has five modules, including Material Properties, Geometry, Excitation Signal, EFIT parameters and Output.

Figure 43 plots a flow chart of how to simulate Lamb waves by using the 2D EFIT software. Step 1 is defining material properties by giving the Young's modulus, density and Poisson's ratio in the Material Properties Module. Step 2 is defining geometry parameters of the plate and the PWAS actuator being simulated. In Step 2, the length and thickness of the plate, and the size and location of the PWAS should be given in the Geometry Module. In addition, the Geometry Module allows adding crack damage by defining the crack location, size and depth. Step 3 is defining the excitation signal by giving the excitation frequency and number of cycles. In the EFIT model, the PWAS excitation is simulated as pin forces with the unit amplitude at the edges of the PWAS. Step 4 is defining EFIT parameters. In this step, the gird size of the EFIT model, sampling frequency and simulation time should be given. Note that usually the gird size should be smaller than 1/10 of a wavelength. Step 5 is defining the output parameters. In this step, the

user can specify whether to output the velocity results or the stress results. Note that the output amplitudes are normalized. Once all the inputs have been given through Step 1 to Step 5, by clicking the Run button, the simulation will start.

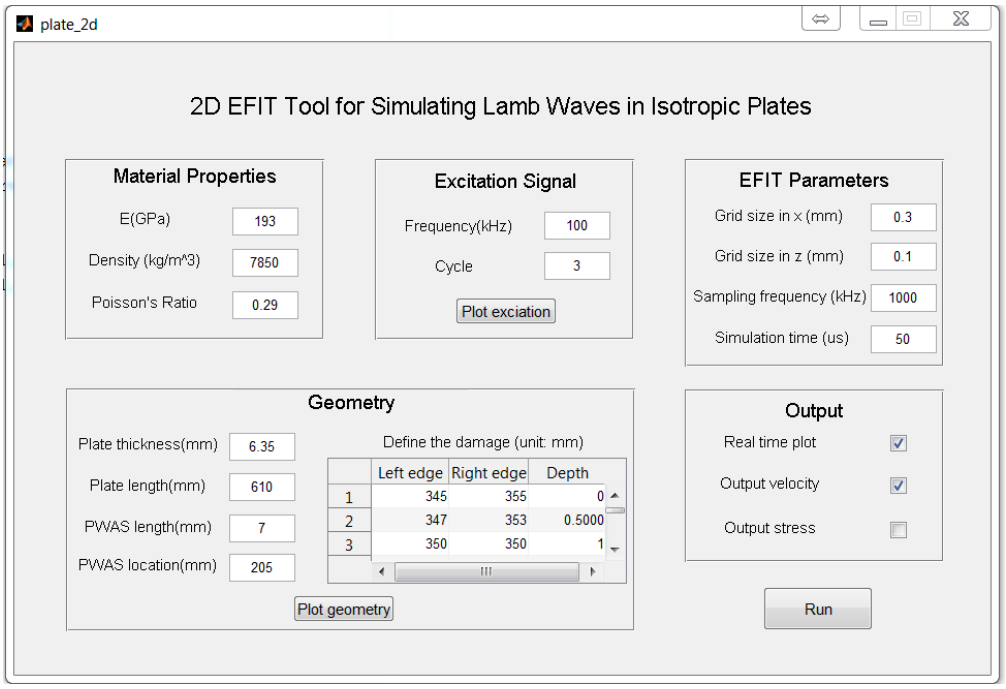

Figure 42 The front panel of the Lamb wave simulation software

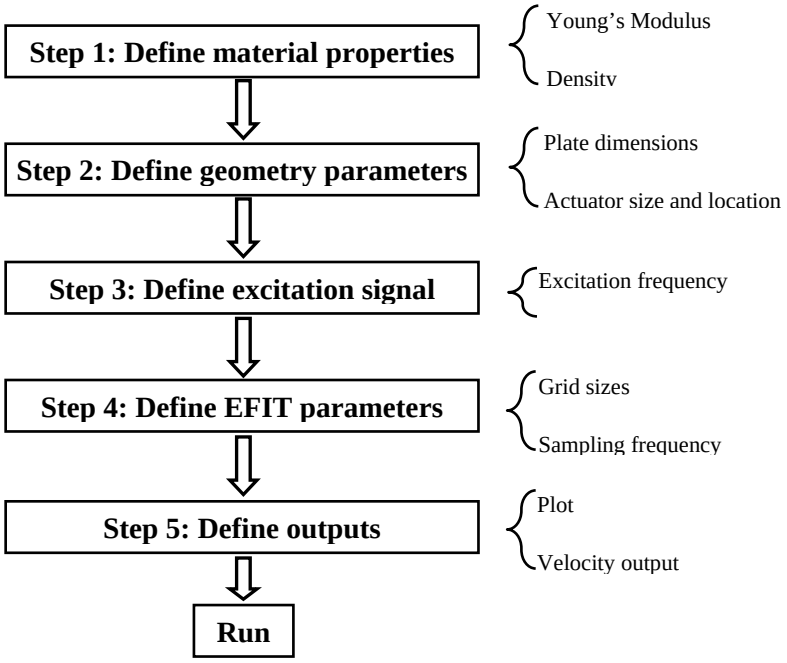

Figure 43 A flow chart of simulating Lamb waves using the 2D EFIT software.

3.3.2.2 Simulation of Lamb waves at different temperatures

After the 2D EFIT software has been validated, the software is used to simulate Lamb waves at higher temperatures up to 316℃. As presented in literatures, when the temperature increases, the Young's Modulus of T304 steel decreases (as plotted in Figure 44) with other material properties (such as density and Poisson's ratio) less affected. Thus, we assume that the density and Poisson's ratio remain the same at different temperatures in this simulation study. In addition, we assume that temperature only affects the Young's Modulus with the same relation in Table 4 and Figure 44.

The Lamb waves at six different temperatures (27, 149, 204, 260 and 316℃) are simulated by using the 2D EFIT software. The excitation is a signal of 3 count tone bursts at 100 kHz. Figure 45 plots the in-plane velocity wavefields at the same time 70 μs after the excitation at the six different temperatures. By comparing the six images in Figure 45, we can find that the locations of A_0 and S_0 modes gradually shift to the left side of the plate with the increase of temperature. The location shift is very small about 10 mm from 27℃ to 316℃. This location shift (i.e., smaller propagation distance) at the higher temperature could be caused by the smaller group velocity.

Table 4 Young's Modulus of T304 steel at different temperatures [ref]

Temperature (℃)	27	93	149	204	260	316
Young's Modulus E (GPa)	193	192	187	183	179	177

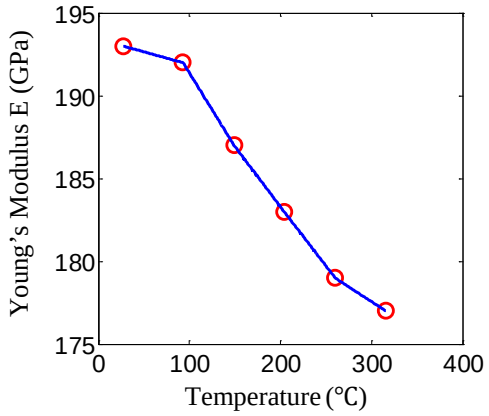

Figure 44 Temperature effect on Young's Modulus (plotted by using the values given in Table 4).

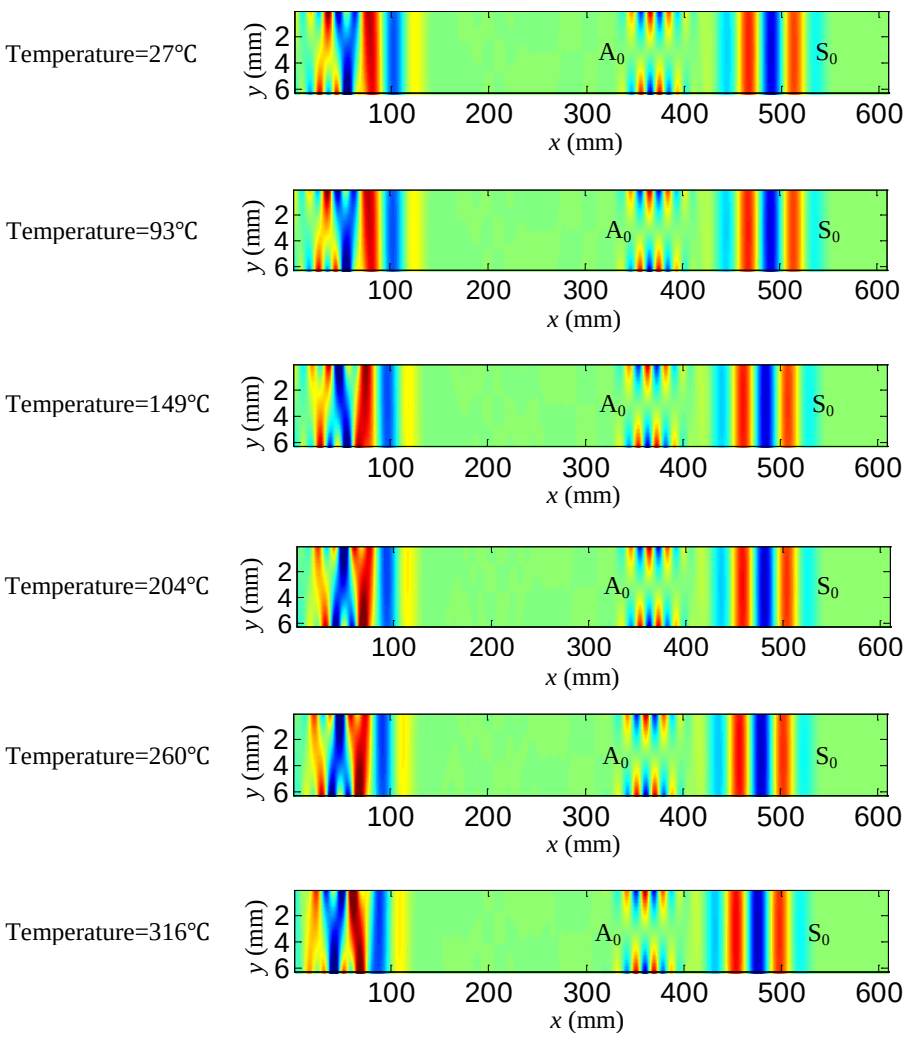

Figure 45 Simulation results (in-plane velocity wavefields) at 70 μs after the excitation at 27, 149, 204, 260 and 316℃ at 100 kHz.

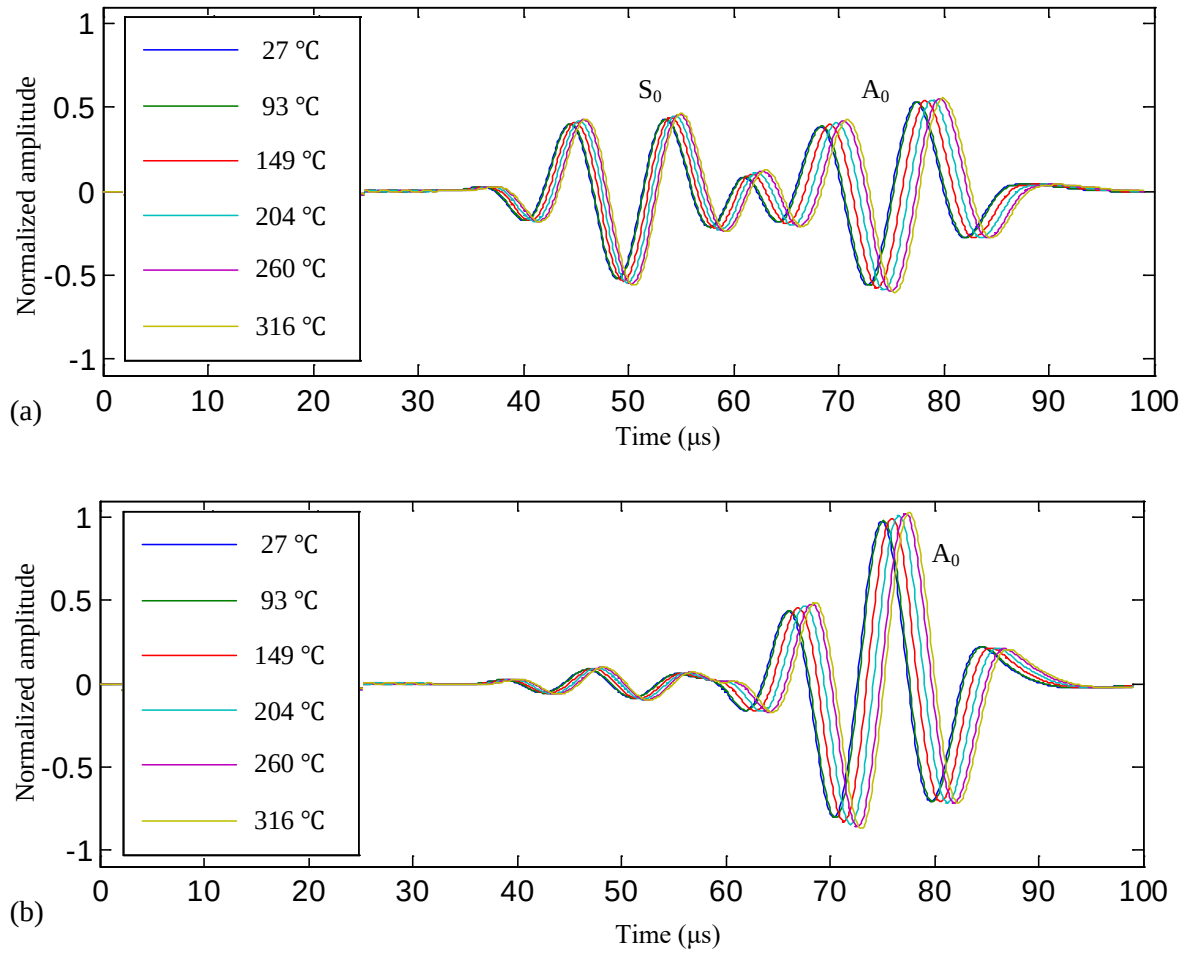

Figure 46 Simulation results (waveforms) received at 175 mm away from the PWAS actuator at different temperatures at 100 kHz: (a) in-plane wave motion; (b) out-of-plane wave motion.

Besides the comparison between wavefield images, Figure 46 compares waveforms received at 175mm away from the actuator at six different temperatures. All the waveforms are normalized with respect to the maximum amplitude of the out-of-plane waveform. By comparing the waveforms at the six temperatures, we can find that the travelling time of both A_0 and S_0 modes becomes larger (waveforms shift to the right side with the increase of temperature).

The travelling time of A_0 and S_0 modes is plotted in Figure 47a ("x" markers), which clearly shows that the travelling time of both modes increases with the increase of temperature. Using the travelling time and the propagation distance 175mm, group velocities at different temperatures are derived and plotted in Figure 47b ("x" markers), which shows that the group velocities of both modes decrease with the increase of temperature.

In addition to the simulation, theoretical group velocities of A_0 and S_0 modes are obtained by solving the classic Rayleigh-Lamb equation. The theoretical group velocities of both modes are plotted in Figure 47b (solid line). By comparing the simulation results ("x" markers) to

theoretical curves, we can find they agree well with each other in the temperature range 27~ 316℃, when the excitation is at 100 kHz.

Besides the case at 100 kHz, group velocities in the temperature range 27~ 316℃ and the frequency range 10~300 kHz have also been found through both simulations and theoretical derivations. Figure 48 plots the group velocities of A_0 and S_0 modes with respect to the frequency and temperature. As plotted in Figure 48a, the group velocity of A_0 mode increases with the increase of frequency, while it decreases with the increase of temperature. As plotted in Figure 48b, the group velocity of S_0 mode decreases with the increases of both frequency and temperature. In conclusion, with the increase of temperature, group velocities of both A_0 and S_0 modes gradually decrease.

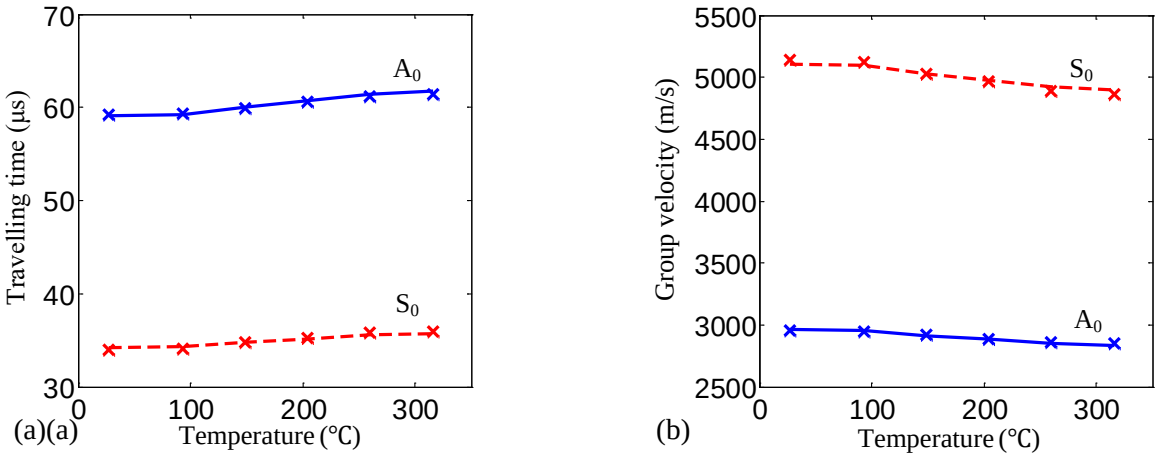

Figure 47 Wave travelling time (a) and group velocities (b) at 100 kHz at different temperatures. The "x" markers are simulations results. The solid curves are theoretical values.

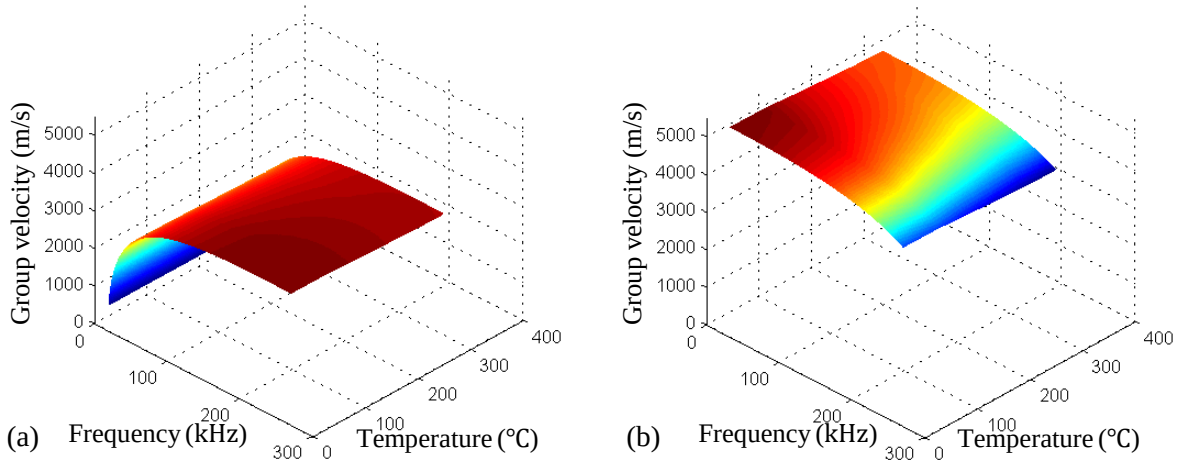

Figure 48 Group velocities versus temperature and frequency: (a) for the A_0 mode; (b) for the S_0 mode.

3.3.2.3 Temperature validation test in a pristine plate

Three-day test was conducted on the steel plate with dimension 420×330×1 (unit: mm). The schematic diagram of the specimen is shown in Figure 49. Four circular sensors with the same dimension (radius = 7 mm, thickness, h = 0.2 mm) were installed on the plate. One was used as transmitter labeled as T from the nearest boundary of 60 mm. PWAS 1 was collocated with the transmitter using pulse-echo tests. PWAS 2 and 3 were at a distance of 105 mm from the transmitter set on the center line. M bound 200 was used as the adhesive. PWAS 2 and 3 were for tracking changes in the guided wave transmitted signal with temperature (in undamaged state). On the first day (Day 1) and second day (Day 2) tests, frequency was set on 300 kHz for low frequency and 540 kHz for high frequency, separately. Temperature was set at room temperature, 40 ˚C and 50 ℃. On the third day (Day 3), the temperature was set from room temperature to 100 °C at 10 °C step size, and the frequency was set on 300 kHz, 540 kHz, 600 kHz and 750 kHz. After each day test, the system need to be cooled down to room temperature. At each temperature, pitch-catch and pulse-echo tests were processed at the same time with selected frequencies.

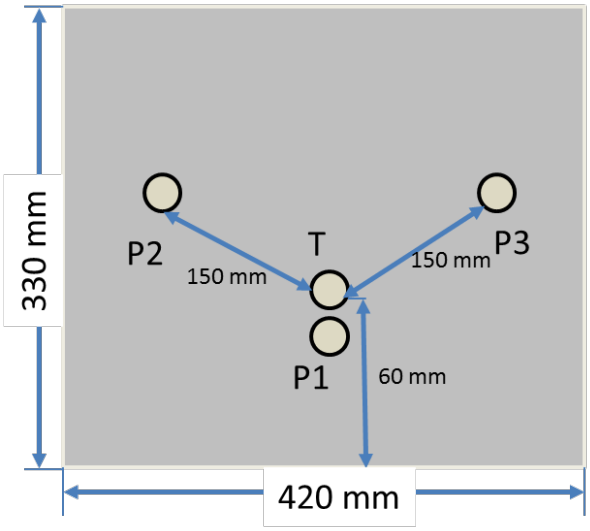

Figure 49: The schematic diagram of the pristine specimen

Pitch-catch tests results

Vertical shifting was added to make waterfall plotting. And the waveforms on Day 3 were plotted in Figure 50.

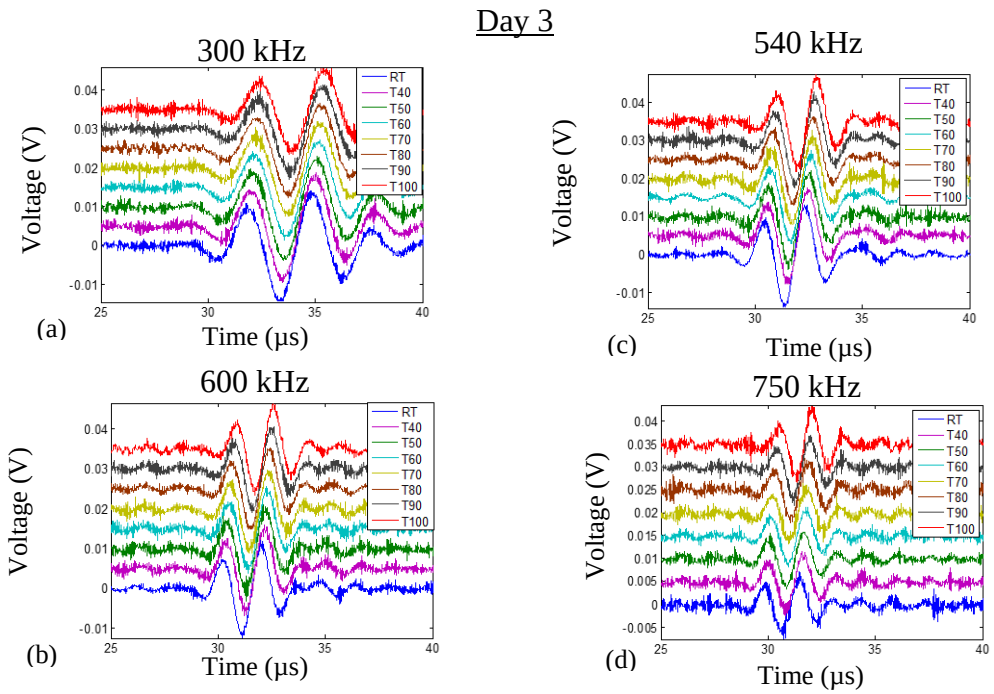

Figure 50: S0 mode on Day 3 pitch-catch tests: (a) wave forms at 300 kHz; (b) wave forms at 600 kHz; (c) wave forms at 540 kHz; (d) wave forms at 700 kHz.

3.3.3 Sensing methodologies: Imaging

We have developed a sparse array algorithm that processes data acquired from a group of sensors, called as sparse array, and generates an image of the plate to which the sensors are bonded for monitoring. The algorithm has been validated with simulated wave propagation. The location of the damage can be pinpointed exactly since we used the simulated data.

3.3.3.1 Principle of the sparse array algorithm

The image construction of the sparse array is based on a synthetic time reversal concept (Wang et al., 2004) by shifting back the scatter signals at time quantities defined by the transmitter-receiver locations used in the pitch-catch mode. Figure 51 illustrates the imaging approach. Assuming a single damage scatter is located at point $Z(x, y)$ in the structure, the scatter signal from transmitter T_i to receiver R_j contains a single wave packet caused by the damage (Figure 51b). The total time of traveling τ_Z is determined by the locations of the transmitter T_i at (x_i, y_i), the receiver R_j at (x_j, y_j), and $Z(x, y)$, as

$$\tau_z = \frac{\sqrt{(x_i - x)^2 + (y_j - y)^2} + \sqrt{(x - x_j)^2 + (y - y_j)^2}}{c_g}$$

where c_g is the group velocity of the traveling Lamb wave, assuming constant. Using the time-reversal concept in Wang et al., 2004, when a wave packet is shifted back by the quantity defined by the transducers and the exact position of the damage, i.e., τ_Z, ideally the peak will be shifted

right back to the time origin. If the wave packet is shifted by a quantity defined with otherwise cases (such as τ_i and τ_O), the peak will not be shifted right at the time origin (Figure 51b).

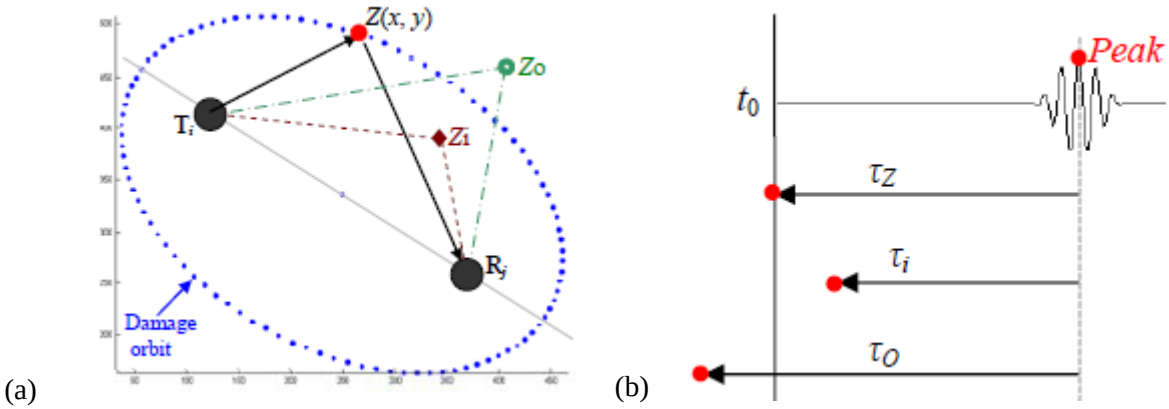

Figure 51: PWAS sparse array imaging principle: (a) damage orbit; (b) signal shifting

For an unknown damage, for certain scatter signal with τ_Z, the possible locations of the damage is an orbit of ellipse with the transmitter and receiver as the foci (Figure 51a). To locate the damage, ellipses from other scatters (or transmitter-receiver pairs in the network) are needed. For a given network of M transducers, a total of M^2 scatter signals will be used if reciprocity is not considered. In our study, two algorithms, one based on summation process and the other based on the correlation process, have been explored for the imaging. Using the summation processing (Michaels and Michaels 2007), the pixel value at an arbitrary location $Z(x, y)$ in the scanned plane is defined as

$$P_z(t_0) = \prod_{i=1}^{M} \prod_{j=1}^{M} s_{ij}(\tau_Z), i \neq j$$

where s_{ij} is the scatter signal obtained from the j^{th} receiver when the i^{th} transmitter sends. Using the multiplication processing (Ihn and Chang 2008), the pixel value is defined as

$$P_z(t_0) = \sum_{i=1}^{M} \sum_{j=1}^{M} s_{ij}(\tau_Z), i \neq j$$

3.3.3.2 Imaging Using Adjusted Baseline and Measurement

The temperature change embedded in the scattered signal causes the failure of sparse array imaging in the previous case and hence needs to be removed. The solution developed in this study is to adjust the baseline to accommodate the temperature change that occurs at the time of measurement. Given the knowledge of temperature effects on guided waves learned in Section 3, the baseline at room temperature is then shifted to account for the elevation to 40 ˚C. The scatter signals are now obtained by subtracting the adjusted baseline from the measurement at T 40 ˚C.

The imaging result of the adjusted data is shown in Figure 52, indicating the presence of the hole at (208, 122) with ~1% error compared to the actual location.

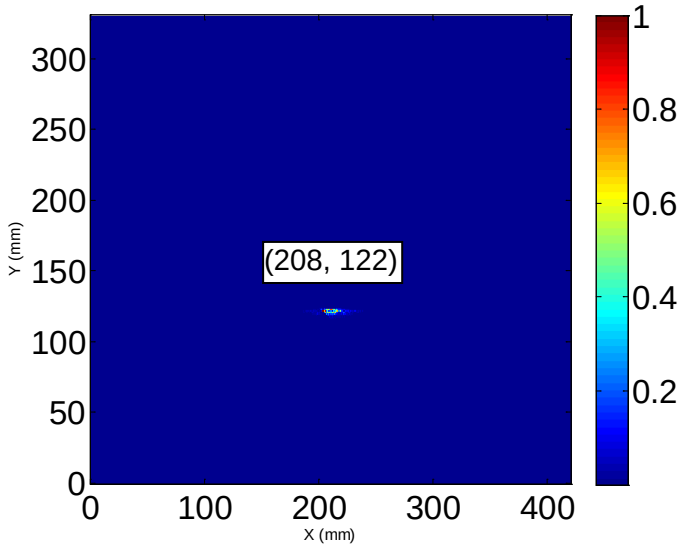

Figure 52: Image of the plate using adjusted baseline and T 40 ˚C measurements

4 TECHNICAL ACCOMPLISHMENT 4: SCALE-UP STUDY AND PREPARE FOR IN-SERVICE APPLICATIONS

4.1 GOAL OF THE REPORTED WORK

The goal is to test and valid the AE functionality of a middle-scale structure. Dry cask storage canisters are large complex structures with a lot of structural features and irregularity. To insure implementation of structural health monitoring on them, testing on structures with complexity is necessary. Two scale-up experiments were performed to explore the sensing capabilities of acoustic emission (AE) on a medium size and a small size facilities with complexity therefore.

4.2 ACCOMPLISHMENT UNDER THIS GOAL

We performed two mockup experiments during the project period. The first one was AE testing on a vacuum chamber at USC. The second experiment was testing on a mockup canister at University of Mississippi (OLEMISS). Resonant and wideband passive piezoelectric AE sensors were used in detecting responses created from many difference sources. These sources include: simulated AE events with PLB, impact balls, and impact hammer hits. After testing many different locations, the results were analyzed. It was found that PLBs had consistent excitation in amplitude and in frequency. It also produced the highest frequency response compared the other simulated AE events. The impact balls and impact hammer produced repeatable frequency responses; however their amplitudes would vary due to the human error involved. The impact hammer produced the lowest frequency response of the three simulated AE methods. Specific location data created by the simulated AE event experiments along with the AEwin software was

used to calculate the impact locations of the simulated AE events. Accurate calculated results were found where nearly all hits fell within a few inches of the excitation source.

4.3 DISSEMINATION OF THE RESULTS

4.3.1 Medium scale testing

The experiment is planned to perform on a vacuum chamber. The vacuum chamber is divided into sections (Figure 53) where areas of sensing and excitation could be identified. External flanges are counted starting with the bottom left flange (F1) and would alternate sides counting up. The front surface areas between the flanges are denoted with “S” and were followed by a number increasing from the lower most surface S1. The back flanges are denoted with “FB” and are counted in the same manner as the surfaces. Lugs are counted from the bottom up in a clockwise fashion starting with the left rear lug. The lugs are denoted with “L” followed by its placement number.

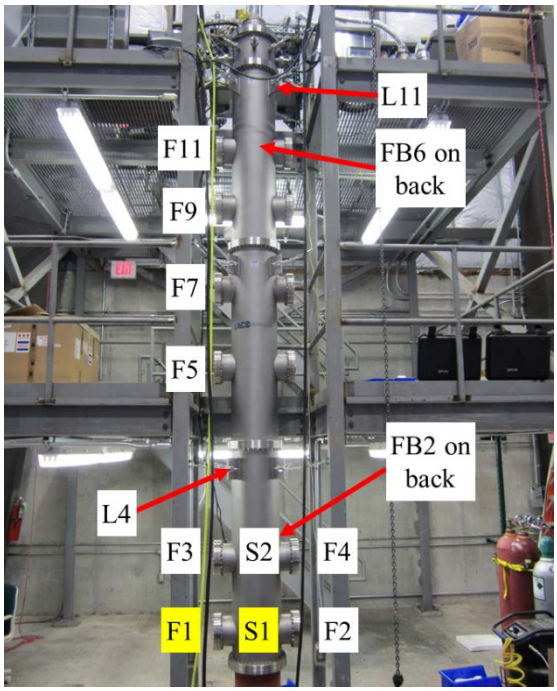

Figure 53 Structure and various locations used. Locations with sensors are highlighted yellow

Experiment round 1

Three experiments were completed to evaluate the SHM system. The first of which examined the sensing capabilities with various excitation methods on the complex structure to identify what type(s) of excitation can be detected. To do so six AE sensors in two sets of three were applied using hot glue to the surface of the vacuum chamber. Each set contained a R15I, a R15α, and a WSα. One set was mounted to the lower left flange, F1 and the other to the front face, S1.

A PCB model 086C04 impact hammer with a built in accelerometer and a PLB, with .07mm lead will be used to excite the AE signal. Two hammer tips will be used for testing: a plastic PCB tip and a custom made 304 stainless steel tip (Figure 55).

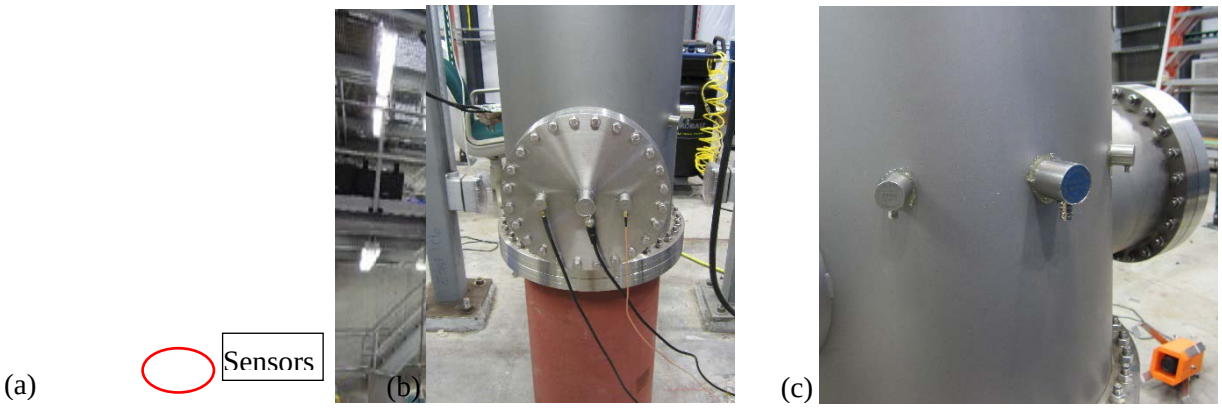

Figure 54 Sensor placement and sensors on surface. (a) Entire structure, (b) sensors applied on the F1 flange, and (c) sensors applied to the S1 front face.

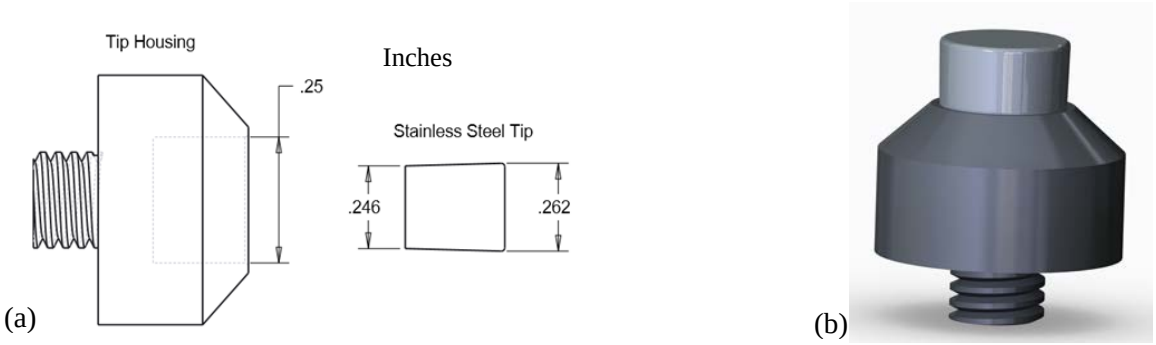

Figure 55 Stainless steel hammer tip. The PCB tip housing (a) is made of aluminum and (b) assembled tip

Various impact locations were chosen for both sets of sensors. For each set of sensor location, a PLB, stainless steel tip impact hammer, or a plastic tip impact hammer excitation used, as shown in Table 5. For each test, the surface was impacted three times. Three additional tests were carried out for each point for a combined nine hits per checked location.

Table 5 Sensors, excitation type and impact locations

		Excitation Location											
Sensing Location	Excitation	F2	F3	F4	F5	F7	F9	F11	FB2	FB6	L4	L11	S2
F1	PLB	✓	✓	✓					✓		✓		✓
	Stainless steel tip	✓	✓	✓	✓		✓	✓	✓	✓	✓	✓	✓
	Plastic tip	✓	✓	✓					✓		✓		✓
S1	PLB		✓						✓		✓		✓
	Stainless steel tip		✓		✓	✓		✓	✓	✓	✓	✓	✓
	Plastic tip		✓						✓		✓		✓

The hammer hits were monitored to have similar decibel amplitudes. The AEwin software received the signals from each sensor which was exported to MATLAB for later analysis. Within the software four channels were used for the impact hammer tests. Channel one was used for the impact hammer, channel two for the R15I sensors, channel three for R15α, and channel 4 for WSα. Their thresholds and other sampling settings are shown in Table 6. The R15I sensor has a built in 40 dB preamplifier while the R15α and WSα each has an external 40 dB amplifier. The external amplifiers used are Mistras Model 2/4/6 which have band filters of 30-700 kHz. During the PLB tests the channel 1 for impact hammer was removed from selection.

Table 6: Software setup for channels for round 1

AE Channel	Threshold			Gain	Pre-Amp	Analog Filter		Waveform Setup		
	Type	dB	FTBnd	dB	dB	Lower	Upper	Sample Rate	Pre-Trigger	Length
☑ 1	FIXED	80	6	0	0	1kHz	3MHz	1MSPS	256.0000	2k
☑ 2	FIXED	60	6	0	40	1kHz	3MHz	1MSPS	256.0000	2k
☑ 3	FIXED	60	6	0	40	1kHz	3MHz	1MSPS	256.0000	2k
☑ 4	FIXED	60	6	0	40	1kHz	3MHz	1MSPS	256.0000	2k

Experiment round 2

During round 1, we found the R15i transducers provided weaker signals and therefore, they were not used in continuing rounds. One sensor was bonded onto the surface of the bottom flange F1 and the other was in the center of the lower-most surface S1. After test was completed for sensors WSα, they were removed and replaced with R15α sensors. Only PLB tests were performed and detected at locations shown below:

		Excitation Location													
Sensing Location	Excitation	F2	F3	F4	F5	F7	F9	F11	FB2	FB6	L4	L11	L12	S2	SB2	SB4
F1	PLB		✓			✓					✓		✓	✓	✓	✓
S1	PLB		✓			✓					✓		✓	✓	✓	✓

The location L11 was found being difficult to reach for the PLB during the first round. Therefor the farthest sample point was relocated from L11 to L12 later. To capture the simulated AE events only two channels were used: Channel 1 was connected to the sensor on S1 while Channel

2 was attached to the senor on F3. The settings from Round 1 were reused except the number of samples (length), which was increased to 3000.

Results: sensing capability of long distance through structural complexity

The AE events were created by the PLB, the striking of a hammer with the original plastic tip and the stainless steel tip. The farthest sensing path was between the excitation at L11 and sensor at F1 for the stainless steel tipped striking and L12 to F1 with the PLB. All three types of AE transducers (R15i, R15α, and WSα) were used. The testing showed that the plastic tip striking at L11 could not be detected at F1. In Round 1 the AE produced by the stainless tip striking could be detected by all three transducers. FFTs were performed to reveal the frequency components. These results are shown in **Error! Reference source not found.**.

R15i was found to be the most difficult to trigger and produced the weakest signals, which were indistinguishable from the background noise. The WSα did not perform significantly better but captured many resonance peaks. The sensing capabilities of the PLB from L12 to F1 were explored in Round 2 (Figure 56). The signal produced from the PLB's amplitude was significantly higher and the FFT plots exhibited a much better-defined resonance. The R15α showed a single significant resonance at 150 kHz and the WSα a single resonance peak just shy of 100 kHz.

We also explored the sensing capabilities of the AE events produced by stainless steel hammer and by PLB. At the farthest point tested with the hammer (at L11) we saw a low amplitude across all the sensors where R15i demonstrated a poor, noise-like signal. The R15α produced the best signal which had a single amplitude peak but peaked at 48 kHz. When examining the Round 2 results in Figure 56, the signals from PLB appeared better than those from the stainless tip striking. A resonance peak of 150 kHz was observed with R15α. Interestingly, the wideband sensor WSα produced only a single reasonace peak.

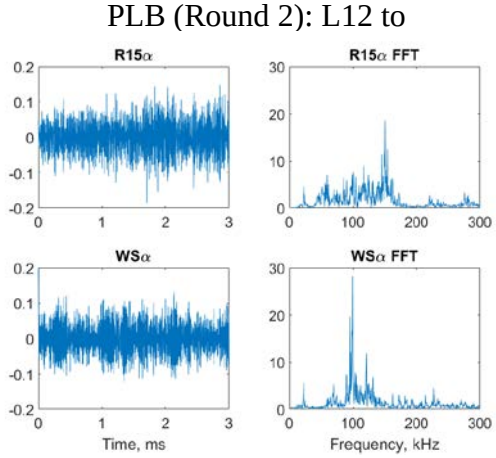

Figure 56 Round 2 signals from the farthest point excited by PLBs (L12 to F1)

Results: study of sensing through local complexity

Further exploration was made into some of the specific features of the vacuum chamber. Excitation locations were selected with the following cases:

- Surface to surface (S2 to S1)
- Surface to Flange (S2 to F1)
- Flange to Surface (F3 to S1)
- Flange to Flange (F3 to F1)

The AE events were first produced by stainless steel tip striking (Figure 57) and then by PLB (Figure 58). The changes in the time and frequency domains were examined by observing the signals passing through the flanges and traveling along the structural surfaces.

As shown in Figure 57, the simulated AE events were produced with the stainless steel tip hammer striking. All the plots exhibit lower frequency resonance below 100 kHz, however, the individual peaks are shifted. The surface to surface case (S2 to S1) produced a gradually increasing and decreasing FFT slope for both the wideband sensor (WSα) and the resonance type sensor (R15α). It was interesting to note from the signal collected when passing through a flange or multiply flanges, well-defined FFT resonance peaks were produced. The R15α sensors in the cases involving flanges resulted in multiple peaks whereas the WSα frequently produced only a single significant peak of resonance. From observation, it appears that the flange behaves as a filter which damps out various frequency components or an oscillator that carries its own natural vibrations.

When the PLB was used (Figure 58) higher frequencies were detected in the structure. Large peaks up to 500 kHz were produced by the R15α and a wider range with the WSα. The surface to surface condition exhibited less but larger peaks than the condition involving the flanges.

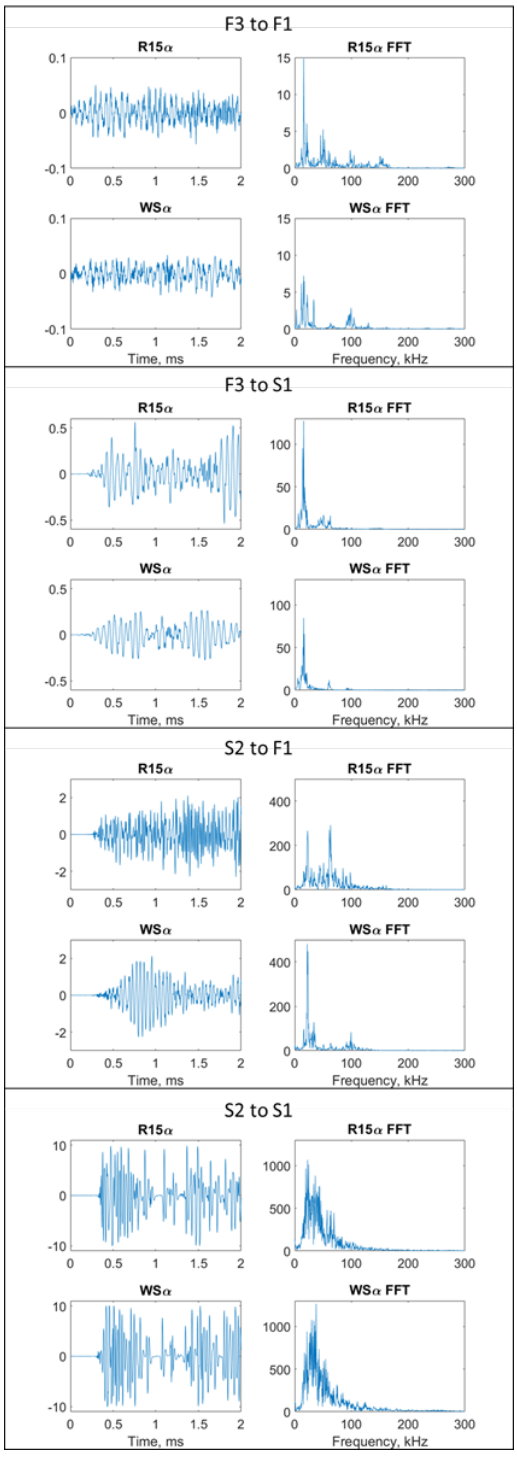

Figure 57 Waveform and FFT from stainless steel tip striking with various flange and surface conditions

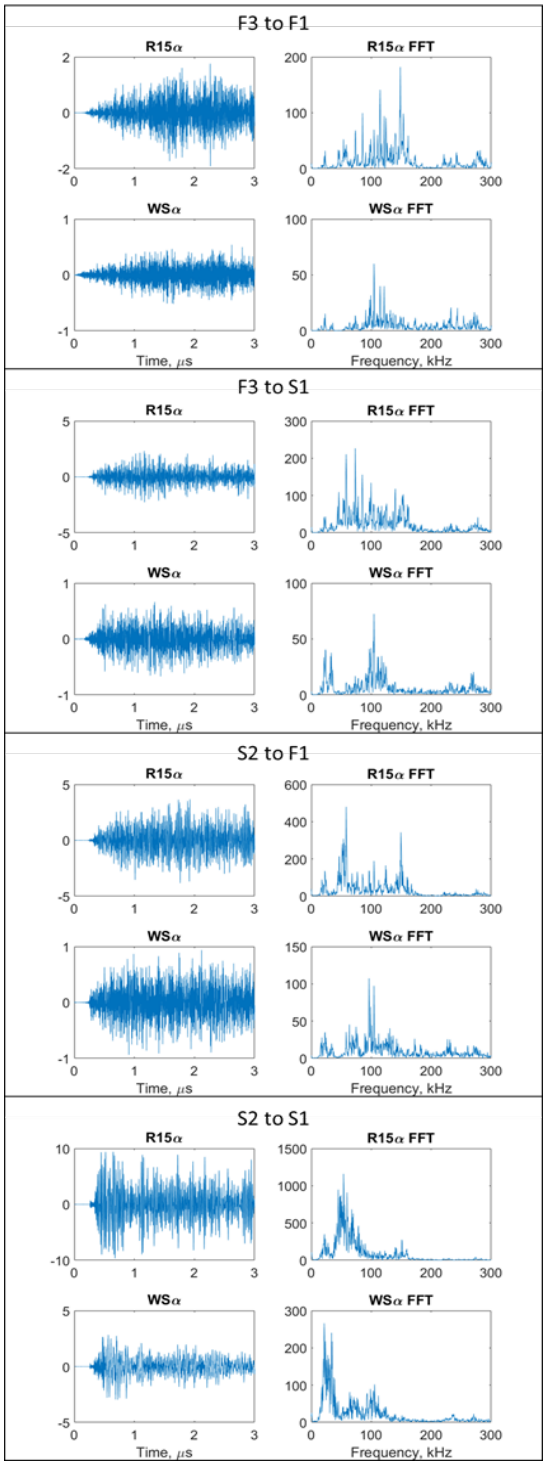

Figure 58 Wavefrom and FFT from PLB with various flange and surface conditions

Result: background noise

One of the key in AE detection is to set up the appropriate threshold, that shall be not too high to miss AE event while also important, not too low to be randomly triggered by background noise. So a good sensing shall start from studying the background noise from the operating environment to help set up the threshold. For this purpose, we used the WSα and R15α sensors to receive signals at the lowest threshold possible of 40 dB (due to 40 dB preamplifiers) to detect noise from the movement within the laboratory. During experimentation the maximum peak amplitude noise was recorded by both sensors. The R15α sensor was more sensitive to the noise with a maximum amplitude of 61 dB while WSα reached a maximum of 54 dB (Figure 59).

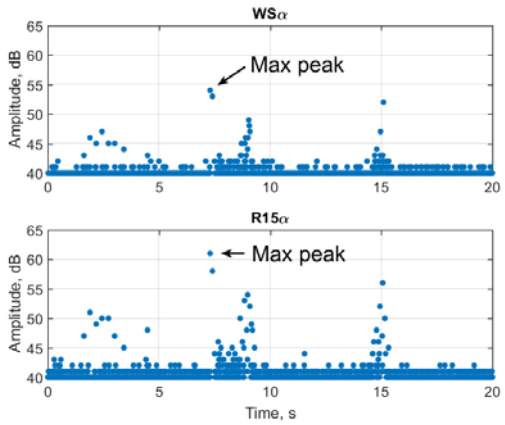

Figure 59: Background noise in the laboratory with movement around the structure where the sensors were installed

We also tried shuffling around the vacuum chamber and found it resulted in multiple peaks. These peaks in amplitude as well as the base noise, that seemed to be uniform along the threshold, were investigated (Figure 60). Signals collected along the threshold line held consistent FFTs. The WSα sensors produced a flat FFT while the R15α sensor signals produced a resonance peak around 150 kHz. The maximum peaks showed a resonance peak for the WSα around 26 kHz with smaller peaks spaced between 50 kHz and 100 kHz. The R15α had a maximum peak at 46 kHz with a second lesser peak around 150 kHz.

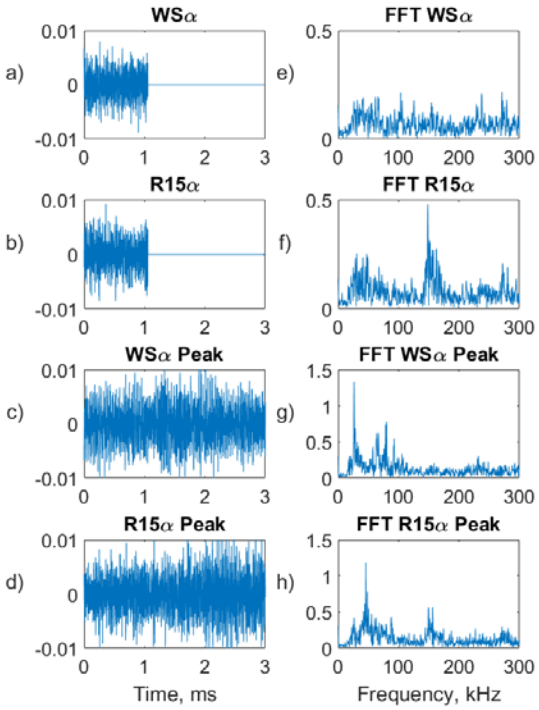

Figure 60: The signals of the uniform base noise (a and b) with their resulting FFTs (e and f) along with the maximum peaks' signals from the noise (c and d) with their corresponding FFTs (g and h)

4.3.2 Testing on a canister mockup

We were able to be supported to perform the sensing on a small-scale canister mockup provided by University of Mississippi. The mockup canister is unloaded but provides very complex geometry for us to evaluate the proposed sensing methods.

Excitation methods

Beginning experimentation, frequencies that excited various components within the small-scale mockup cask were unknown. Therefore, a variety of methods were used to excite a range of frequency responses, including:

- Impact Hammer: A PCB Model 086C04 impact hammer was used for excitation for AE tests (Figure 61a). The hammer was fitted with a custom made T304 stainless steel tip (Figure 61b). This tip was used for all impact hammer excitations described in this report.

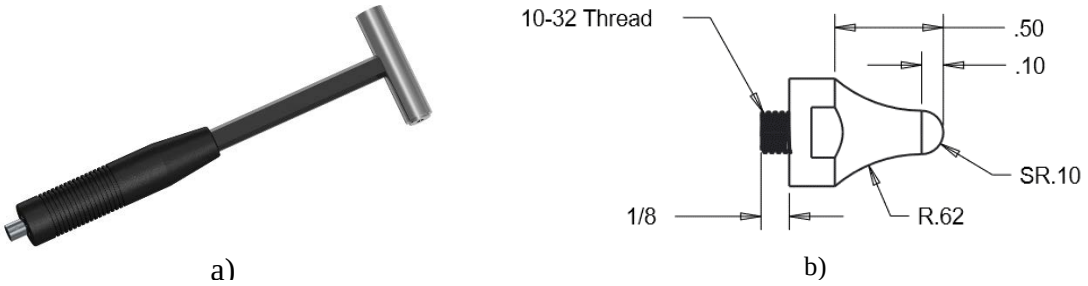

Figure 61: a) hammer used in excitation and b) tip fitted on hammer

- PLB: A standard PLB break test was conducted using 0.5 mm HB lead. PLBs were used to excite relatively higher frequencies within the structure.
- Carbon steel ball: To excite a somewhat midrange response between the PLB and impact hammer, carbon steel balls of various sizes (0.25, 0.137, and 0.125 inch diameter) were lightly thrown at the surface of the cast. All excitations using this method were thrown at SG5 (described in sensor locations).

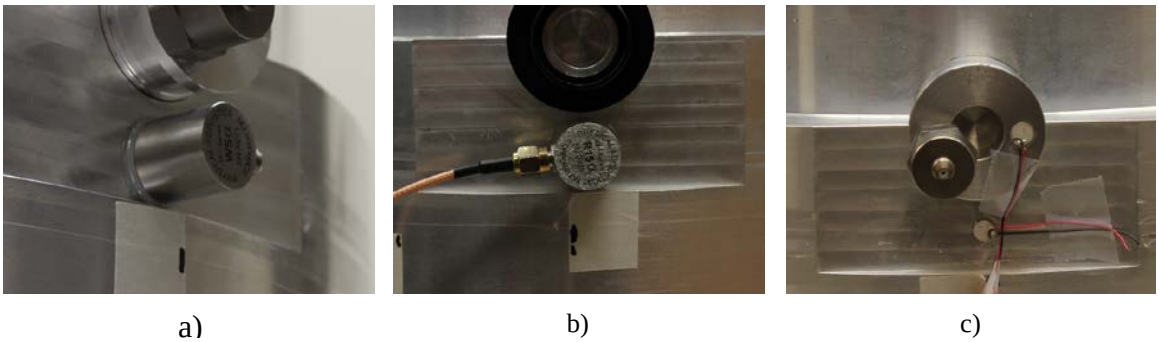

Figure 62: Sensors used experiments: a) WSα, b) R15α, and c) PZT wafers

- Sensors: For the experiments AE sensors were used: WSα, R15α and they were installed nearby the areas on the bottom of the canister as illustrated. Before testing, locations were defined on the surfaces, small geometry, rims and certain basket guides. These locations used either for excitation or sensor placement. Three settings are considered in this research for sensing capability study (T series), localization ability (SG series), and complex concern (R series).
    - T series: The T series represent the trunnions. The trunnions were labeled T1 to T4 starting from top left to right and then bottom left to right, increasing in number.
    - SG series: SG or surface gird locations were defined for localization techniques like that on the full-scale testing. The grid was 3 by 3 points where the vertical center was on the vertical plane between T1 and T2. The horizontal center laid 11 inches below the outside rim (directly above the top trunnions). The points were labeled left to right from the top down starting at SG1 ending with SG9 (Figure 63).

- R series: R represents the testing of the inside rim when the lid was not present. They were labeled at each 90 degrees, clockwise pattern, starting with R1 and ending with R3 (where the back wall was ignored, assuming symmetry). The points were at the midpoint of the top lip and the basket guides.

Figure 63: The surface grid (SG) series on the front face of the cask

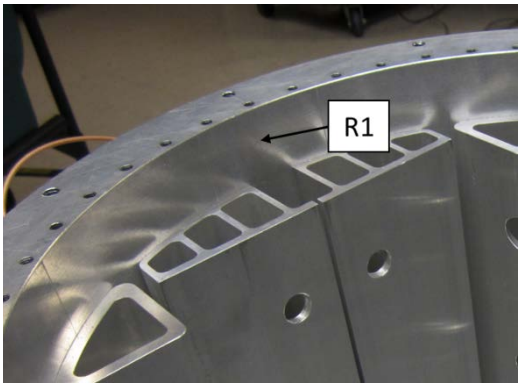

Figure 64: Location of R1

AE experiments

Each experiment the sensors were in sets of four placed on the trunnion faces. All AE experiments with WSα and R15α used a Physical Acoustics MICRO II Digital AE system (Figure 65a) along with its supporting AEwin software to record the hits. Sensor and excitation locations for all the AE experiments were recorded. Sensors were used in pairs where all were supplied with 2/4/6 Physical Acoustics preamplifiers (Figure 65b) which have a built in 30-700 kHz bandpass filter.

Test runs were completed and settings were tuned to find appropriate settings for the AEwin acquisition. Those settings were recorded (Table 7). Note the analog filter would be superseded by the 2/4/6 Preamplifier's 30 kHz – 700 kHz bandpass filter. For the simulated impact hammer AE to basket experiments a Tektronix TDS5034B oscilloscope was used to receive the signals. The accelerometer from the impact hammer was used as the trigger.

a) b)

Figure 65: Pictures of an a) 2/4/6 preamplifier and the b) AE computer

Table 7: Settings for AEwin acquisition

Sensor type	Threshold	Pre-Amp	Analog filter	Sample rate	Pre-trigger	Length
R15α	50	40	1 kHz to 3 MHz	1 MSPS	256	5000
WSα	60	40	1 kHz to 3 MHZ	1 MSPS	256	5000

Wave speeds and event definitions for localization study

To calculate the simulated AE locations, various settings are needed (Table 8). All the settings were estimated by tuning after each replay. Once optimal settings were found the settings and impact locations were saved.

Of these settings, the biggest influence of calculated AE localization was the estimated wave speed. All sets of data had the same wave speed and event definitions except for one point where the event definition was changed. The event definition had relatively insignificant influence on the calculated impact location.

Table 8: Settings for localizations

Sensor	Basket	Excitation	Wave speed, in/sec	Event definition	Exemptions
R15α	In	PLB	140000	20	
WSα	In	PLB	100000	20	
R15α	In	Impact hammer	110000	20	Event def 5 on SG7
WSα	In	Impact hammer	100000	20	
R15α	Out	PLB	140000	80	
WSα	Out	PLB	110000	15	
R15α	Out	Impact hammer	100000	80	
WSα	Out	Impact hammer	140000	15	

Simulated AE excitation response

To better understand more detailed analysis, the basic structural responses of the small-scale mockup need to be understood. We need to explore the passing waves as they circled around the surface of the structure. During experimentation, multiple wave passes were observed. This was more prevalent during respectively higher frequency excitations such with PLB. The details from the passing wave experiments helped determine some localization settings.

Based on the small-scale mockup cask structure and type of excitation used, different frequency responses were expected. To better understand what response was coupled with the excitation and sensor used, frequency plots were made from several experiments. First examined was the ball excitation. For simplicity, only the path of SG5 to sensors on TF1 are shown.

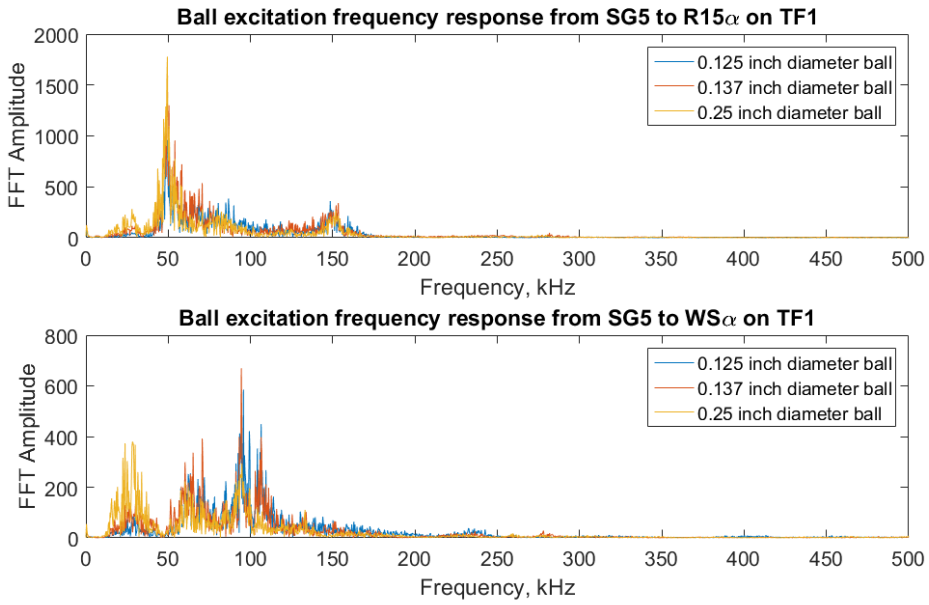

Figure 66: Ball excitation response with R15α and WSα on TF1 while basket was out

All the impacting balls used, of different diameters, had very similar frequency response. The R15α resonant type sensor produced a large resonance peak at 50 kHz and a small peak at the sensor's resonance peak at 150 kHz. As expected the WSα wide band sensor produced more peaks but surprisingly produced no peaks after roughly 120 kHz. The PLB tests were performed next. Three peaks can be seen from the R15α signal where the largest fell at 150 kHz. The WSα produced a much wider range of frequency components with many different peaks. Last, the impact hammer frequency response was examined.

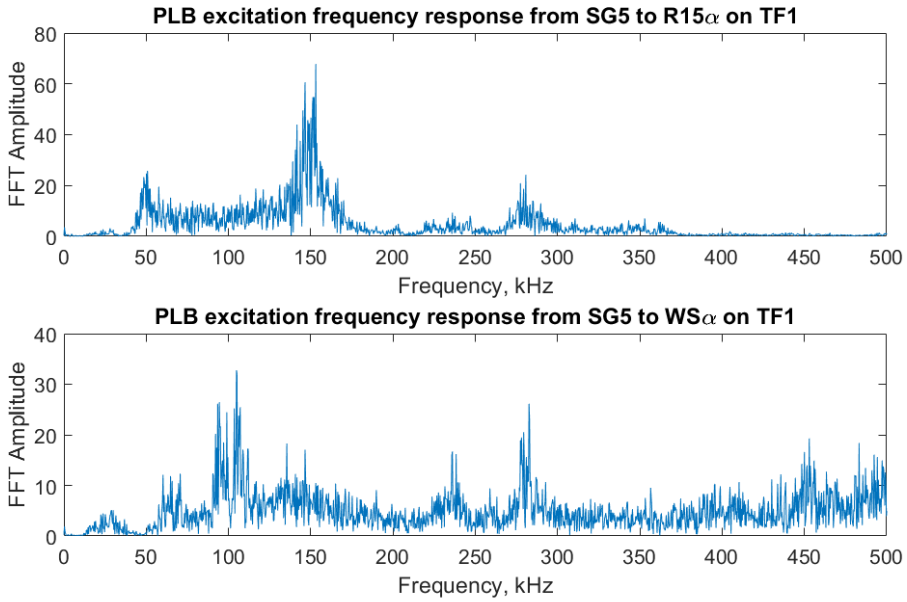

Figure 67: PLB excitation response with R15α and WSα on TF1 while basket was out

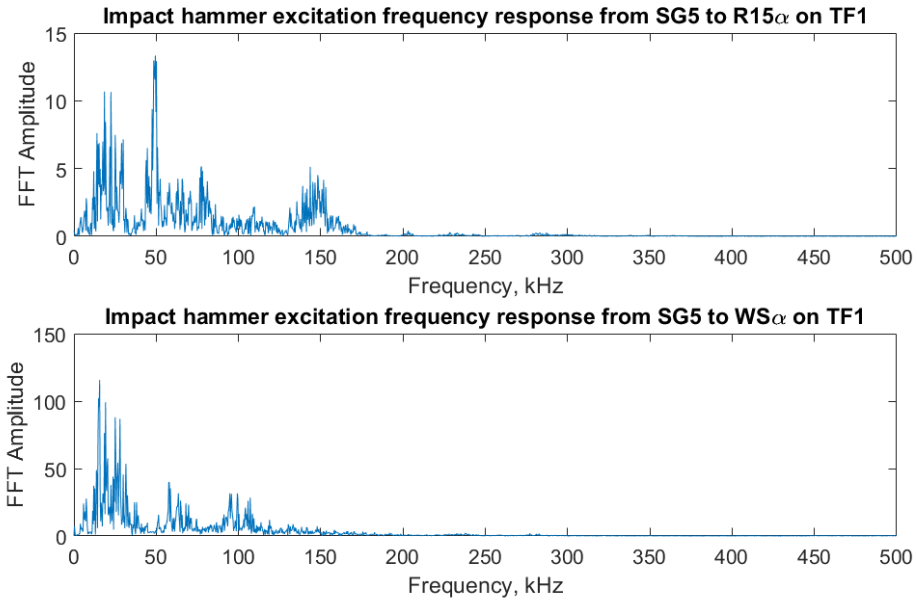

Figure 68: Impact hammer excitation response with R15α and WSα on TF1 while basket was out

The impact hammer produced significantly lower frequency components that the other methods. Peaks for both AE sensors fell under 200 kHz with no higher harmonics. To see the consistency between consecutive hits a sample from the TF1 position under the fuel rod basket out condition was examined. This data consisted of two sensor types: R15α and WSα. Both the waveforms and their frequency response from PLB excitation was plotted (Figure 69).

The PLB excitations had very similar excitation between hits. The amplitudes were nearly consistent as well as their corresponding FFTs. Differences between the sensors types was clear as a significant peak around 150 kHz can be seen on the R15α FFT while the WSα demonstrated its wideband capabilities. The consistency between hits using the impact hammer was subordinate to that of the PLB. Peak amplitudes varied as human error was the likely cause of inconsistencies. Even with that the frequency response remained similar.

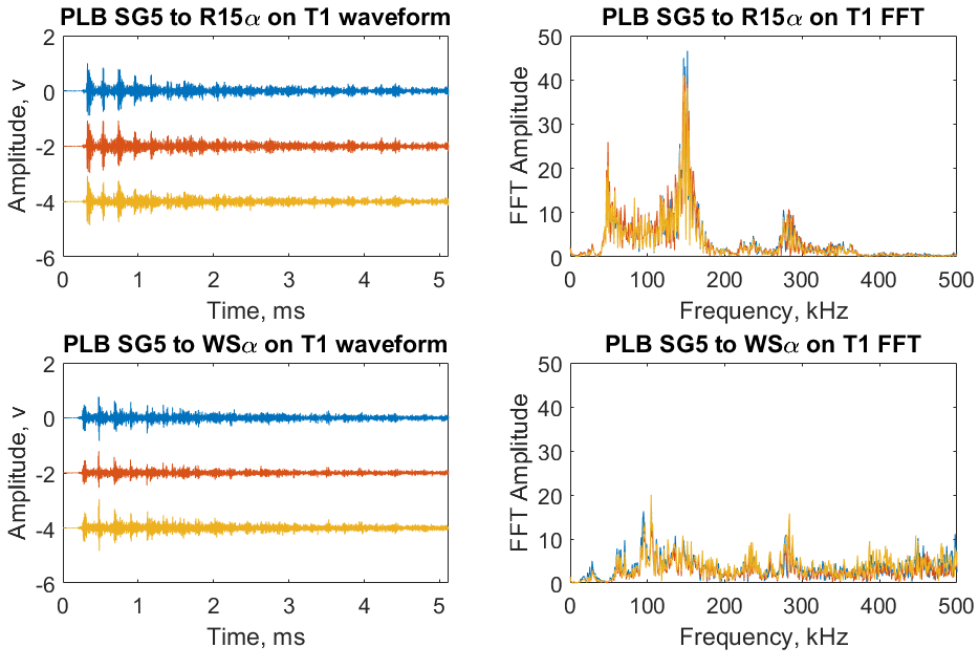

Figure 69: PLB excitation waveforms and FFTs on R15α and WSα sensors for three consecutive hits with fuel rod basket out

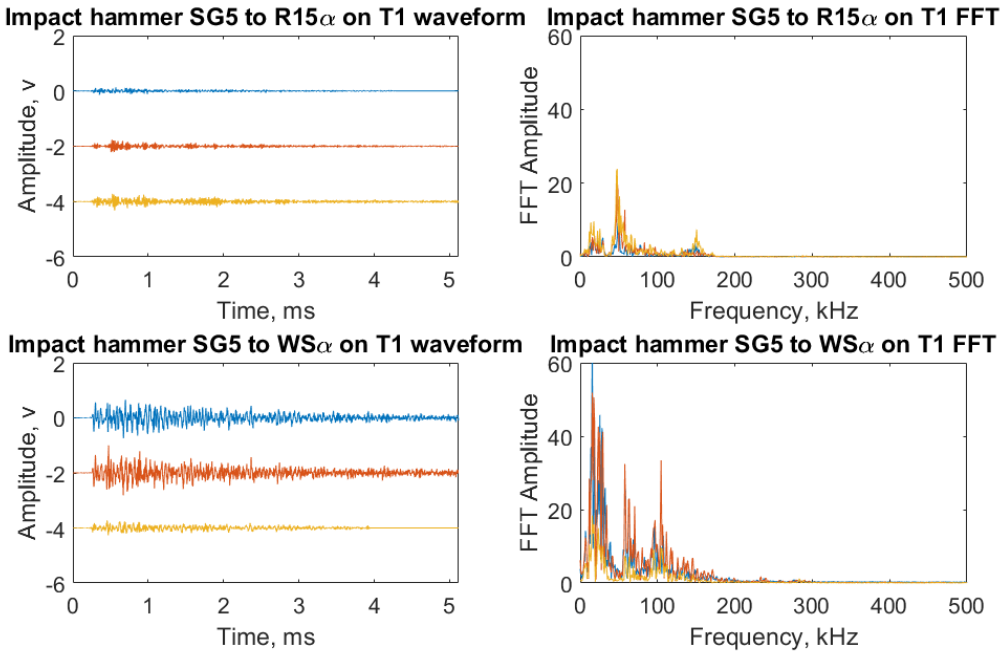

Figure 70:Impact hammer excitation waveforms and FFTs on R15α and WSα sensors for five consecutive hits with fuel rod basket out

Localization

After replaying the AE events and tuning the parameters for optimal results the data was collected. This was done by selecting the results in the localization graph (Figure 71a) and copying the calculated results in the data lookup display window (Figure 71b). Once the data was moved to MATLAB the results were analyzed. The R15α resonant type sensors' data was first examined (Figure 72). All impacts were successfully detected and localized from the results. The results were accurate where most of the detected hits lay within an inch or two of the actual impact. The PLB with the basket out resulted in the least accurate calculated impact locations. The basket condition seemed to have little effect on the localization accuracy.

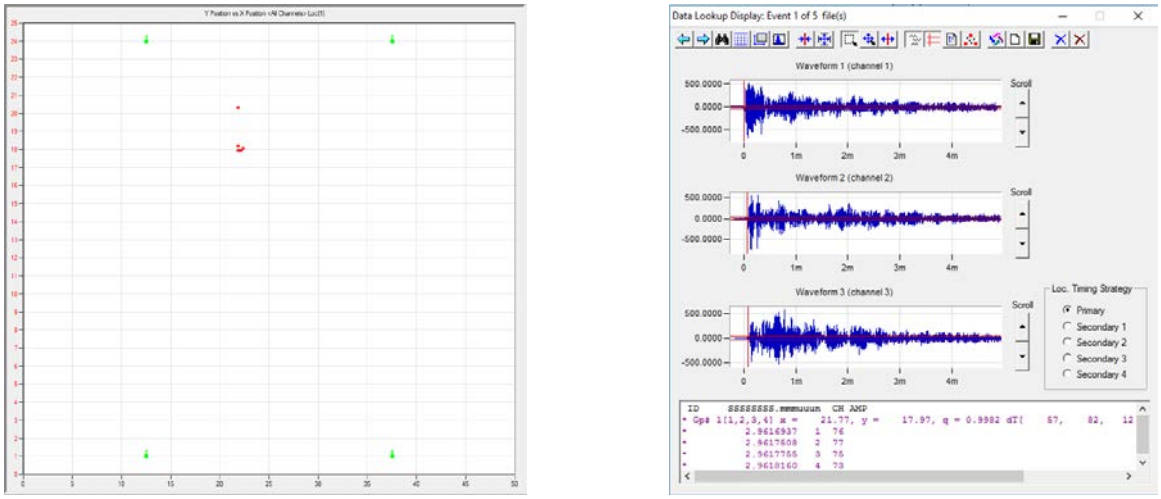

a) b)

Figure 71: AEwin graphs and window for collecting calculated AE event locations

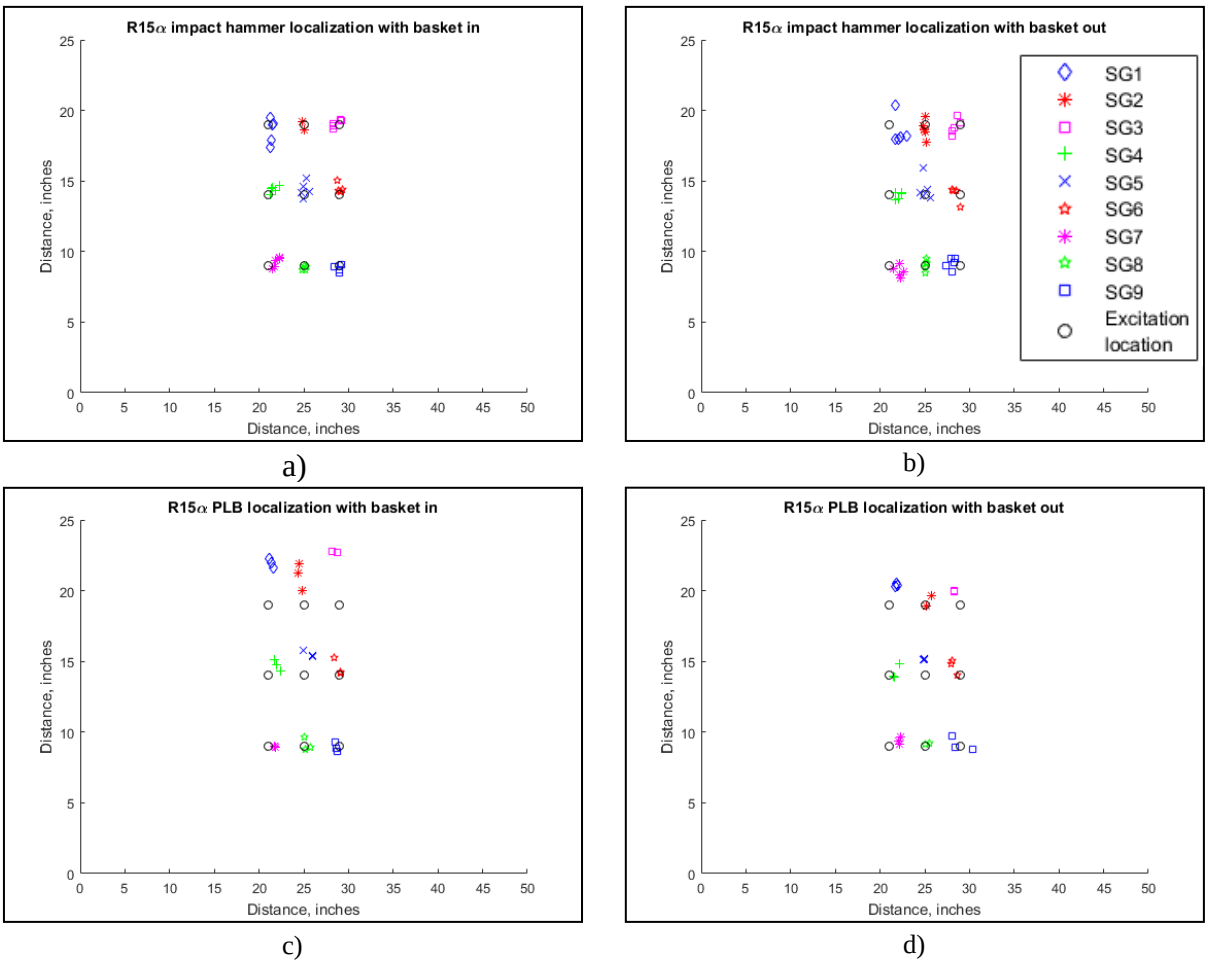

Figure 72: PLB and T304 tip impact hammer localizations of SG series using R15α

5 TRAINING/LEARNING/PROFESSIONAL DEVELOPMENT ACQUIRED FROM THIS WORK

Ph.D and undergraduate students were involved in designing and performing the tests and algorithm development. Post-docs advised the students on the test designing and algorithm development. They organized regular technical meetings of the team, and supervised the progress.

6 ADDITIONAL REPORTING

6.1 PARTICIPANTS

- Name: Lingyu Yu
- Nearest person month worked: 6 summer months

- Project role: Principal investigator
- Contribution to the project: administrate the project, advice post-docs and students, reporting.

- Name: Victor Giurgiutiu
- Nearest person month worked: 6 summer months
- Project role: co-Principal investigator
- Contribution to the project: supervise the project and advice post-docs and students.

- Name: Bin Lin
- Nearest person month worked: 36 months
- Project role: co-Principal investigator
- Contribution to the project: plan, manage, and report the project and advice graduate and undergraduate students.

- Name: Linlin Ma
- Nearest person month worked: 12 months
- Project role: Graduate Student, EMIS modeling and testing
- Contribution to the project: Performed EMIS modeling and analysis.
- Country of foreign participant: China

- Name: Mohammad Faisal Harder
- Nearest person month worked: 18 months
- Project role: Graduate student
- Contribution to the project: Performed the irradiation test
- Country of foreign participant: Bangladesh

- Name: Xiaoyi Sun
- Nearest person month worked: 12 months
- Project role: Graduate student
- Contribution to the project: Performed the testing and analysis
- Country of foreign participant: China

- Name: Roshan Joseph
- Nearest person month worked: 12 months
- Project role: Graduate student
- Contribution to the project: Performed FEM test
- Country of foreign participant: India

- Name: Stephen Howden
- Nearest person month worked: 12 months
- Project role: Graduate Student
- Contribution to the project: Planed the mockup test.

6.2 IMPACTS

During this project, we developed analytical model for piezoelectric based ultrasonic DCSS SHM. We considered the temperature and irradiation influence on the model of sensing and sensing algorithm considering acoustic emission (AE), guided ultrasonic waves (GUW), and electro-mechanical impedance spectrum (EMIS). We explored experimentally and numerically the temperature and irradiation influence on the PWAS sensor and sensing capabilities for steel canisters in nuclear spent fuel storage facilities. We performed multi-modal sensing development, verification and validation tests in laboratory environment. And finally, we studied scale-up issues and performed testing on very complex structures including a medium-scale vacuum drying chamber and a small-scale mockup canister available for the desired testing. The experimental exploration confirms not only the sensing capability of the proposed piezoelectric based sensing on complex structures with small or medium scales, but also demonstrate the detection capability for damage within certain range in the subject small-scale structures. Our work developed the potential candidate for long term structural health monitoring of spent fuel canister through piezoelectric wafer sensors and provided the sensing methodologies based on AE and GUW methodologies. The temperature and irradiation studies further demonstrated its feasibility to be used in the nuclear spent fuel cycle. This research overall provides an innovative system and methodology for enhancing the safe operation of nuclear power plant.

6.3 PRODUCTS

Journal papers:

1. Haider, M. F., Giurgiutiu, V., Lin, B., Yu, L., Lam. P. and Verst. C. (2018). “Gamma Radiation Endurance of Piezoelectric Wafer Active Sensors for SHM applications to Nuclear Spent Fuel Storage Facilities”, Journal of Nondestructive Evaluation, Diagnostics and Prognostics of Engineering Systems, ASME (under review).
2. Haider, M. F. and Giurgiutiu, V. (2017) “A Helmholtz Potential Approach to the Analysis of Guided Wave Generation during Acoustic Emission Events”, Journal of Nondestructive Evaluation, Diagnostics and Prognostics of Engineering Systems, Vol. 2, DOI:10.1115/1.4038116
3. Haider, M. F., & Giurgiutiu, V. (2017). “Analysis of axis symmetric circular crested elastic wave generated during crack propagation in a plate: A Helmholtz potential technique”, International Journal of Solids and Structures, Vol. 134, pp. 130-150
4. Haider, M. F., Giurgiutiu, V., Lin, B., & Yu, L. (2017). “Irreversibility effects in piezoelectric wafer active sensors after exposure to high temperature”, Smart Mater. Structures, Vol. 26, No. 9

5. Yu, L.; Tian, Z. (2016) “Guided wave phased array beamforming and imaging in composite plates”, Ultrasonics, Vol. 68, pp. 43-53
6. Kamas, T.; Poddar, B.; Lin, B.; Yu, L. (2015) “Assessment of Temperature Effect in Structural Health Monitoring with Piezoelectric Wafer Active Sensors”, Smart Structures and Systems, Vol. 17, No. 2

Conference proceeding papers:

1. Ma, L.; Sun, X.; Lin, B.; Yu, L.; (2015) “Temperature Effects on Piezoelectric Wafer Active Sensors for Steel Canister Health Monitoring”, *Proceedings of the ASME 2015 Pressure Vessels & Piping Division Conference*, PVP 2015-45841, July 19-23, 2015, Boston, MA

2. Lin, B.; Yu, L.; Giurgiutiu, V. (2015) “Temperature Effects on Fiber Optical Sensors for Dry Cast Storage Health Monitoring”, *Proceedings of the ASME 2015 Pressure Vessels & Piping Division Conference*, PVP 2015-45623, July 19-23, 2015, Boston, MA

3. Kamas, T.; Poddar, B.; Lin, B.; Yu, L.; Giurgiutiu, V. (2015) “Experimentation and Adaptive Modeling for Temperature Effect Quantification in PVP Structural Health Monitoring with PWAS**”**, *Proceedings of the ASME 2015 Pressure Vessels & Piping Division Conference*, PVP 2015-45595, July 19-23, 2015, Boston, MA

4. Xiaoyi Sun, Bin Lin, Jingjing Bao, Victor Giurgiutiu, Travis Knight, Poh-Sang Lam, Lingyu, Yu, “Developing a Structural Health Monitoring System for Nuclear Dry Cask Storage Canister”, 2015 SPIE Smart Structures/NDE Conference, 9-11 March 2015, San Diego, CA

5. Kamas, T.; Frankforter, E.; Lin, B.; Yu, Lingyu; Giurgiutiu, V., (2015) “Thermal Effect on E/M Impedance Spectroscopy (EMIS) of Piezoelectric Wafer Active Sensors”, *2015 Smart Structures and NDE*, 8-12 March 2015, San Diego, CA, 943500, 9435-23

1. Lin, B.; Bao, J.; Yu, L.; Giurgiutiu, V. (2016) “Acoustic emission detection with fiber optical sensors for dry cask storage health monitoring”, *2016 Smart Structures and NDE*, 20-24 March 2016, Las Vegas, NV, 98031H, doi: 10.1117/12.2219337

2. Ma, L.; Lin, B.; Sun, X.; Howden, S.; Yu, L. (2016) “Developing an piezoelectric sensing based on SHM system for nuclear dry storage system”, 2016 SPIE Smart Structures/NDE , 21-24 March, Las Vegas, NV, Paper# 9806-30

3. Sun, X.; Tian, Z.; Lin, B.; Yu, L. (2016) “Guided wave damage detection with PZT-FBG sensing”, 2016 SPIE Smart Structures/NDE , 21-24 March, Las Vegas, NV, Paper# 9804-85

4. Haider, M.; Lin, B.; Yu, L.; Giurgiutiu, V. (2016) “Characterization of Piezo Electric Wafer Active Sensors After Exposure to High Temperature”, *ASME 2016 Pressure Vessels & Piping Conference*, July 17,2016, Vancouver BC, Canada, PVP2016-63663

5. Sun, X.; Ma, L.; Howden, S.; Lin, B.; Yu, L. (2016) “Temperature Effects on Guided Ultrasonic Wave Sensing for Dry Cast Storage Health Monitoring”, *ASME 2016 Pressure Vessels & Piping Conference*, July 17,2016, Vancouver BC, Canada, PVP2016-63741

6. Tian, Z.; Howden, S.; Ma, L.; Lin, B.; Yu, L. (2016) “Damage Detection in Thick Steel Plates Using Guided Ultrasonic Waves and Non-Contact Laser Vibrometry”, *ASME 2016 Pressure Vessels & Piping Conference*, July 17,2016, Vancouver BC, Canada, PVP2016-63744

7. Sun, X.; Tian, Z.; Yu, L.; Lin, B. (2016) “Damage Detection With Guided Waves and Fiber Bragg Grating Sensor Arrays”, ASME Smart Materials, Adaptive Structures and Intelligent Systems conference, Stowe, VT, Sep 28-30 2016, Paper# SMASIS2016-9204

8. Haider, M. F., Lin, B., Yu, L., & Giurgiutiu, V. (2017, April). Sensing capabilities of piezoelectric wafer active sensors in extreme nuclear environment. In Nondestructive Characterization and Monitoring of Advanced Materials, Aerospace, and Civil Infrastructure 2017 (Vol. 10169, p. 101691Z). International Society for Optics and Photonics.
9. Haider, M. F., Giurgiutiu, V., Lin, B., & Yu, L. (2017, July). Simulation of Lamb Wave Propagation Using Excitation Potentials. In *ASME 2017 Pressure Vessels and Piping Conference* (pp. V06AT06A024-V06AT06A024). American Society of Mechanical Engineers.

Inventions:

Nothing to report

7 REFERENCE

[1] Wolf, R. A., and S. Trolier-McKinstry. "Temperature dependence of the piezoelectric response in lead zirconate titanate films." Journal of applied physics 95.3 (2004): 1397-1406.

[2] B. Jaffe, W. R. Cook Jr. and H. Jaffe: Piezoelectric Ceramics. 1971

[3] Talal M. Kamel, G. de With, Grain size effect on the poling of soft Pb(Zr,Ti)O3 ferroelectric ceramics, Journal of the European Ceramic Society, Volume 28, Issue 4, 2008, Pages 851-861, ISSN 0955-2219

[4] Choudhury, S., Li, Y. L., Krill, C., & Chen, L. Q. (2007). Effect of grain orientation and grain size on ferroelectric domain switching and evolution: Phase field simulations. Acta materialia, 55(4), 1415-1426.

[5] Lin, B.; Yu, L.; Giurgiutiu, V. (2015) “Temperature Effects on Fiber Optical Sensors for Dry Cast Storage Health Monitoring”, Proceedings of the ASME 2015 Pressure Vessels & Piping Division Conference, PVP 2015-45623, July 19-23, 2015, Boston, MA

[6] https://www.americanpiezo.com/piezo-theory/pzt.html

[7] Buessem, W. R., Cross L. E. and Gowsami, A. K., J. Am. Ceramic. Soc., 1966, 49, 33

[8] Krempl, P., Schleinzer, G., WallnGfer, W., (1997) “Gallium phosphate, GaPO4: a new piezoelectric crystal material for high-temperature sensors”. *Sensors Actuators A Physical,* 61, 361−363.1.

[9] Kazys, R., Voleisis, A., Voleisiene B., (2008) “High temperature ultrasonic transducer: review”, *Ultragarsas,* Vol. 63, No. 7–17.

[10] Zhang, S.; Yu, F. Piezoelectric materials for high-temperature sensors. *J. Am. Ceram. Soc.* 2011, *94*, 3153–3170.

[11] Jiang. X., Kim. K., Zhang. S., Johnson. J., Salazar. G., (2014) “High-Temperature Piezoelectric Sensing”, *Sensors,* Vol. 14, pp. 144-169.

[12] Zhang, S.; Yu, F. (2011) “Piezoelectric materials for high-temperature sensors”. *J. Am. Ceram. Soc*., Vol. 94, pp. 3153–3170.

[13] Giurgiutiu. V., Xu. B., Liu. W., (2010) “Development and testing of high-temperature piezoelectric wafer active sensors for extreme environments”, *Structural Health Monitoring,* Vol. 0, pp. 1-13.

[14] Krempl. PM., Krispel. F., Wallnofer. W., Leuprecht. J., (1995) “GaPO4: a new Critical review of material data”, *Proc 9th European frequency and Time Forum. Besancon, France.* pp, 59-65.

[15] Worsch, P. M., Krempl, P. W., Kreiter, F., Thanner, H., and Wallnofer, W., “GaPO4 crystals for sensor applications”, AVL List GmbH, Austria. www.ewh.ieee.org/tc/sensors/Sensors2002/advprog/47.htm.

[16] Damjanovic, D. Materials for high-temperature piezoelectric transducers. *Curr. Opin. Solid State Mater. Sci.* 1998, *3*, 469–473.

[17] Wallnofer. W., Stadler. J., and Krempl. P., (1993) “Temperature dependence of clastic constants of GaPO4 and its influence in BAW und SAW devices” *Proc 7th European frequency and Time Forum. Neuchatel, Switzerland*. pp. 653.

[18] Hornsteiner, J., Born, E., Fischerauer, G., Riha, E., (1998) “Surface Acoustic Wave Sensors for High-Temperature Applications”, *In Proceedings of the IEEE International Frequency Control Symposium,* Pasadena, CA, USA, pp. 615–620.

[19] Fachberger, R., Bruckner, G., Knoll, G., Hauser, R., Biniasch, J., Reindl, L., (2014) “Applicability of $LiNbO_3$, langasite and $GaPO_4$ in high-temperature SAW sensors operating at radio frequencies”, *Sensors,* Vol. 14, No. 165.

[20] Ohlendorf, G., Richter, D., Sauerwald, J., Fritze, H., (2008) “High-temperature electrical conductivity and electro-mechanical properties of stoichiometric lithium niobate”, *Diffus. Fundam. Vol. 8*, pp. 1–7.

[21] Da Cunha, M.P.; Moonlight, T.; Lad, R.; Frankel, D.; Bernhard, G. High-Temperature Sensing Technology for Applications up to 1,000 °C. *In Proceedings of the IEEE Sensors, Lecce, Italy*, 29 October 2008; pp. 752–755.

[22] Fritze, H., (2006) “High-temperature piezoelectric materials: Defect chemistry and electro-mechanical properties”, *J. Electroceram.*, Vol. 17, pp. 625–630.

[23] Puigcorbé, J.; Vogel, D.; Michel, B.; Vilà, A.; Gràcia, I.; Cané, C.; Morante, J. High-temperature degradation of Pt/Ti electrodes in micro-hotplate gas sensors. *J. Micromech. Microeng.* **2003**, *13*, S119–S124.

[24] Schulz, M., Sauerwald, J., Richter, D., Fritze, H., (2009) “Electromechanical properties and defect chemistry of high-temperature piezoelectric materials”’ *Ionics* , Vol. 15, pp. 157–161.

[25] Richter, D.; Fritze, H., (2011) "High-temperature Stable Electrodes for Langasite Based Surface Acoustic Wave Devices", *In Proceedings of the Sensor and Test Conferences 2011, Nürnberg, Germany, 9 June 2011*; pp. 532–537.

[26] Frankel, D., Bernhardt, G., Sturtevant, B., Moonlight, T., Pereira da Cunha, M., Lad, R., (2008) "Stable Electrodes and Ultrathin Passivation Coatings for High-Temperature Sensors in Harsh Environments", *In Proceedings of the IEEE Sensors, Lecce, Italy*, pp. 82–85.

[27] Dankov, IA., Zvereva, OV., lvannikov, VI., Tokarev, EF., Khatamov, FS., (1991) "Electromechanical properties of gallium phosphate between -196 and +723'C", *Sov Phys Crystallogr*, Vol. 36, pp. 277-279.

[28] Krispel, F., Reiter, C., Neubig, J., Lenzenhuber, F., Krempl, P.W., Wallnofer, W. and Worsch, P.M., (2003) "Properties and applications of singly rotated GaPO4 resonators", *In: Frequency Control Symposium and PDA Exhibition Jointly With the 17th European Frequency and Time Forum, Proceedings of the 2003 IEEE International, Tampa, FL*; 4–8, pp. 668–673.

[29] Worsch, PM., Krempl, PW., Krispel, F., (2001) "The temperature-stable piezoelectric material GaPO4 and its sensor applications", *11th International Conference on Solid-State Sensors and Actuators*. *Munich, Germany*.

[30] Pulliam, W.J., Russler, P.M., Fielder, R.S., (2001) "High-Temperature High-Bandwidth Fiber Optic MEMS Pressure-Sensor Technology for Turbine Engine Component Testing", *In Proceedings of Fiber Optic Sensor Technology and Applications, Boston, MA, USA*, pp. 229–238.

[31] Wang, J., Dong, B., Lally, E., Gong, J., Han, M., Wang, A., (2010) "Multiplexed high-temperature sensing with sapphire fiber air gap-based extrinsic Fabry-Perot interferometers", *Opt. Lett.*, Vol. 35, pp. 619–621.

[32] Hamidon, M.N.; Skarda, V.; White, N.M.; Krispel, F.; Krempl, P.; Binhack, M.; Buff, W. (2006) "High-temperature 434 MHz surface acoustic wave devices based on GaPO4", *IEEE Trans. Ultrason. Ferroelectr. Freq. Control*, 53, 2465–2470.

[33] Zhang, S., Fei, Y., Chai, B., Frantz, E., Synder, D., (2008) "Characterization of piezoelectric single crystal $YCa_4O(BO_3)_3$ for high temperature applications", *Appl. Phys. Lett*., Vol. 92, No. 202905.

[34] Kim, K., Zhang, S., Huang, W., Yu, F., (2011) "$YCa_4O(BO_3)_3$(YCOB) high temperature vibration sensor", *Appl. Phys. Lett.*, Vol. 109, No. 126103.

[35] Parks, D.A.; Zhang, S.; Tittmann, B.R., (2013) "High-temperature (>500 °C) ultrasonic transducers: An experimental comparison among three candidate piezoelectric materials", *IEEE Trans. Ultrason. Ferroelectr. Freq. Control 2013*, Vol. 60, pp. 1010–1015.

[36] Johnson, J.A., Kim, K., Zhang, S., Wu, D., Jiang, X., (2013) "High-Temperature (>1,000 °C) Acoustic Emission Sensor'. *In Proceedings of the SPIE Smart Structures and Materials + Nondestructive Evaluation and Health Monitoring*, San Diego, CA, USA, doi: 10.1117/12.2009301.

[37] Zhang, S., Yu, F., (2011) "Piezoelectric materials for high-temperature sensors", *J. Am. Ceram. Soc*. Vol. 94, pp. 3153–3170.

[38] Kim, K., Zhang, S., Salazar, G., Jiang, X., (2012) "Design, fabrication and characteristics of high temperature piezoelectric vibration sensor using YCOB crystals," *Sens. Actuators A*, vol. 178, pp. 40–48.
[39] Park, J., Lindberg, C. R., Vernon III, F. L.,(1987) "Multitaper spectral analysis of high-frequency seismograms," *J. Geophys. Res*., vol. 92, no. B12, pp. 12675–12684.
[40] Kirk, K.; Scheit, C.; Schmarje, N., (2007) "High-temperature acoustic emission tests using lithium niobate piezocomposite transducers", Insight Non Destructive. Test. Cond. Monit. Vol. 49, pp. 142–145.
[41] Piezocryst Inc. Available at: http://www.gapo4.com (accessed February 25, **2010**).
[42] Ohlendorf, G.; Richter, D.; Sauerwald, J.; Fritze, H. High-temperature electrical conductivity and electro-mechanical properties of stoichiometric lithium niobate. Diffus. Fundam. 2008, 8, 1–7.
[43] Fachberger, R.; Bruckner, G.; Knoll, G.; Hauser, R.; Biniasch, J.; Reindl, L. Applicability of LiNbO3, langasite and GaPO4 in high-temperature SAW sensors operating at radio frequencies. IEEE Trans. Ultrason. Ferroelectr. Freq. Control 2004, 51, 1427–1431.
[44] Hornsteiner, J.; Born, E.; Fischerauer, G.; Riha, E. Surface Acoustic Wave Sensors for High-Temperature Applications. In Proceedings of the IEEE International Frequency Control Symposium, Pasadena, CA, USA, 29 May 1998; pp. 615–620.
[45] Giurgiutiu, V.; Zagrai, A. N.; Bao, J. (2002) "*Piezoelectric Wafer Embedded Active Sensors for Aging Aircraft Structural Health Monitoring*", Structural Health Monitoring – an International Journal, Vol. 1, No. 1, pp. 41-61, July 2002, Sage Pub. 1.
[46] Giurgiutiu, V. & Zagrai, A. (2000) "*Damage Detection in Simulated Aging-Aircraft Panels Using The Electro-Mechanical Impedance Technique*", In Adaptive Structures and Material Systems Symposium, ASME Winter Annual Meeting (pp. 1–10). Orlando, FL.
[47] Kamas, T.; Giurgiutiu, V.; Lin, B. (2015) "*E/M impedance modeling and experimentation for the piezoelectric wafer active sensor*", Smart Materials and Structures, Volume 24, Number 11, 115040.
[48] Giurgiutiu, V. (2008) "*Structural Health Monitoring with Piezoelectric Wafer Active Sensors*", Elsevier Academic Press, ISBN 978-0120887606, 2008
[49] https://www.americanpiezo.com/apc-materials/physical-piezoelectric-properties.html
[50] Mezheritsky, A. V. (2002). "*Quality factor of piezoceramics*", Ferroelectrics, 266(1), 613-640.
[51] Mezheritsky, A.V. (2002) IEEE UFFC, 4, (2002) 484.
[52] Laboratory for Active Materials and Smart Structures. (2010) "Wavescope 2.5", *University of South Carolina*